A SATELLITE-BASED RADAR WIND SENSOR

Weizhuang Xin

Radar Systems and Remote Sensing Laboratory
University of Kansas Center for Research, Inc.
2291 Irving Hill Road
Lawrence, Kansas 66045-2969
913/864-4835
FAX: 913/864-7789 OMNET: KANSAS.U.RSL TELEX: 706352

RSL Technical Report 8760-2

June 1991

Supported by:

NASA Marshall Space Flight Center
Marshall Space Flight Center, AL 35812

Contract NAG 8-796

Table of Contents

ACKNOWLEDGEMENT i
TABLE OF CONTENTS ii
LIST OF FIGURES v
LIST OF TABLES xiii
ABSTRACT xiv
CHAPTER 1 — INTRODUCTION 1
  1.0 RADAR REMOTE SENSING 1
  1.1 BACKGROUND 2
    1.1.1 Need for Global Wind Data 2
    1.1.2 Instruments used for Global Measurement of Wind 4
    1.1.3 Required Observations Resolutions 7
    1.1.4 The LAWS from EOS 8
    1.1.5 Effect on Lidars by Clouds 9
  1.2 THE DOPPLER RADAR WIND SOUNDER (RAWS) 10
  1.3 DISSERTATION OUTLINE 10
CHAPTER 2 — RADAR BACKSCATTER AND ATTENUATION FROM CLOUDS 12
  2.1 SCATTERING FROM CLOUDS 12
    2.1.1 Definitions of Radar Cross Sections 12
    2.1.2 Scatter From a Single Spherical Particle 14
    2.1.3 Rayleigh Approximation 15
    2.1.4 Volume Scatter 19
      2.1.4.1 Volume Scattering Coefficient 20
      2.1.4.2 Volume Absorption Coefficient 20
      2.1.4.3 Volume Extinction Coefficient 21
      2.1.4.4 Volume Backscattering Coefficient 21
    2.1.5 Radar Equation 23
  2.2 MODELS OF DROP-SIZE DISTRIBUTION IN CLOUDS 24
    2.2.1 Contents of Clouds 24
    2.2.2 Droplet Size Distribution of Water Cloud 25
    2.2.3 Ice Cloud Modeling 30
  2.3. COMPUTER SIMULATIONS AND CONCLUSIONS 31
    2.3.1 Computer Simulations of SNR of Radar Echoes 32
    2.3.2 Conclusions and Future Work 38

CHAPTER 3 — CONCEPTUAL DESIGN AND ANALYSIS OF PERFORMANCE....... 40
- 3.1 INTRODUCTION 40
- 3.2 BASIC CONFIGURATION OF THE SYSTEM 42
  - 3.2.1 System Parameters 44
  - 3.2.2 Antenna Scan Schemes 50
    - 3.2.2.1 Uniform Scan 51
    - 3.2.2.2 Discrete Scan 53
    - 3.2.2.3 Combination of Uniform and Discrete Scans 53
    - 3.2.2.4 Scan Trajectory 54
  - 3.2.3 Tracking the Doppler Shift Caused by Satellite Motion 57
    - 3.2.3.1 Frequency Tracking by a Phase Lock Loop 60
- 3.3 MEASUREMENT ERRORS OF WIND SPEED DUE TO ANTENNA POINTING ERROR AND FREQUENCY MEASUREMENT ERROR 65
  - 3.3.1 Basic Equations 65
  - 3.3.2 Error Analysis 66
  - 3.3.3 Error Bound Caused by Frequency Uncertainty 67
  - 3.3.3 Error Due to Uncertanties in Antenna Pointing Angles 69
  - 3.3.4 The Total Error Bound 70
- 3.4 CONCLUSIONS AND RECOMMENDATIONS FOR FURTHER STUDY 71

CHAPTER 4 — ESTIMATION OF MOMENTS OF POWER SPECTRUM 73
- 4.1 MOMENTS OF SPECTRUM 73
- 4.2 INTRODUCTION TO RANDOM SIGNALS AND SPECTRAL ANALYSIS.... 74
  - 4.2.1 Random Process 74
  - 4.2.2 Power Spectral Density 75
- 4.3 COMPUTER SIMULATION OF RANDOM SIGNALS 76
  - 4.3.1 Shape of the Doppler Spectrum 76
  - 4.3.2 Generating Random Variables with Specific PDFS 78
  - 4.3.3 Generation of A Random Process with A Specific Autocorrelation Function 80
    - 4.3.3.1 Using An ARMA Model 80
    - 4.3.3.2 Using An Inverse Fourier Transform 81
- 4.4 ESTIMATION OF THE MOMENTS OF THE DOPPLER SPECTRUM 83
  - 4.4.1 FFT Method 84
    - 4.4.1.1 Estimation of The Mean With Noise Suppression....... 87
    - 4.4.1.2 FFT Method with De-aliasing 89
  - 4.4.2 The Covariance Estimator 92
  - 4.4.3 The Parametric Methods 96
  - 4.4.4 Random Samples and Spectrum Estimation 99

4.5 RESULTS OF COMPUTER SIMULATIONS, CONCLUSIONS, AND FUTURE WORK 101
    4.5.1 Monte Carlo Simulation of the Estimators 101
    4.5.3 Conclusions and Further Work 106

APPENDIX 4.A PROOF THAT THE FFT ESTIMATOR FOR MEAN IS CONSISTENT 108

CHAPTER 5 — ALGORITHMS FOR REMOVAL OF RANGE AND FREQUENCY AMBIGUITIES 110

5.1 INTRODUCTION 110

5.2 INTERPULSE PHASE CODING 113
    5.2.1 Radar Ambiguity Functions 113
    5.2.2 Random-Phase Coding 116
    5.2.3 Deterministic Phase Coding 121

5.3 MULTIPLE PRF AND FREQUENCY AMBIGUITY REMOVAL 122
    5.3.1 Staggered PRF Method- A 123
    5.3.2 Staggered PRF Method- B 127
    5.3.3 Random Pulse Position Coding 128

5.4 WAVEFORM MODULATION AND AMBIGUITY REMOVAL 129
    5.4.1 Waveform Modulation Reduces Range Ambiguity 129
    5.4.2 An Application 137

5.5 RESULTS AND CONCLUSIONS 139
    5.5.1 The Simulator 139
    5.5.2 Monte Carlo Simulation 140
    5.5.3 Conclusion 148

APPENDIX 5.A. AMBIGUITY FUNCTION FOR WAVEFORM MODULATION 149

CHAPTER 6 — CONCLUSIONS AND RECOMMENDATIONS FOR FUTURE WORK 159

REFERENCES 163

List of Figures

Figure 2.1. 18

Mie efficiency factors for scattering and extinction by a water sphere as a function of drop radius (Fraser et al., 1975 Am. Soc. Photogram. [29]). Horizontal arrows indicate drop radii; a) at 3 GHz; b) at 30 GHz; c) at 300 GHz.

Figure 2.2. 23

Total attenuation of radio waves by atmospheric gases versus frequency for various elevation angles (from satellite communication system).

Figure 2.3. 26

Measured drop-diameter histograms for different kinds of clouds. Note the change in ordinate scale from part to part. Note significant numbers of large drops in all but (d). (a) Orographic cloud, Hawaii, ρ = 0.4 gm-3. (b) Dark stratus over Hilo, HI, ρ = 0.34 gm-3. (c) Tradewind cumulus over Pacific near Hawaii, 615 m above base, ρ = 0.5 gm-3. (d) Continental cumulus over Blue Mountains near Sydney, Australia, 615 m above base, ρ = 0.35 gm-3.

Figure 2.4. 26

Average cloud-drop spectra reported by aufm Kampe and Weickmann for different cloud types. Note the large number of large drops present in the cumulus congestus and cumulonimbus clouds.

Figure 2.5. 27

Distribution of drop radii for summer convective clouds over the U.S. based on work of Battan and Reitan. Left: 19 fair-weather cumulus clouds with average of 293 drops cm-3. Right: cumulus congestus for two cases: arrested growth with 247 drops cm-3 and those growing to point where 1950s weather radar showed echoes with 188 drops cm-3.

Figure 2.6. 29

Computer simulated drop-size-distributions of three different types of clouds: 0.3, 0.5, and 1.0 gm^{-3} (thin, medium and heavy).

Figure 2.7. 30

Average ice crystal spectra in a) Ci Spi, b) AS, c) and d) Ci unc, e) Cs, f) Ac and g) Cb cap. The size class is 200 μ.

Figure 2.8. 33

Spatial distribution of microstructure parameters in cumulus cloud. (a) drop diameter (μm), (b) drop concentration (number cm^{-3}), (c) W_L (gm^{-3}).

Figure 2.9. 35

Signal to noise ratio of radar echo as a function of cloud penetration (water content of cloud = 0.3 gm^{-3}); a) orbit height = 300 km; b) orbit height = 830 km.

Figure 2.10. 36

Signal to noise ratio of radar echo as a function of cloud penetration (water content of cloud = 0.5 gm^{-3}); a) orbit height = 300 km; b) orbit height = 830 km.

Figure 2.11. 37

Signal to noise ratio of radar echo as a function of cloud penetration (water content of cloud = 1.0 gm^{-3}); a) orbit height = 300 km; b) orbit height = 830 km.

Figure 2.12. 38

Signal to noise ratio of radar echo as a function of reflectivity factor Z ($mm^6\ m^{-3}$). The return signal is from 1 km depth from the cloud top.

Figure 3.1. 41

Basic concepts of two beam conical scan: the same area can be viewed forward and rearward by the antenna with different looking angles for wind vector component retrieval.

Figure 3.2. 45

Percentage transmission through the earth's atmosphere, along the vertical direction, under clear sky conditions.

Figure 3.3. 46

Tradeoff between the antenna pointing angle, antenna beamwidths and the vertical resolution, where ϕ is antenna pointing angle, r_e is the edge-to-edge vertical resolution, and H is the height of the antenna.

Figure 3.4. 51

Illustration of pulse-pair transmission scheme, and limit on the PRT. T is the PRT, T_1 is inter-pulse spacing.

Figure 3.5 54

Antenna scan pattern; a) uniform scanning; b) discrete scanning; c) a combination of the uniform and discrete scanning.

Figure 3.6. 55

Antenna scan trajectories at 30 deg. and 35 deg. pointing angles with scan period = 10 s; a) at 300 km orbit; b) at 830 km orbit.

Figure 3.7. 58

Functional Block Diagram of Radar Wind Sounder. It shows the two stage tracking of the Doppler shift caused by satellite motion.

Figure 3.8. 59
Equivalent linearized baseband model of a PLL.

Figure 3.9. 63
Equivalent block diagram of a second order PLL with perfect integrators.

Figure 3.10. 64
Monte-Carlo simulation of tracking error by a second order PLL with perfect integrator; a) ensemble average; b) standard deviation of frequency error.

Figure 4.1. 83
Example of computer simulated spectrum of a random signal with spectrum width $\sigma = 0.3$, mean frequency -0.7, and SNR 10 dB.

Figure 4.2. 87
Simulation of FFT estimator without de-aliasing and noise suppression, under the condition $\sigma = 0.1$, SNR = 0 dB, and 10 dB, and the number of runs = 200.

Figure 4.3. 88
Monte Carlo simulation of FFT estimator with noise suppression; a) estimate under the condition $\sigma = 0.1$, SNR = 0 dB, and 10 dB, with 200 runs; b) RMS errors as functions of frequency and the spectral width of power spectrum of signal.

Figure 4.4 91
FFT Estimator with de-aliasing applied with $\sigma = 0.1$, SNR = 10 dB; a) the plot of ensemble average of estimates; b) plot of RMS error with 200 runs. For the RAWS parameters the scale would be from -1.75 kHz to + 1.75 kHz. The frequency shown here is normalized to the Nyquist frequency.

Figure 4.5. 95

Computer Simulation of the Covariance Method with 128 pairs of samples ; a) mean estimate, with inter-pulse-pair spacing = 1, 7, SNR = 10 dB, $\sigma = 0.1$; b) RMS errors with 200 runs. For the RAWS parameters the scale would be from -1.75 kHz to + 1.75 kHz. The frequency shown here is normalized to the Nyquist frequency.

Figure 4.6. 97

Computer Simulation of AR(2) and AR(20) estimators with 200 runs, SNR = 10 dB, $\sigma = 0.1$, and 128 samples for each run; a) plot of mean estimates; b) plot of RMS errors. For the RAWS parameters the scale would be from -1.75 kHz to + 1.75 kHz. The frequency shown here is normalized to the Nyquist frequency.

Figure 4.7. 102

Monte Carlo Simulation of FFT estimator with de-aliasing, with 200 runs, and 128 samples for each run; a) Expectation simulated; b) RMS error as a function of SNR, and frequency. Both normalized (-1, 1) and RAWS (-1750, 1750) frequency scales are shown.

Figure 4.8. 103

Monte Carlo Simulation of the Covariance estimator, the spectral width $\sigma = 0.3$, with 200 runs, and 128 samples for each run; a) Mean estimate for SNR = 0 dB; b) RMS errors as functions of SNR and frequency.

Figure 4.9. 104

Monte Carlo Simulation of the Autoregressive , AR(2), method, with 200 runs, and 128 samples for each run; a) Expectation simulated; b) RMS error as a function of SNR and frequency.

Figure 4.10. 105

Monte Carlo simulation of FFT estimator with RMS error as functions of SNR and spectral width. A fixed mean frequency 0.5 is used in this simulation.

Figure 4.11. 105

Monte Carlo simulation of the covariance estimator with RMS error as functions of SNR and spectral width. A fixed mean frequency 0.5 is used in this simulation.

Figure 4.12. 106

Monte Carlo simulation of AR(2) estimator with RMS error as functions of SNR and spectral width. A fixed mean frequency 0.5 is used in this simulation.

Figure 5.1. 118

Examples of ambiguity function: a) ambiguity function for single rectangle pulse, b) ambiguity function for single linear FM modulated pulse. Absolute value shown for response function. Ambiguity function is square of response function, but contrasts are too great to show effectively on a 3-D graph. All other graphs in Chap. 5 labeled "ambiguity function" are actually response-function magnitudes.

Figure 5.2 119

Ambiguity function of uniformly spaced pulses in which the pulse shape is Gaussian and total pulse number is 30.

Figure 5.3. 119

Ambiguity function of uniformly spaced pulses with random phase coding, the total pulse number is 30.

Figure 5.4. 120

Ambiguity function of uniformly spaced pulses with Barker phase coding, the total pulse number is 13.

Figure 5.5. 122

Ambiguity function for uniformly spaced pulses with $-\pi/4$, $\pi/4$, ..., $-\pi/4$, $\pi/4$ inter-pulse coding,the pulse shape is Gaussian, and total number of pulses is 30.

Figure 5.6. 126

Simulation of STAGGERED PRF-A method, a) $\sigma = 0.1$, SNR = 0 dB, b) $\sigma = 0.3$, SNR = 0 dB. Normalized frequencies are shown.

Figure 5.7. 128

Figure 5.7. Simulation of STAGGERED PRF-B method with $T_1/T_2 = 0.875$, $\sigma = 0.3$, SNR = 0 dB. Normalized frequency is shown.

Figure 5.8. 131

Configuration of dual-modulation receiver.

Figure 5.9. 135

Ambiguity function of dual linear FM modulated pulse train. $T_2 = 0.3\ T_1$, time bandwidth product = 10.0

Figure 5.10. 136

Cross ambiguity functions, a) as an output of channel I, b) as an output of channel II.

Figure 5.11. 138

Simulation of waveform modulation method for estimating first moment with extended frequency range, with one run, $\sigma = 0.3$, SNR = 10 dB.

Figure 5.12. 139

Ambiguity function for the same pulse train as in Figure 5.10, except random phase coding was applied.

Figure 5.13. 142

Monte Carlo simulation of STAGGERED PRF-A method with 100 runs, $\sigma = 0.3$, number of pulse pairs = 128; a) probability of false estimate; b) RMS error as a function of frequency and SNR.

Figure 5.14. 143

Monte Carlo simulation of STAGGERED PRF-B method with 100 runs, σ = 0.3, number of pulse pairs = 128; a) ensemble average of estimates; b) RMS error as a function of frequency and SNR.

Figure 5.15. 144

Monte Carlo simulation of waveform modulation method with 100 runs, σ = 0.3, number of pulse pairs = 128; a) ensemble average of estimates; b) RMS error as a function of frequency and SNR

Figure 5.16. 145

Monte Carlo simulation of STAGGERED PRF-A method with RMS error and probability of false estimate as function of spectral width of the signal and SNR, 100 runs, number of pulse pairs = 128; a) plot of the probability of false estimate; b) plot of RMS errors.

Figure 5.17. 146

Monte Carlo simulation of STAGGERED PRF-B method with 100 runs, number of pulse pairs = 128; a) plot of the ensemble average of estimates; b) plot of RMS errors as a function of spectral width of input signal.

Figure 5.18. 147

Monte Carlo simulation of WAVEFORM MODULATION method with 100 runs, number of pulse pairs = 128; a) plot of the ensemble average of estimates; b) plot of RMS errors as a function of spectral width of input signal.

List of Tables

Table 1.1. Global and Synoptic Scale Observational Requirements 5

Table 1.2. Characteristics of various spaceborne wind sensors 6

Table 1.3. Required Observational Resolution 7

Table 1.4. Base Parameters for a lidar Wind Sounder 9

Table 2.1. $|K|^2$ and Im(-K) for Clouds (Table 4.1, Battan [28]) 17

Table 2.2. Some Typical Parameters for Coluds 30

Table 2.3. Parameters In Cloud Modeling 32

Table 2.4. Parameters Used in Computer Simulation 32

Table 3.1. Basic Parameters for The Radar Wind Sounder 43

Table 3.2. Swath Widths For Different Orbits and Antenna Pointing Angles 48

Table 3.3. Roots of equation 57

Table 3.4. Norm of linear operator A^{-1}in l_∞ space 68

Table 3.5. Norm of non-linear operator (3.38) in l_∞ space 70

ABSTRACT

The objective of this study is to investigate the application of Doppler radar systems for global wind measurement. A model of the satellite-based radar wind sounder (RAWS) is discussed, and many critical problems in the designing, such as the antenna scan pattern, tracking the Doppler shift caused by satellite motion, and backscattering of radar signals from different types of clouds, are discussed along with their computer simulations.

In addition, algorithms for measuring mean frequency of radar echoes, such as the FFT estimator, the covariance estimator, and the estimators based on autoregressive models, are discussed. Monte Carlo computer simulations were used to compare the performance of these algorithms. Anti-alias methods are discussed for the FFT and the autoregressive methods.

Several algorithms for reducing radar ambiguity were studied, such as random phase coding methods and staggered PRF methods. Computer simulations showed that these methods are not applicable to the RAWS because of the broad spectral widths of the radar echoes from clouds. A waveform modulation method using the concept of spread spectrum and correlation detection was developed to solve the radar ambiguity. Radar ambiguity functions were used to analyze the effective signal-to-noise ratios for the waveform modulation method. The result showed that, with suitable bandwidth product and modulation of the waveform, this method can achieve the desired maximum range and maximum frequency of the radar system.

Chapter 1

Introduction

1.0 RADAR REMOTE SENSING

Since the early 1960s, the field of radar remote sensing has grown into an important technology for scientific research. Radar remote sensing has been applied in the areas of 1) astronomical studies, 2) military applications, 3) environmental monitoring, and 4) meteorology. The importance of radar remote sensing can be attributed to two predominant factors: a) radars do not require the sun as a source of illumination, and b) operating in the microwave region, a radar signal can penetrate fog, clouds, and to some extent precipitation (rain, or snow).

During the past, radar remote sensing has found wide applications in meteorology, such as storm observation and forecasting. For example, ground-based radars are widely used for detecting severe weather and measuring rain-fall rate [1-2]. Ground-based Doppler radars, most of them operated in very-high frequency (VHF) and ultra-high frequency (UHF), are used for detecting turbulence, local wind field etc [3-5]. Recently, S band ground-based Doppler radars were developed to detect severe weather, precipitation and velocity fields [6]. As global environmental study becomes more and more important, spaceborne radar systems are anticipated to become more crucial in monitoring global environment, for instance, measuring rain-fall rate [7].

In this study, we discuss one potential application for radar remote sensing — using a spaceborne Doppler radar system to monitor the global wind fields. Numerous ground-based VHF and UHF Doppler radar systems are being used in measuring turbulence and local wind, and recently some microwave radar systems were used to measure clouds [8]. However, few spaceborne Doppler radar systems have been studied for global wind measurement purposes.

In this dissertation, we carry out a system study of a spaceborne radar wind sounder. The major difficulties treated concerning the implementation of a spaceborne Doppler radar wind sounder include power requirements, antenna scan pattern, algorithms for measuring mean frequency of Doppler shifts of radar signals, removal of frequency ambiguity, and compensating the Doppler shift caused by satellite motion. In addition to theoretical analysis, computer simulations were used to evaluate the system performance and to compare algorithms for measuring mean Doppler frequency of the radar signal and algorithms for removal of radar-frequency ambiguity and range ambiguity.

1.1 BACKGROUND

1.1.1 NEED FOR GLOBAL WIND DATA

The importance of investigating a spaceborne Doppler radar for wind measurement applications arises from the need for global wind data for both operational and scientific-research applications. As pointed out in [9], "Knowledge of the global wind field is widely recognized as fundamental to advancing our understanding and prediction of the total Earth system. Yet, because wind profiles are primarily measured by land-based rawinsondes, the oceanic areas (covering roughly three quarters of the Earth's surface) and many regions of the less-developed southern hemisphere land areas are poorly observed. The gap between our requirements for global wind data and their availability continues to widen. For example, as faster computers become available to model the atmosphere with ever increasing resolution and sophistication, our ability to do so will be hampered because of the lack of data, particularly wind profiles."

An improved understanding of the atmospheric wind field is essential for purposes such as understanding the physics of the atmosphere, weather forecasting, and many others. One of the most important applications for global wind data is in numerical weather prediction (NWP), a technique on which modern weather forecasts are based. Numerical weather prediction utilizes basic hydrodynamic and thermodynamic equations to predict the future states of the environment from the present states [10]. As an initial value problem, NWP depends critically on the accurate specification of the state at time zero. If the models used in weather prediction are correct, then the improvement in weather prediction largely depends on the observation and measurement of the state of the weather. This view is generally shared by the numerical prediction community [11].

Significant progress has been made in NWP in recent years, especially with the development of accurate global numerical weather prediction models, improved global coverage of the atmosphere provided by satellite observing systems, and with the development of high speed computers. However, the current weather forecasts are still not close to the theoretical limit of dynamic predictability, generally accepted to be about two weeks. Further improvements of weather forecasts are considered necessary in the following aspects: the observations that provide the initial data for the models, the objective analysis techniques, and the correctness of the weather models [12].

The variables used in NWP are temperature, pressure, and wind. The early NWP models were designed to use only pressure and temperature data. Winds were derived from the mass observations using the geostrophic relationship. This relationship assumes that the latitudinally dependent Coriolis force [13] is balanced by the pressure gradient force. This was a natural choice because pressure observations were more abundant and more accurate than wind observations. Recently, however, it has become increasingly clear that wind data are extremely effective for use in numerical weather prediction. Two reasons for this are explained by Kalnay, et al. [14]. The first reason is derived from the concept of geostrophic adjustment. For most scales of importance to numerical weather prediction, the models effectively retain wind data incorporated into the initial conditions. Specifically, small-scale pressure-height variations do not result in small-scale changes in the wind field. Instead, they are rapidly dispersed as gravity waves. In other words, NWP models accept the wind data more readily than mass data for scales which can be observed.

The second reason that winds are an extremely effective source of data comes from the well-known fact that integration of noisy data reduces the effect of random noise, whereas differentiation enhances the effect of noise. The geostrophic relationship implies that wind is proportional to the horizontal pressure gradient. At increasingly smaller scales, the geostrophic relationship is often invalid so that wind becomes an increasingly more accurate measure of atmosphere state than do the pressure or height measurements.

In addition, the wind observations are especially important in the Tropics, since the quasi-geostrophic balance, present in the mid-latitudes, breaks down. As a result, the wind field cannot be determined from the pressure or height. Moreover, a reliable estimate of the divergent component of the wind is necessary to depict the convective areas in the Tropics that provide a source of energy for the equatorial regions and at times the mid-latitudes. Therefore, wind measurements are more important than temperature sounding wherever the winds are not in balance with the mass field. This means that they are required to faithfully predict the smaller scale systems at all latitudes and all scales in the Tropics. For the larger scales in mid-latitudes, temperature data are probably more important, provided they are accurate to about ± 1°C.

Forecast simulations, using wind data in the Tropics and surface wind data over the oceans, show significant increases in predictive skill. Global climate modeling (GCM) simulation studies show that an rms wind error of 2m/s is equivalent to an rms temperature error of about 1°C outside of the Tropics. Thus, a wind-measuring system that could achieve such accuracy would be equivalent to the best that is possible by any passive temperature measurement system now available or under consideration [11].

1.1.2 INSTRUMENTS USED FOR GLOBAL MEASUREMENT OF WIND

Today's operational wind-velocity observing systems are basically implemented in two forms: those mounted on instrumented towers, and mobile instruments mounted aboard ships, aircraft, or balloons. These instruments are very sparse and/or inherently unable to provide temporal and spatial coverage of the global atmosphere at short time intervals. A unique opportunity to measure wind with global coverage of the atmosphere is offered by remote-sensing instruments mounted on spacecraft. Such instruments could provide observations even in those regions not covered by the conventional ground-based monitoring network (examples are the oceans and most of the Southern Hemisphere).

Efforts have been undertaken by various operational and research centers to assess quantitatively, by means of observing-system simulation experiments, the potential usefulness of a spaceborne global wind sensor and the observational requirements that must be met to forecast various atmospheric phenomena [12-14]. The cost, complexity, and spacecraft constraints indicate that satellite-based wind sensors would be most useful in monitoring only the large scale atmospheric motions driving the weather systems, while smaller scale motions may be more appropriately resolved by ground-based systems. It has been concluded that global, twice-daily measurements, with the accuracies and resolutions summarized in Table 1.1, would result in more accurate medium-range (up to five days) forecasts in the Northern Hemisphere, over which most of the conventional, ground-based wind sensors (rawinsonde network) in operation today are concentrated. A major impact is to be expected for forecasting in the sparsely instrumented Southern Hemisphere, where the usefulness of forecasts may be advanced by as much as 24 hours [15].

Table 1.1 Global and Synoptic Scale Observational Requirements

Horizontal resolution	100 km (meso-α scale)
Vertical resolution	1 km (0.5 km in the boundary layer and in the vicinity of the jet stream)
Temporal resolution	6 hour
Accuracy of the wind component	1-2 m/s in the lower troposphere 2-5 m/s in the upper troposphere
Directional accuracy	± 10 degree

Recognition that only a space-based monitoring system might have the capability to provide wind data throughout the troposphere on a global scale has prompted researchers to consider new remote wind-measuring techniques. A number of active and passive sensing instruments have been proposed, and some have already been experimentally tested [16-22]. Their main performance characteristics are listed in Table 1.2 [15]. It is apparent that most of these techniques are unable to satisfy the demands for increasing measurement accuracy at better horizontal and vertical resolutions. This is the case for all passive sensors and the scatterometers. On the other hand, excessive size and power consumption limit the utilization of Doppler radars for wind measurement from clear air in space.

Table 1.2. Characteristics of various spaceborne wind sensors

Instrument	Horizontal (km)	Vertical (km)	Temporal (h)	Accuracy (m/s)	Coverage	Limitations
Passive						
High-resolution Doppler imagers	125	4	24	< 5	Middle/upper troposphere; Stratosphere	Low reolution and accuracy; no troposphere coverage
Electro-optical modulation correlatiors	150	5	24	< 5	Stratosphere and mesosphere	Low resolution and accuracy; no troposphere coverage
Cloud-motion imagers	20-50	none	0.1 to 1	2	10,000 km^2	No global coverage. No vertial profiles
Active						
Doppler radars	10	0.2	< 0.1	1	In precipitating systems; regional	Excessive size and power consumption
Scatterometers	25	none	12	± 10%	Global oceanic surface	Low accuracy, no vertical profiles
Doppler lidars	100	0.2 to 1	12	1 to 3	Global troposphere	Immature technology; no coverage in cloudy regions

By comparing the performance of different instruments listed in Table 1.2, it can be concluded that Doppler Lidars are viable instruments able to provide, in the near future, wind information as a function of height in the troposphere from clear air regions. The information could be obtained on a global scale except for the cloudy regions, in a grid form suitable for use in operational meteorology, and with the required resolutions and accuracies [15]. Since the Doppler radars can also provide the required temporal and spatial resolutions, they can fill in the gaps in coverage of lidars caused by clouds and rain. Excessive power requirements for clear air Doppler radar systems limit the use of radars to wind measurements in cloudy regions or precipitation systems.

1.1.3 REQUIRED OBSERVATION RESOLUTIONS

Table 1.1 listed the observational requirements for global and synoptic scale required in numerical weather prediction modeling. Table 1.3 presents the observational resolution generally required to nowcast or forecast various mesoscale phenomena, as addressed in a variety of documents (e.g., Federal Coordinator for Meteorological Services and Supporting Research, 1982; The National Stormscale Operational and R research Meteorology (STORM) Program(NCAR, 1984); Shenk et at., 1985; National Environmental Satellite, Data, and Information Service, 1985). Typical phenomena associated with the meso-α, meso-β, and meso-γ scales shown in the table are as follows: meso-α scale corresponds to the initiation of a mesoscale convective system(MCS) (NCAR, 1984); meso-β scale describes the the internal structure of the MCS (NCAR, 1984), for example; and meso-γ scale corresponds to small phenomena such as the low-level wind shear (microbursts).

Table 1.3 Required Observational Resolution

	Characteristic Resolution		
	meso-α	meso-β	meso-γ
Horizontal	100 km	10 km	0.1 km
Vertical	25 mb	10 mb	10 mb
Temporal	1 hr	10 min	1 min

The last column in Table 1.3, meso-γ, is now generally referred to as microscale. It follows from Table 1.2 that satellite-based remote sensing platforms would be most helpful in meeting the temporal and spatial resolution requirements at the global and synoptic scale and the meso-α scale. For meso-β and meso-γ phenomena, ground-based systems such as the Doppler radar wind profilers [11] would be more useful. However, in some situations, geosynchronous-satellite cloud winds could be useful for meso-β events [15].

1.1.4 THE LAWS FROM EOS

Since the lidar systems are the most promising remote sensing instruments for global wind measurement in cloud-free areas, a spaceborne Doppler laser atmospheric wind sounder (LAWS) is under development as part of NASA's Earth Observing System (EOS) study [9]. This system is planned for a late-90s launch into low-Earth orbit on an EOS platform. It should make a strong scientific contribution to our understanding of the Earth as an integrated system.

The LAWS will measure the Doppler shift of line-of-sight components from aerosol backscattering in the atmosphere with a conically scanned optical arrangement. Successive measurements from different directions will provide global coverage of wind-vector profiles throughout the troposphere, on a spatial scale of 100 km by 100 km at 1 km height intervals, and with an expected accuracy better than 1 ms^{-1}. Precise management and scheduling of laser pulses should allow for more detailed examination of fine-scale meteorological features [23].

A set of instrument parameters for the lidar system was selected for a Space Shuttle orbit of 300 km and a near-polar orbit of 800 km (Huffaker, 1978, 1980). The parameters selected for use in the computer simulation are shown in the following table.

Table 1.4 Base parameters for a lidar wind sounder

	Space Shuttle Orbit	Near-Polar Orbit
Altitude	300 km	830 km
Target volume (patch)	300 × 300 × 20 km	300 × 300 × 20 km
Nadir angle	62°(600 km reach)	52°(1200 km reach)
Conical scan period	7 s	19 s
Wavelength	9.11 μm (C O_2)	
Telescope diameter	1.25 m	
Pulse duration	6.7 μs	
Optical-detector efficiency	10%	
rms Long-term pointing error	50 μrad	
rms Short-term pointing error	2 μrad	
Local Oscillator	50 kHz	

1.1.5 EFFECT ON LIDARS BY CLOUDS

A large portion of the globe is normally covered by clouds (about 40%), a major obstacle for the operation of LAWS. The cloud distribution is usually divided into three layers by meteorologists, (except the vertical clouds: Cumulonimbus or Cumulus). The low cloud layer covers the range from the Earth's surface to 2 km. These clouds include stratus, stratocumulus, and nimbostratus. The middle layer clouds are in the 2 km to 8 km range. These clouds include altostratus and altocumulus. The top layer clouds are in the 8 km to 20 km range. These clouds are called cirrus, cirrostratus and cirrocumulus. These clouds are generally opaque to lidar pulses, except for very thin clouds like cirrus.

The research done by Huffaker indicates that 77% of lidar pulses can penetrate the upper layer, or down to 8 km [17]. Of those that reach this level, 73% will penetrate the middle layer. Thus, only 57% of the transmitted pulses are expected to reach down to the 2 km altitude."Using global cloud statistics, the lidar system is not expected to be seriously affected provided that the laser prf is sufficiently high. Tropical storms and the warm sector in typical cyclonic storms will seriously affect lidar's performance."

1.2 THE DOPPLER RADAR WIND SOUNDER (RAWS)

The potential for Doppler radar use for global wind measurement acquisition was considered poor because of the large antenna aperture and power requirements. However, if the Doppler radar is restricted to measuring the wind field inside a cloud system, it can provide valuable complementary information for the lidar system. In addition, such a system can also provide measurements for rainfall rate and ocean surface winds.

A radar wind sounder (RAWS) is proposed as a multipurpose instrument with a scanning pattern similar to LAWS that could measure the winds in the cloudy areas [24]. This radar would serve as a complement to the LAWS, which must work in clear air or where clouds are thin. Frequencies in X band or Ku band are appropriate where precipitation is present, but clouds require higher frequencies because cloud drops are very small. More power is needed for clouds than for rain alone, but this will be available in future unmanned spacecraft with robust power sources.

1.3 DISSERTATION OUTLINE

As an initial step in the study of RAWS, this dissertation is intended to investigate several key problems in implementing a Doppler radar wind sounder. Several key problems addressed in this study are listed as follows:

- Radar backscatter cross section for water clouds and ice clouds. This involves modeling of cloud drop-size distributions and water content, and computer simulation of backscattering coefficients from different types of clouds.
- Conceptual design of the system and an analysis of error bound
  - system parameters
  - tracking of satellite speed
  - simulation of signal to noise ratios
- Algorithms for accurately estimating the moments of the frequency spectrum of radar echoes.
- Algorithms to resolve the frequency ambiguity and range ambiguity problems.

In Chapter 2, we review, as background, the theory of radar scattering from particles and clouds, as well as drop-size distributions of water droplets in clouds. Computer simulations for a conceptual system are performed to calculate the signal to noise ratios for different types of clouds.

In Chapter 3, we discuss the basic system parameters of a proposed RAWS, as well as problems of antenna scan and compensation of the Doppler shift caused by satellite motion. In addition, we carry out the analysis of error bounds for estimating the wind field for specific situations.

In Chapter 4, various algorithms for estimating the first moment of the Doppler spectrum are discussed. Computer simulations are used to evaluate the performance of these algorithms.

In Chapter 5, radar ambiguity functions are used in analysis of algorithms for removal of frequency and range ambiguities. An algorithm using different waveform modulations to transmitted pulses is develped to solve the radar ambiguity problems of Doppler radars. Again, computer simulations are used in this chapter to compare the performance of the algorithms discussed .

Chapter 2

Radar Backscatter and Attenuation From Clouds

2.1 SCATTERING FROM CLOUDS

In this chapter, we review some of the concepts of radar backscattering from particles, as well as some of the models of drop-size distributions of clouds. We use computer simulations to estimate signal-to-noise ratios (SNRs) of radar echoes scattered from some cloud models. The radar system used in the computer simulation is a spaceborne Doppler radar wind sounder that is discussed in more detail in Chapter 3. Three types of cloud models were selected in the computer simulations, according to their mean drop sizes and water contents. The results of the simulations are presented as functions of signal-to-noise ratio of radar echo, cloud type, and penetration into the clouds.

2.1.1 DEFINITIONS OF RADAR CROSS SECTIONS

Assume S_i is the power density (W m^{-2}) of an electromagnetic wave incident upon a suspended material particle of geometrical cross sectional area $A = \pi r^2$. A fraction of the incident power is absorbed by the particle, and an additional fraction is scattered by the particle in all directions. The ratio of absorbed power P_a to incident power density S_i is known as the absorption cross section

$$Q_a = \frac{P_a}{S_i} \qquad m^2 \qquad (2.1)$$

Furthermore, the absorption efficiency is defined as the ratio of the absorption cross section to the physical cross section of the particle:

$$\xi_a = \frac{Q_a}{\pi r^2} \qquad (2.2)$$

In addition to absorption, a portion of the incident power is scattered by the particle. The scattering cross-section of the particle, Q_s, is defined as the ratio of the scattered power P_s and the incident power density S_i

$$Q_s = \frac{P_s}{S_i} \qquad m^2 \qquad (2.3)$$

and accordingly the scattering efficiency is defined

$$\xi_s = \frac{Q_s}{\pi r^2} \qquad (2.4)$$

Both absorption and scattering reduce the incident power density. The extinction cross-section Q_e, denoting the total power removed by the particle, is defined as the sum of the absorption cross-section and the scattering cross section:

$$Q_e = Q_a + Q_s \qquad m^2 \qquad (2.5)$$

The extinction efficiency ξ_e is defined as

$$\xi_e = \xi_\alpha + \xi_s \qquad (2.6)$$

To calculate the power of the radar echoes, knowledge of the backscatter cross-section is required. If the back-scattered power density is denoted as S_b, the radar backscatter cross-section σ_b is defined such that the product of σ_b and the incident power density S_i is equal to the total power radiated by an equivalent isotopic radiator with power density equal to S_b. Therefore, at a distance R from the scatterer, the backscatter power density S_b is given as [25]:

$$S_b = S_i \frac{\sigma_b}{4\pi R^2} \qquad (2.7)$$

From equation (2.7), the backscatter cross-section of the scatteerr is equal to

$$\sigma_b = 4\pi R^2 \frac{S_b}{S_i} \qquad m^2 \qquad (2.8)$$

2.1.2 SCATTER FROM A SINGLE SPHERICAL PARTICLE

Radar cross-sections for objects of almost any shape are difficult to calculate. However, the solution for the scattering and absorption of electromagnetic waves by a dielectric sphere of arbitrary radius r was derived by Mie [26]. The results for the scattering coefficients and absorption coefficients were presented in the form of a converging series:

$$\xi s(n, \chi) = \frac{2}{\chi^2} \sum_{k=0}^{+\infty} (2k+1)(|a_k|^2 + |b_k|^2) \qquad (2.9)$$

and

$$\xi e(n, \chi) = \frac{2}{\chi^2} \sum_{k=0}^{+\infty} (2k+1)\, \mathrm{Re}(a_k + b_k) \qquad (2.10)$$

where χ and n are defined as follows

$$\chi = k_b\, r = \frac{2\pi r}{\lambda_b} = \frac{2\pi r}{\lambda_0} \sqrt{\varepsilon_{rb}}$$

and

$$n = \frac{n_p}{n_b} = \left(\frac{\varepsilon_{cp}}{\varepsilon_{cb}}\right)^{1/2}$$

with

k_b = the wave number in the background medium
ε_{rb} = the real part of the relative dielectric constant of the background medium
λ_b = the wave length in the background medium
λ_0 = the free space wave length
n_p = the complex index of refraction of the particle
n_b = the complex index of refraction of the background medium
ε_{cp} = the complex dielectric constant of particle
ε_{cb} = the complex dielectric constant of background medium

The terms a_k and b_k, known as the Mie coefficients, are functions of n and χ, and given by Stratton[27] , Battan[28] , and many others. When the background medium is air, then $\varepsilon_{rb} = 1$ and $\lambda_b = \lambda_0$.

2.1.3 RAYLEIGH APPROXIMATION

When the radius of the particles is considerably smaller than the wavelength of the incident wave, specifically when $|np\chi| \ll 1$, the Mie expressions for ξ_s and ξ_e can be expressed by the Rayleigh approximations (in which only the first and second terms of the Mie solutions are considered) [28]:

$$\xi_s = (8/3)\chi^4 \, |K|^2 \tag{2.11}$$

and

$$\xi_e = 4\chi \, \mathrm{Im}(-K) + 8/3\,\chi^4 \, |K|^2 + \ldots \tag{2.12}$$

where

$$K = \frac{n^2 - 1}{n^2 + 2} = \frac{\varepsilon_c - 1}{\varepsilon_c + 2} \tag{2.13}$$

n is the complex index of refraction of the droplet to the background medium, and ε_c the complex dielectric constant of the droplet relative to the background medium. From (2.12) and (2.13), the absorption efficiency ξ_a can be written as

$$\xi_a = \xi_e - \xi_s = 4\chi \, \mathrm{Im}(-K) \tag{2.14}$$

The corresponding scattering and absorption cross-sections for a single spherical particle are

$$Q_s = \frac{2\lambda^2}{3\pi} \chi^6 \, |K|^2 \qquad m^2 \tag{2.15}$$

$$Q_a = \frac{\lambda^2}{\pi} \chi^3 \, \mathrm{Im}(-K) \qquad m^2 \tag{2.16}$$

The backscatter efficiency ξ_b in the Rayleigh region is [25] :

$$\xi_b = 4\chi^4 |K|^2 \tag{2.17}$$

Therefore, in the Rayleigh region, the backscattering cross-section of an individual spherical particle of radius r is equal to

$$\sigma_b = \pi r^2 \xi_b = \frac{64\pi^5}{\lambda^4} r^6 \, |K|^2 \qquad m^2 \tag{2.18}$$

The Rayleigh approximations of scattering, absorption, and backscattering coefficients are useful in calculating signal-to-noise ratios for radar echoes. The only values we need to know are $|K|^2$ and Im(-K). For water droplets, values of $|K|^2$ and Im (-K) are known for various temperatures and wavelengths: $|K|^2$ is approximately equal to 0.9 for frequencies from 3 GHz to 30 GHz, and temperatures from 0°C to 20°C, while Im(-K) increases with frequency [25]. Some of the values of $|K|^2$ and Im(-K) for different frequencies and temperature are listed in Table 2.1 (Table 4.1, Battan[28]).

The Rayleigh approximation is not always applicable, especially when the diameter of the particle is large compared with the wavelength; however, it has been shown that the Rayleigh approximation is valid when $|n_p \chi| \leq 0.5$. Since, the absolute value of refractive index of a water droplet, $|n_w|$ decreases with increasing frequency from 1 GHz to 300 GHz [25], the Rayleigh condition $|n_w \chi| < 0.5$ can be satisfied for increasingly larger values of χ as frequency increases. The Mie extinction and scattering efficiencies, ξ_e and ξ_s, are shown in Figures 2.1 a, b and c as functions of drop radius r [29]. The three figures, corresponding to 3, 30, and 300 GHz, also include dashed lines which represent the Rayleigh extinction efficiencies.

Table 2.1 $|K|^2$ and Im(-K) for Clouds (Table 4.1, Battan [28])

Quality	Temperature °C	Frequency (GHz) 10	 24.1	 35.5
$\|K\|^2$	20	0.9270	0.9193	0.9100
	10	0.9282	0.9152	0.9045
	0	0.9300	0.9055	0.9000
	-8		0.8902	
Im(-K)	20	0.0188	0.0471	0.06745
	10	0.0247	0.0615	0.08565
	0	0.0335	0.0807	0.10970
	-8		0.1036	

The heavy horizontal lines in Figure 2.1 indicate the ranges of drop radii characteristic of two types of water clouds and a rain cloud with a rain rate of 25.4 mm hr^{-1}. At 3 GHz, the Rayleigh approximation is certainly applicable for the water clouds and is approximately valid for the rain cloud, while at 30 GHz, the approximation is valid only for the water clouds. At 300 GHz, the approximation is valid only for the fair-weather cloud.

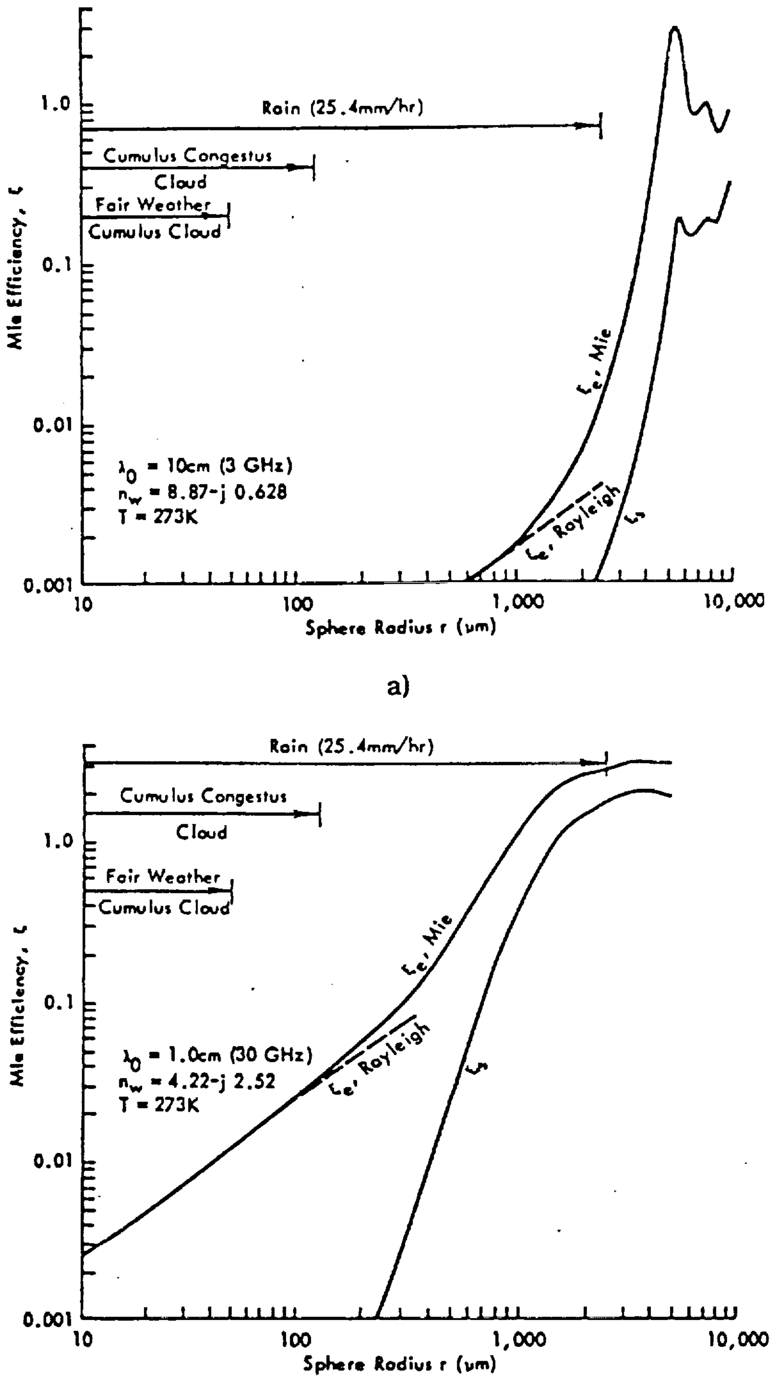

a)

b)

Figure 2.1. Mie efficiency factors for scattering and extinction by a water sphere as a function of drop radius (Fraser et al., 1975 Am. Soc. Photogram. [29]). Horizontal arrows indicate drop radii; a) at 3 GHz; b) at 30 GHz; c) at 300 GHz.

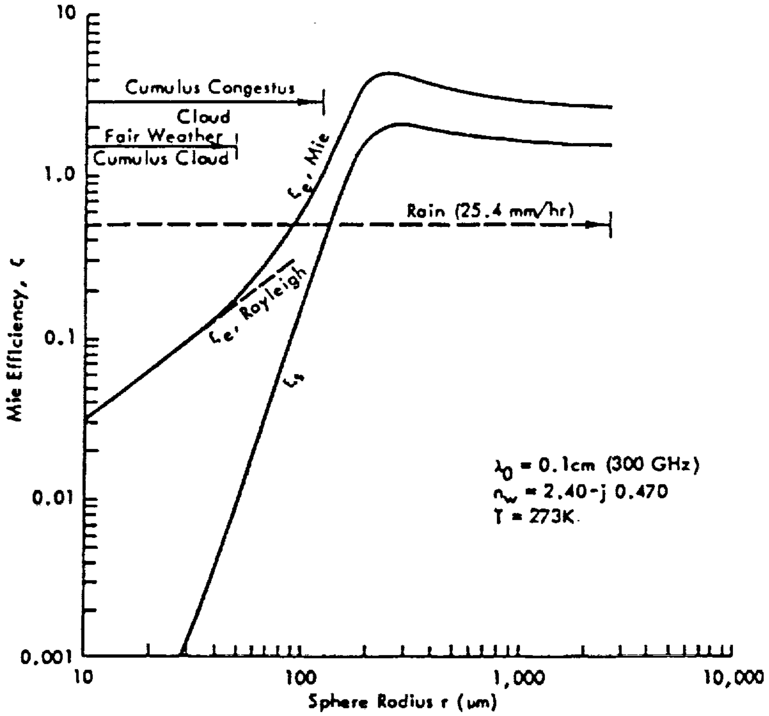

c)

Ice clouds may contain particles with radii up to about 0.2 mm, but the refractive index of ice is smaller than that of water. The combination of these two factors leads to the conclusion that, for an ice cloud, the Rayleigh criterion is applicable up to about 70 GHz for computing ξ_e, and up to 200 GHz for computing ξ_b [25].

2.1.4 VOLUME SCATTER

In a resolution volume in clouds, the scatterers (water droplets or ice particles) are assumed to be randomly distributed within the volume such that there are no coherent phase relationships between the fields scattered by the individual particles. Additionally, the concentration of particles is usually small enough to support the assumption that the shadowing of one particle by another may be ignored. These two assumptions lead to the conclusion that the total scatter cross-section of a given volume is equal to the algebraic sum of the scatter cross-sections of all of the individual particles contained within that volume. Similar statements may be made regarding the absorption and backscattering cross sections.

2.1.4.1 VOLUME SCATTERING COEFFICIENT

The volume scattering coefficient κ_s represents the total scattering cross-section per unit volume, and has units of Np $m^{-3} \times m^2$=Np m^{-1}. The volume-scattering coefficient k_s is given by

$$\kappa_s = \int_{r_{min}}^{r_{max}} p(r)\, Q_s(r)\, dr \qquad \text{Np m}^{-1} \qquad (2.19)$$

where p(r) represents the number of water droplets per-unit volume per increment of r, Q_s is the scattering cross section for a droplet with radius r. In the Rayleigh region, equation (2.19) can be expressed in a summation form

$$\kappa_s = \frac{2\pi^5}{\lambda^4} |K|^2 \sum_{i=1}^{N} D_i^6 \qquad \text{Np m}^{-1} \qquad (2.20)$$

where N is the total concentration of the droplets in a unit volume of the cloud and D_i is the diameter of i^{th} droplet in the unit volume.

2.1.4.2 VOLUME ABSORPTION COEFFICIENT

Similar to the volume scattering coefficient, the volume absorption coefficient is defined as

$$\kappa_a = \int_{r_{min}}^{r_{max}} p(r)\, Q_a(r)\, dr \qquad \text{Np m}^{-1} \qquad (2.21)$$

In the Rayleigh region, the absorption coefficient can be expressed as

$$\kappa_a = \frac{\pi^2}{\lambda} \mathrm{Im}(-K) \sum_{i=1}^{N} D_i^3 \qquad \mathrm{Np\,m^{-1}} \tag{2.22}$$

Using the following relationship

$$m_v = 10^6 \times \frac{\pi}{6} \sum_{i=1}^{N} D_i^3 \qquad \mathrm{g\,m^{-3}}$$

where m_v represents the water content in a cubic meter volume in clouds (the fractional volume occupied by the particles multiplied by the density of water(= 10^6 gm^{-3}), the volume absorption coefficient can be written as:

$$\kappa_a = 6\pi/\lambda\, \mathrm{Im}(-K)\ m_v\, 10^{-6} \qquad \mathrm{Np\,m^{-1}} \tag{2.23}$$

2.1.4.3 VOLUME EXTINCTION COEFFICIENT

For water and ice drops in clouds, the absorption cross-section Q_a is much larger than the scattering cross-section Q_s in the Rayleigh region since Q_a is proportional to r^3 while Q_s is proportional to r^6. This fact can be observed from Figure 2.1. The cloud volume extinction coefficient κ_e as the sum of κ_s and κ_a is therefore approximately equal to the volume absorption coefficient κ_a, and can be calculated with equations (2.22) and (2.23).

2.1.4.4 VOLUME BACKSCATTERING COEFFICIENT

Similar to the definitions of scattering cross-section and absorption cross-section, the volume backscattering cross-section is defined as a summation of backscattering cross sections of individual drops in a unit volume

$$\sigma_{vc} = \frac{\pi^5}{\lambda^4} |K|^2 \sum_{i=1}^{N} D_i^6 \qquad m^{-1}$$

$$= 10^{-18} \frac{\pi^5}{\lambda^4} |K|^2 Z \qquad m^{-1} \qquad (2.24)$$

where Z is the reflectivity factor (a quantity widely used in the meteorology community) in units of $mm^6\ m^{-3}$.

Backscatter from turbulent fluctuations in the refractive index of the medium adds to the echo power. However, since the contribution of this type of backscatter is quite small when compared to the droplet backscatter, it can be neglected. In addition to the attenuation caused by water droplets in clouds, radio waves also suffer attenuation caused by absorption of atmospheric gases. This attenuation is mainly caused by the existence of absorption lines of oxygen and water vapor in the atmosphere. Oxygen has an isolated absorption line at 118.74 GHz and a series of close lines between 50 and 70 GHz which act as a continuous absorption band. Water vapor has three absorption lines at frequencies of 22.3 GHz, 183.3 GHz, and 323.8 GHz. As a result, the atmosphere contains a number of "windows" where the attenuation of radio waves by atmospheric gases is small. The total attenuations caused by absorption of gases as a function of incident angle between 20 MHz and 50 GHz are shown in Figure 2.2 [30].

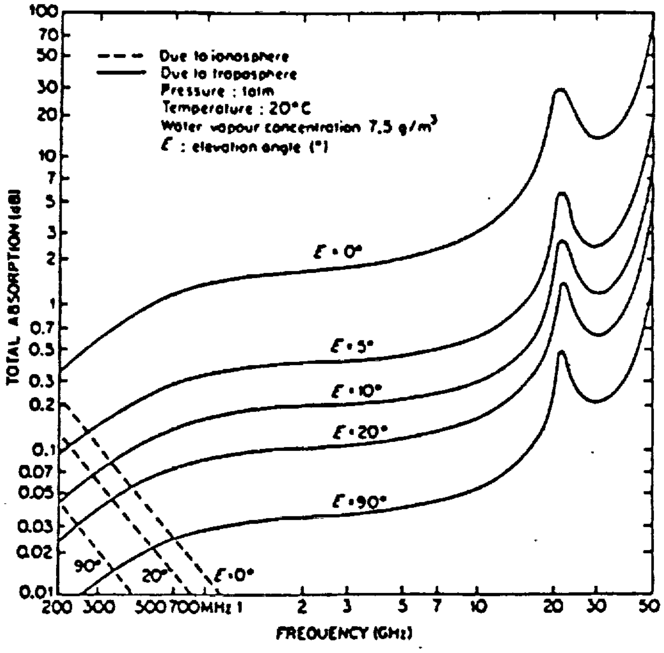

Figure 2.2. Total attenuation of radio waves by atmospheric gases versus frequency for various elevation angles (from [30]).

2.1.5 RADAR EQUATION

The weather radar equation can be stated as follows [31]

$$P_r = \left[\frac{c}{1024\pi^2 \ln 2} P_t \tau \lambda^2 G^2 \theta \phi L_t L_r \frac{1}{r^2} \right] \eta$$

$$\exp\left\{ -2 \int_0^h (\kappa_g + \kappa_p + \kappa_c) \right\} dh \qquad (2.25)$$

where

c = the speed of light
P_r = the received signal power
P_t = the transmitted peak power
τ = the expanded pulse width if the chirp technique is applied

λ = the wavelength
G = the antenna gain
θ = the horizontal beamwidth
ϕ = the vertical beam width
L_t = the transmitter loss
L_r = the receiver loss including filters
r = the distance from the radar to the target
κ_g = the extinction coefficient due to gas
k_p = the extinction coefficient due to rain or snow
κ_c = the extinction coefficient due to clouds
(in the Rayleigh region, it is equal to κ_s, the scatter coefficient)
h = the depth of the radar signal penetration into the cloud
η = the volume scatter coefficient

The total attenuation caused by the atmospheric gases is dependent upon the pointing angle of the antenna and the operating frequency. At a pointing angle of 30 - 35 degrees and frequency of 35 GHz, the total loss is less than 0.5 dB, as shown in Figure 2.2. κ_p and κ_c are dependent upon cloud type and can be calculated using equation (2.22) or (2.23).

2.2 MODELS OF DROP-SIZE DISTRIBUTION IN CLOUDS

2.2.1 CONTENTS OF CLOUDS

Cloud droplets are usually formed by water vapor condensing on particulate which serve as condensation nuclei. Supersaturation (humidity of >100%) is required to condense water vapor in pure air. For a visible cloud, the droplet's diameter is > 5 micrometers. The concentration of water droplets in clouds is on the order of 100 per cubic centimeter and typical radii are about 10 µm. This structure is extremely stable as a rule, and the droplets show little tendency to come together or to change their sizes except by general growth of the whole population [32]. In addition to mean radius of droplets, total concentration and water content per-cubic meter are other important parameters used to classify cloud.s In non-precipitating cumulus, a typical value for water content is 0.59 gm^{-3}, with peak values of about 1g m^{-3}. In stratus clouds, the values tend to be smaller. In cumulonimbus clouds, the water contents can exceed 5 gm^{-3}.

In addition to water droplets, clouds often contain ice particles when the temperature is low. However, observations show that the 0°C level in the atmosphere does not induce a sharp discontinuity in the microstructure of clouds and precipitation. Clouds have a high probability of containing no ice if the temperature of the cloud is warmer than -10°C. However, with decreasing temperature the likelihood of ice increases: below -20°C, more than 90 percent of the clouds contain ice particles [33].

2.2.2 DROPLET SIZE DISTRIBUTION OF WATER CLOUD

Many cloud physicists have published results of measurements of drop-size distributions or liquid-water contents, or both, in various types of cloud and fog. Some of these results are shown in Figures 2.3, 2.4, and 2.5. These examples show that most drop-size distributions measured in many different types of cloud under a variety of meteorological conditions exhibit a characteristic shape. Generally, the concentration rises sharply from a low value to a maximum, and then decreases gently toward larger sizes; thus, the distribution becomes positively skewed with a long tail toward the larger sizes. Such a characteristic can be approximated reasonably well by some analytical formulas [34-35]:

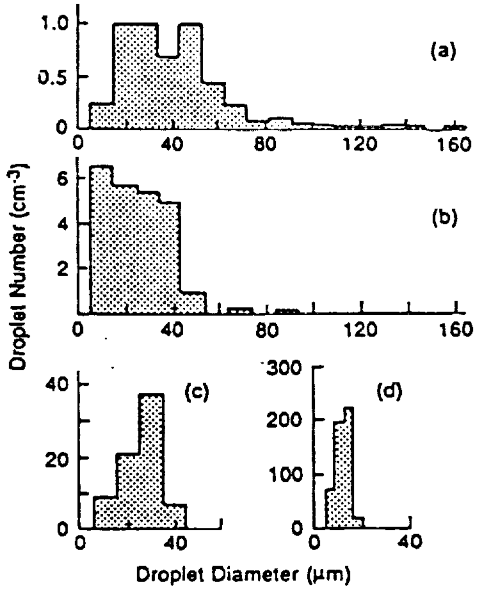

Figure 2.3. Measured drop-diameter histograms for different kinds of clouds. Note the change in ordinate scale from part to part. Note significant numbers of large drops in all but (d). (a) Orographic cloud, Hawaii, ρ = 0.4 gm-3. (b) Dark stratus over Hilo, HI, ρ = 0.34 gm-3. (c) Tradewind cumulus over Pacific near Hawaii, 615 m above base, ρ = 0.5 gm-3. (d) Continental cumulus over Blue Mountains near Sydney, Australia, 615 m above base, ρ = 0.35 gm-3 (From [35])

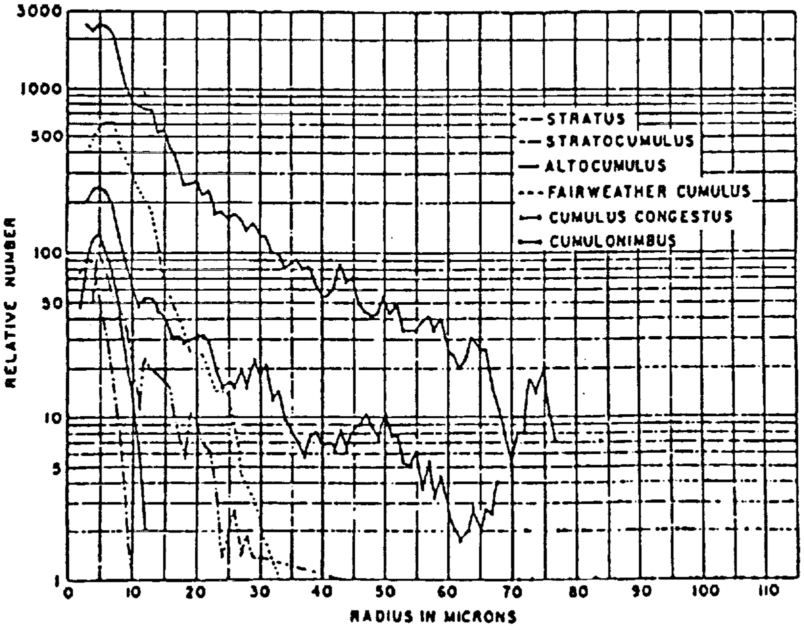

Figure 2.4. Average cloud-drop spectra reported by aufm Kampe and Weickmann for different cloud types. Note the large number of large drops present in the cumulus congestus and cumulonimbus clouds (from [35]).

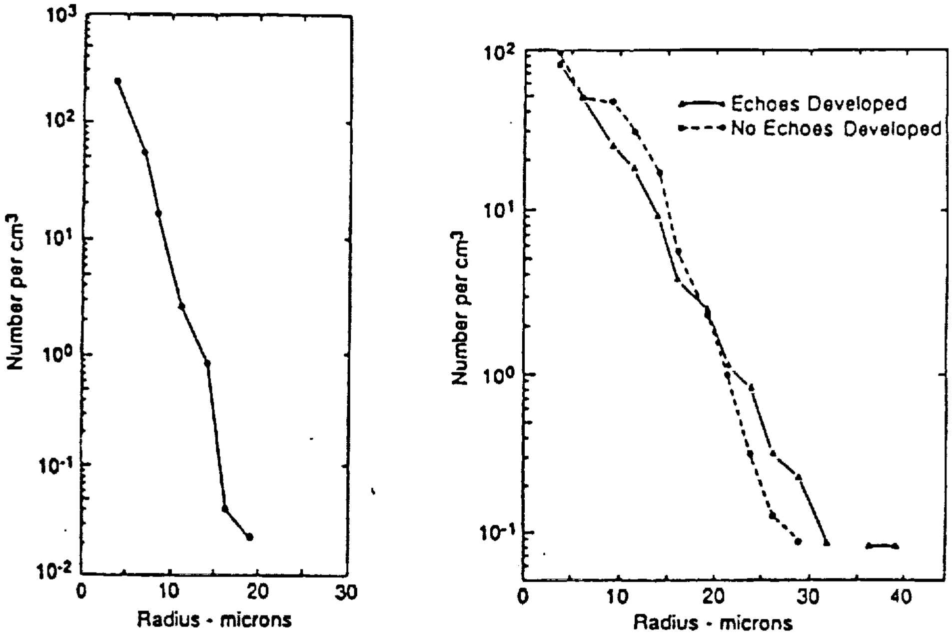

Figure 2.5. Distribution of drop radii for summer convective clouds over the U.S. based on work of Battan and Reitan. Left: 19 fair-weather cumulus clouds with average of 293 drops cm-3. Right: cumulus congestus for two cases: arrested growth with 247 drops cm-3 and those growing to point where 1950s weather radar showed echoes with 188 drops cm-3 (from [35]).

LOG NORMAL DISTRIBUTION

$$n(a) = \frac{1}{\sigma\sqrt{2\pi a}} \exp\left\{ -\frac{\ln^2(a/a_m)}{2\sigma^2} \right\} \qquad (2.26)$$

where a is drop radius, a_m is the median drop radius and σ is the root mean square (RMS) deviation of the logarithm of the drop radius.

MODIFIED GAMMA DISTRIBUTION

$$n(a) = A\, a^{\beta}\, e^{-Ba^{\gamma}} \qquad (2.27)$$

where A, B, β, γ are positive parameters. The maximum of this distribution occurs at a_m, an observable quantity which relates the parameters of the distribution to

$$\beta = B \gamma a_m^{\gamma}$$

A constraint is imposed on equation (2.27) in terms of the total concentration N.

$$N = \frac{AB^{-(\beta+1)/\gamma}}{\gamma} \Gamma((\beta + 1)/\gamma) \tag{2.28}$$

KHRIGIAN AND MAZIN DISTRIBUTION

The Khrigian-Mazin drop-size distribution is a special case of the modified Gamma distribution [34], which can be expressed as

$$n(a) = A\, a^2\, e^{(-B\, a)} \tag{2.29}$$

The parameters A and B can be related to the first and second moments of the distribution:

$$N = \int_{r_{min}}^{r_{max}} n(a)\, da = \frac{2A}{B^3} \tag{2.30}$$

and

$$<a> = 1/N \int_{rmin}^{rmax} a\, n(a)\, da = 3\, /B \tag{2.31}$$

where <a> is the mean radius of drop size. Another related quantity of interest is the water content, W_L. For the Khrigian-Mazin distribution,

$$A = 1.45 \times 10^{18} \frac{W_L}{\rho <a>^6} \tag{2.32}$$

$$N = 1.07 \times 10^5 \frac{W_L}{\rho <a>^3} \qquad \text{Number of Drops} \tag{2.33}$$

$$W_L = 0.934579 \times 10^{-5} \times N \rho <a>^3 \ \ g\,m^{-3} \tag{2.34}$$

where <a> is in μm, ρ is in g cm^{-3}, W_L is in gm^{-3} and N is in number of drops per cm^3.

The Khrigian-Mazin distribution is very convenient to be used in computer simulation of cloud drop size distributions and calculation of water contents of clouds while the modified Gamma distribution may give overflow problems in simulating drop-size distributions or some types of cloud. The log-normal distribution does not have the simple relationships between the total concentration of droplets, the water contents, and the mean radius like the other distributions. However, all of the analytical expressions given represent only average distributions. Individual drop-size spectra may be significantly different. Figure 2.6 shows computer simulated Khrigian-Mazin Drop size distributions for three different types of clouds. These three models of clouds are classified as thin, medium, and heavy according to their water contents per-unit volume.

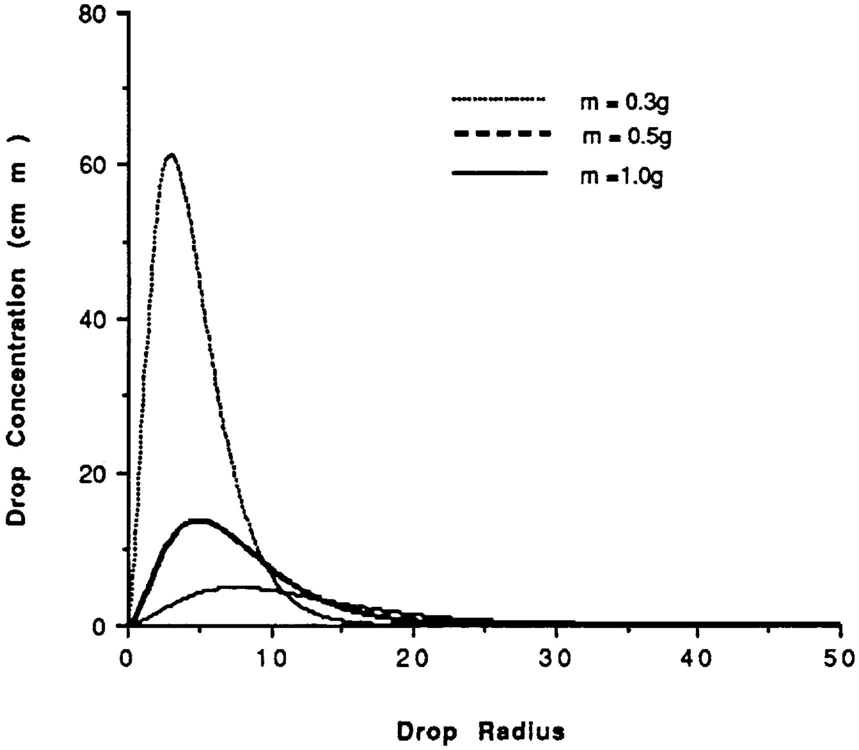

Figure 2.6. Computer simulated drop-size-distributions of three different types of clouds 0.3, 0.5, and 1.0 gm^{-3} (thin, medium and heavy).

In general, when the drop size increases, the concentration of droplets decreases. The following parameters may be helpful in cloud modeling [32]:

Table 2.2. Some Typical Parameters for Clouds

Droplet Type	Mean Radius (μm)	Concentration of Droplets (per liter)	Falling Velocity cm s^{-1}
Typical Cloud Drop	10	10^6	1
Large Cloud Drop	50	10^3	27
Typical Rain Drop	1000	1	650

2.2.3 ICE CLOUD MODELING

The drop size distributions of ice crystals in clouds are not as well known as those for water droplets. With the average size of the ice crystals under many conditions being considerably large and their shapes irregular and usually far from spherical, it is difficult to model an ice cloud. Ice crystals in ice clouds can attain sizes an order of magnitude larger than water droplets found in water clouds. Hence, the reflectivity factor Z_i of an ice cloud may be several orders of magnitude larger than that of a water cloud with the same liquid water content m_v.

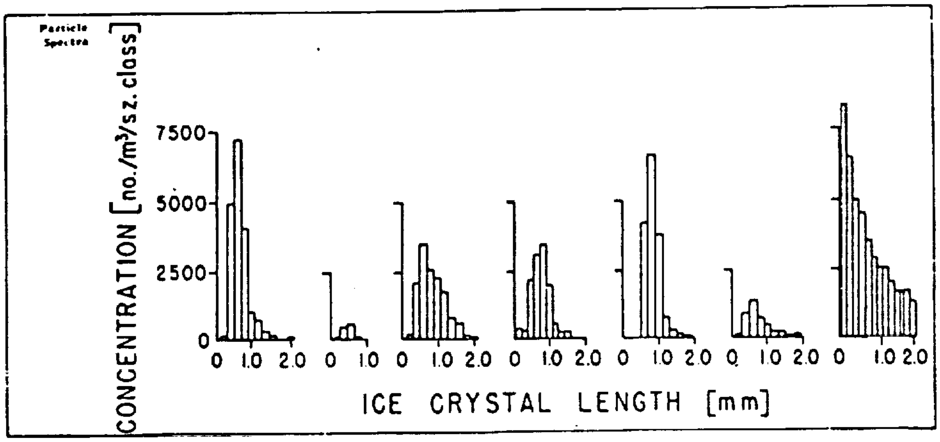

Figure 2.7. Average ice crystal spectra in a) Ci Spi, b) AS, c) and d) Ci unc, e) Cs, f) Ac and g) Cb cap. The size class is 200 μ (From [36]).

The water content of a cloud is typically less than 1 gm-3 and rarely exceeds 4 gm-3. The factor $|K_w|^2$ for water varies between 0.89 and 0.93 over the 0-20 °C temperature range and 1-10 cm wavelength range. For ice, $|K_i|^2$ is about 0.2, which is 4.5 times smaller than $|K_w|^2$, but because of the much larger Z_i (in comparison to Z_w), ice clouds are much more readily detectable by radar than water clouds.

Figure 2.7 shows some averaged ice crystal spectra in different cloud types measured by Heymsfield and Knowllenberg [36]. For cirrus clouds, Heymsfield and Knollenberg measured the following average characteristics:

- ice crystal concentration 1.0×10^4 to 2.5×10^4 m^{-3}
- mean crystal length 6.0×10^{-2} to 1.0×10^{-1} cm
- ice-water content 0.15 - 0.25 gm^{-3}
- radar reflectivity factor 5.0 - 20.0 mm^6 m^{-3}
- precipitation rate 0.5 - 0.7 mm hr^{-1}

2.3 COMPUTER SIMULATIONS AND CONCLUSIONS

Most of the early experiments used 10 cm to 3 cm radars that could only detect drops larger than a few hundred microns in diameter. More recent high-power 3-cm radars, and most 1-cm radars, permit the detection of drops with diameters larger than a few tens of microns. A majority of this work has shown that the appearance of the radar echo is characteristically related to the cloud dimensions and temperatures [37-38]. There is a correlation between the number of echoes and the cloud dimension and top temperature. Larger clouds produced more radar echoes. Similarly, louds with colder cloud top temperatures also produced more radar echoes. The explanation for this phenomena is that the large clouds tend to have a broader spectra of drop sizes and greater Z factors with the same mean drop size and water content. Cold cloud temperatures indicate that the clouds may contain ice particles and therefore have large reflectivity factors.

2.3.1 COMPUTER SIMULATIONS OF SNR OF RADAR ECHOES

Three cloud types, rated as thin, medium and heavy according to their water contents and mean drop sizes, have been selected in the computer simulations. Their water contents and mean drop-radii are listed in Table 2.3. The basic purpose of these computer simulations was to examine the signal to noise ratio of radar echoes from different cloud types as a function of cloud penetration, frequency and reflectivity factor.

Table 2.3. Parameters In Cloud Modeling

Type of Cloud	Water Content $g\ m^{-3}$	Mean Drop Radius μm
Thin Cloud	0.3	4.5
Medium Cloud	0.5	7.5
Heavy Cloud	1.0	11.6

A menu-driven simulator was developed, which allows the user to set up parameters, such as frequency, antenna gain, altitude, signal-to-noise ratio, cloud models, etc., from popup menus. The parameters for the radar system used in the simulations are listed in Table 2.4. A detailed discussion of these parameters is presented in Chapter 3.

Table 2.4. Parameters Used in Computer Simulation

Parameter	35 GHz	10 GHz
Antenna Gain	68 dB	57 dB
Beamwidth	0.00122 rad	0.00427 rad
Peak Power	3000 W	3000 W
Pulse Length (chirped)	1 μs	1 μs
Chirp Gain	20	20
Pointing Angle	30 deg	30 deg
Transmitter Loss	1.5 dB	1.5 dB
Receiver Loss	1.5 dB	1.5 dB
Noise Figure	4 dB	4 dB
Im(-K)	0.08565	0.0247
K^2	0.9	0.9

SIGNAL-TO-NOISE RATIO VERSUS CLOUD DEPTHS AND CLOUD TYPES

Using the parameters given in Table 2.4, computer simulations of signal-to-noise ratio (SNR) versus cloud depth were performed for different types of clouds, frequencies, and altitudes of orbits. The mean radius of droplets, drop concentration, and water contents of a cloud are not independent. An example of the correlation between these values ishown in Figure 2.8 [35]. From this figure, an experimental formula was derived that relates the mean drop size and the water content in a cloud.

$$r = 11.6 + 13.5 * \log(W) \tag{2.39}$$

where r is mean radius, and W is water content. This equation is only used for the purpose of computer simulations of cloud drop-size distribution in this chapter. The actual clouds may have a much different relationship than (2.39).

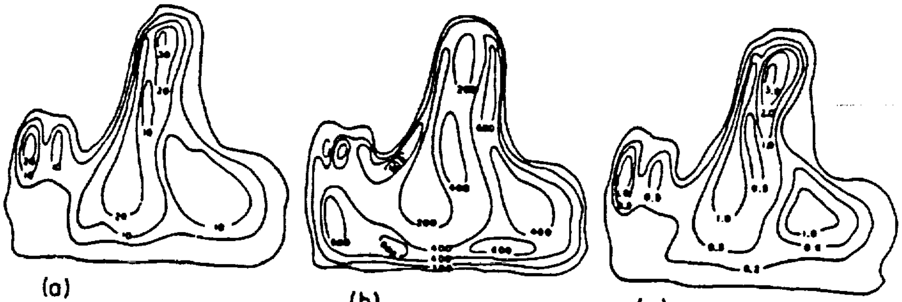
(a) (b) (c)

Figure 2.8. Spatial distribution of microstructure parameters in cumulus cloud. (a) drop diameter (μm), (b) drop concentration (number cm^{-3}), (c) W_L (gm^{-3}) (from [35]).

The results presented in Figures 2.9 to 2.11 show that, for water clouds, the return signal from cloud tops at 35-GHz is much larger than at 10-GHz. This is due to the fact that the 35 GHz system has a higher antenna gain and larger backscatter coefficients than the 10 GHz system does.

Figure 2.9 shows the signal-to-noise ratio for the "thin" cloud type (like fair-weather cumulus). In this condition, the radar echo is weak even at 35 GHz: 5 dB SNR at a 300-km orbit, and below zero dB at a 800 km orbit. For the 10-GHz system, the signal is too weak to be useful in measurement of wind vectors from clouds. Figure 2.10 shows the signal-to-noise ratios from a medium cloud, with water content 0.5 gm^{-3}.; the signal-to-noise ratios increase substantially (about 10 dB) as the water content increases from 0.3 gm^{-3} to 0.5 $gm^{-0.3}$. In this case, at both the 300-km and the 830-km orbits, the 35-GHz system is able to provide high enough SNRs for measuring Doppler frequencies. As for 0.3 gm^{-3}, the 10-GHz system cannot provide high enough SNR. Figure 2.11 shows the signal return from a heavy cloud with water content 1.0 gm^{-3}. The SNR's at both frequencies are further increased; even at 10 GHz the SNR is above 0 dB for the 300-km orbit.

From these results, it can be concluded that a frequency of 35 GHz or higher is required for measuring moments of Doppler spectra of radar echoes from a majority of water clouds, as well as ice clouds. Although the 10-GHz system shows greater penetrations than the 35-GHz system, especially in the heavy cloud (1.0 gm^{-3}), it is limited for wind measurement in clouds from space because of low SNR and wide antenna beamwidth (as we will see in Chapter 3). A frequency around 10 GHz can be used for measuring wind in rain. The rain may cause too much attenuation for 35 GHz or higher. In addition, the 10-GHz radar can also determine ocean surface wind fields.

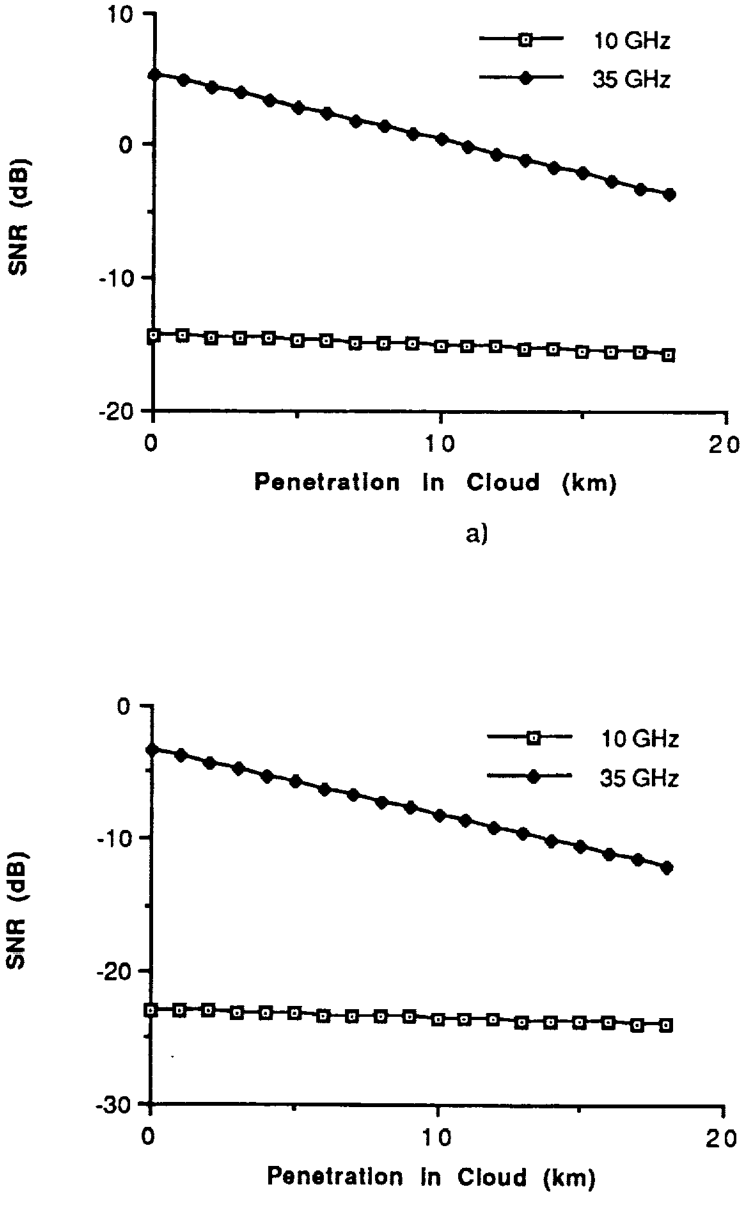

Figure 2.9. Signal to noise ratio of radar echo as a function of cloud penetration (water content of cloud = 0.3 gm^{-3}); a) orbit height = 300 km; b) orbit height = 830 km.

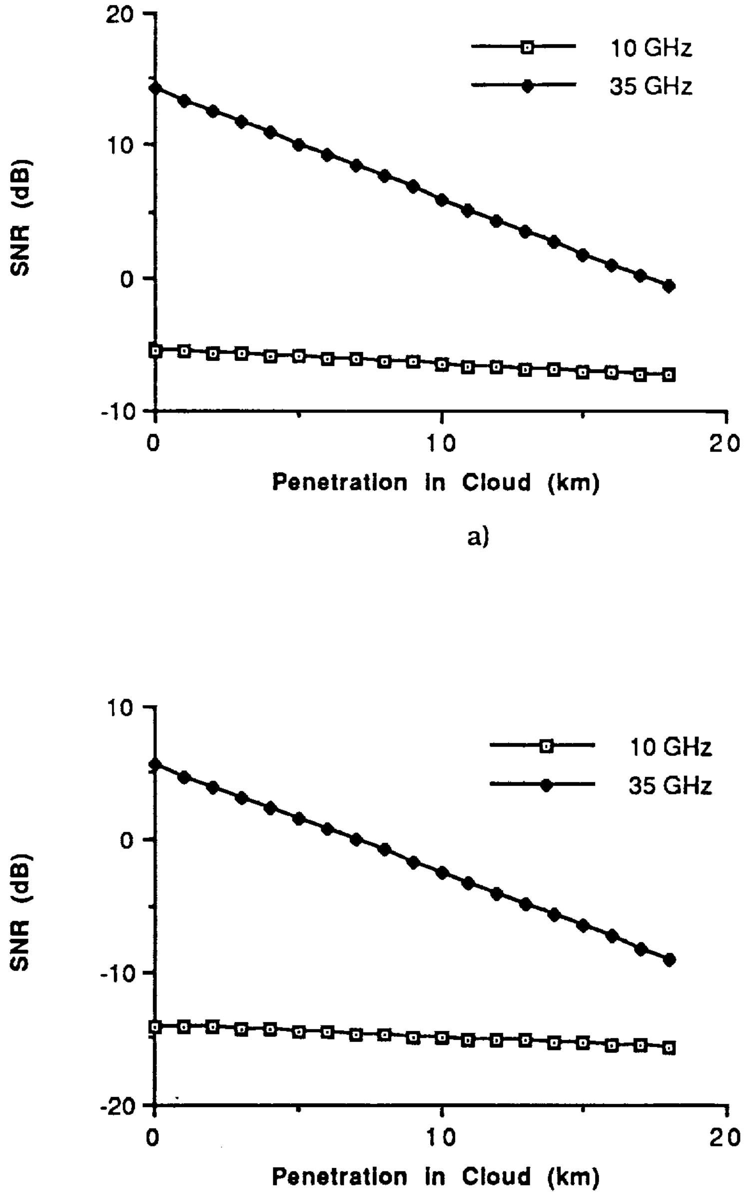

a)

b)

Figure 2.10. Signal to noise ratio of radar echo as a function of cloud penetration (water content of cloud = 0.5 gm^{-3}); a) orbit height = 300 km; b) orbit height = 830 km.

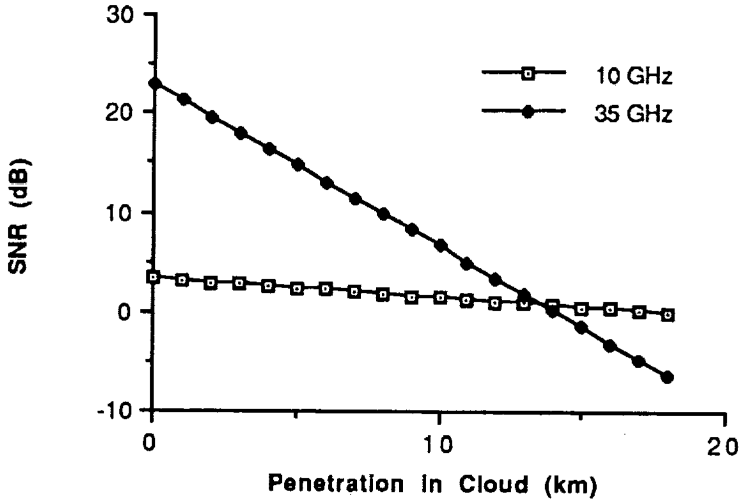

a)

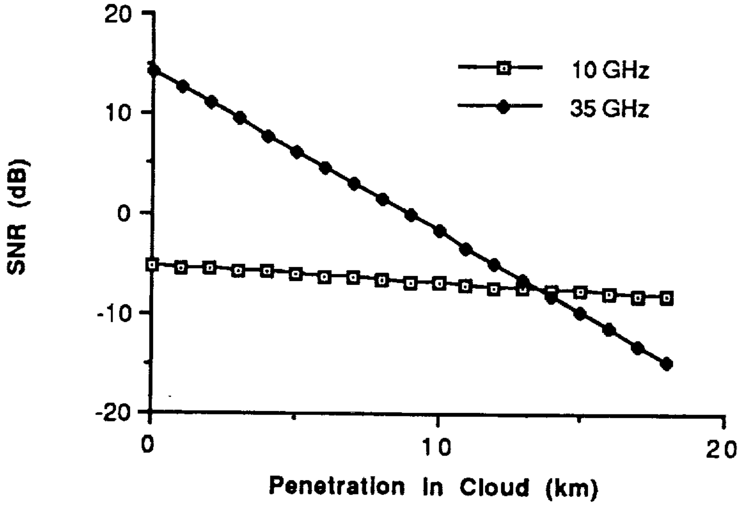

b)

Figure 2.11. Signal to noise ratio of radar echo as a function of cloud penetration (water content of cloud = 1.0 gm^{-3}); a) orbit height = 300 km; b) orbit height = 830 km.

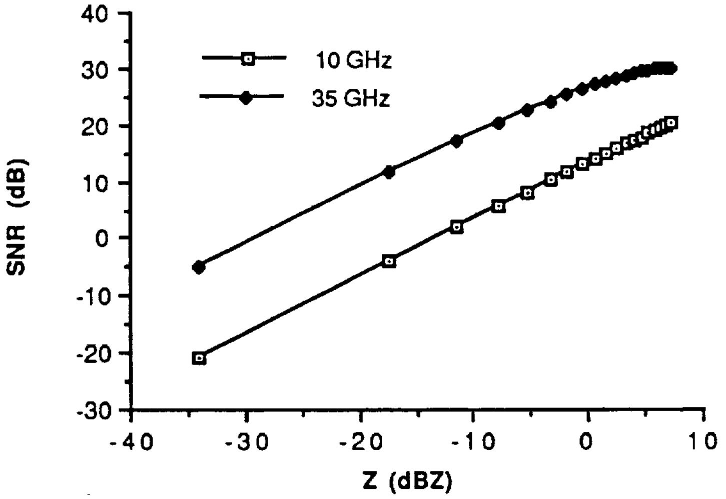

Figure 2.12. Signal to noise ratio of radar echo as a function of reflectivity factor Z ($mm^6\ m^{-3}$). The return signal is from 1 km depth from the cloud top.

Finally, Figure 2.12 shows the simulated signal-to-noise ratio (SNR) versus increments of the Z factor. Because the ice cloud is difficult to model, we can derive some qualitative idea from Figure 2.12 about the signal to noise ratio from ice clouds. For example, although the $|K_i|$ is about 0.2, 4.5 times smaller than $|K_w|$, Z for cirrus (ice) clouds at 35 GHz is 5 to 20 $mm^6\ m^{-3}$, and the signal-to-noise ratio is above 20 dB based on Figure 2.12.

2.3.2 CONCLUSION AND FUTURE WORK

The results presented in this chapter demonstrate that, from a SNR point of view, the 35 GHz Doppler radar can provide high enough SNR's of radar echoes from clouds for measuring mean Doppler frequency. Although the computer simulations were based on water cloud models, the results may also be applicable to ice clouds as discussed in the previous section. However, many other factors were not considered in the computer simulations and therefore not discussed in this chapter. For example, we did not consider the cases that the cloud dimensions are smaller than the antenna beamwidth, or the thickness of clouds are narrower than the vertical resolution of the radar. In these cases, the signal-to-noise ratios of radar echoes would be smaller than those simulated in this chapter. Moreover, some of the cloud models used in the computer simulations may be impractical. These questions need to be addressed in future studies.

Chapter 3

Conceptual Design and Analysis of Performance

3.1 INTRODUCTION

A large volume of published literature concerns operations of Doppler radars for measuring wind speed, weather forecasting, detecting turbulence, etc. However, there was not conclusive evidence that Doppler radars were able to measure the wind fields in clouds from space. One major obstacle was that the radars lacked the power to overcome the weak backscatter from clouds. Although recently there has been research in the area of using VHF and UHF Doppler radars to measure wind speeds [39-42], these VHF and UHF systems could not be used in spaceborne applications because of the excessive size of the antenna and power requirements. To meet the requirements for vertical resolution and peak power, a spaceborne Doppler radar for wind measurement should use a high frequency, as discussed in Chapter 2.

The Radar Wind Sensor (RAWS) is a proposed space-borne Doppler radar to be used as a multi-purpose instrument for measuring global wind fields in cloud-covered areas as well as rainfall and surface winds on the oceans. The basic configuration, as shown in Figure 3.1, has two antenna beams at two fixed elevation angles ϕ_1 and ϕ_2, and the antenna scan patterns are conical. The transmitted pulses are frequency modulated with compressed pulse widths of about 1 μs. Each antenna beam transmits signals at two different frequencies: one frequency is at about 10 GHz (X band), and the other is approximately at 35 GHz (Ka band). The frequencies used on the two antenna beams may need to be slightly different to avoid interference between received signals. To concentrate on the topic of wind measurement from non-precipitating clouds, we will primarily discuss the system configuration and performance for 35 GHz. The 10-GHz system will be covered by others since it is primarily useful for measurements of wind in precipitation systems, ocean-surface wind, or rainfall rate. For the lower elevations in rain, a f requency like 10 GHz is required because of the high attenuation of the 35-GHz signal traveling through rain.

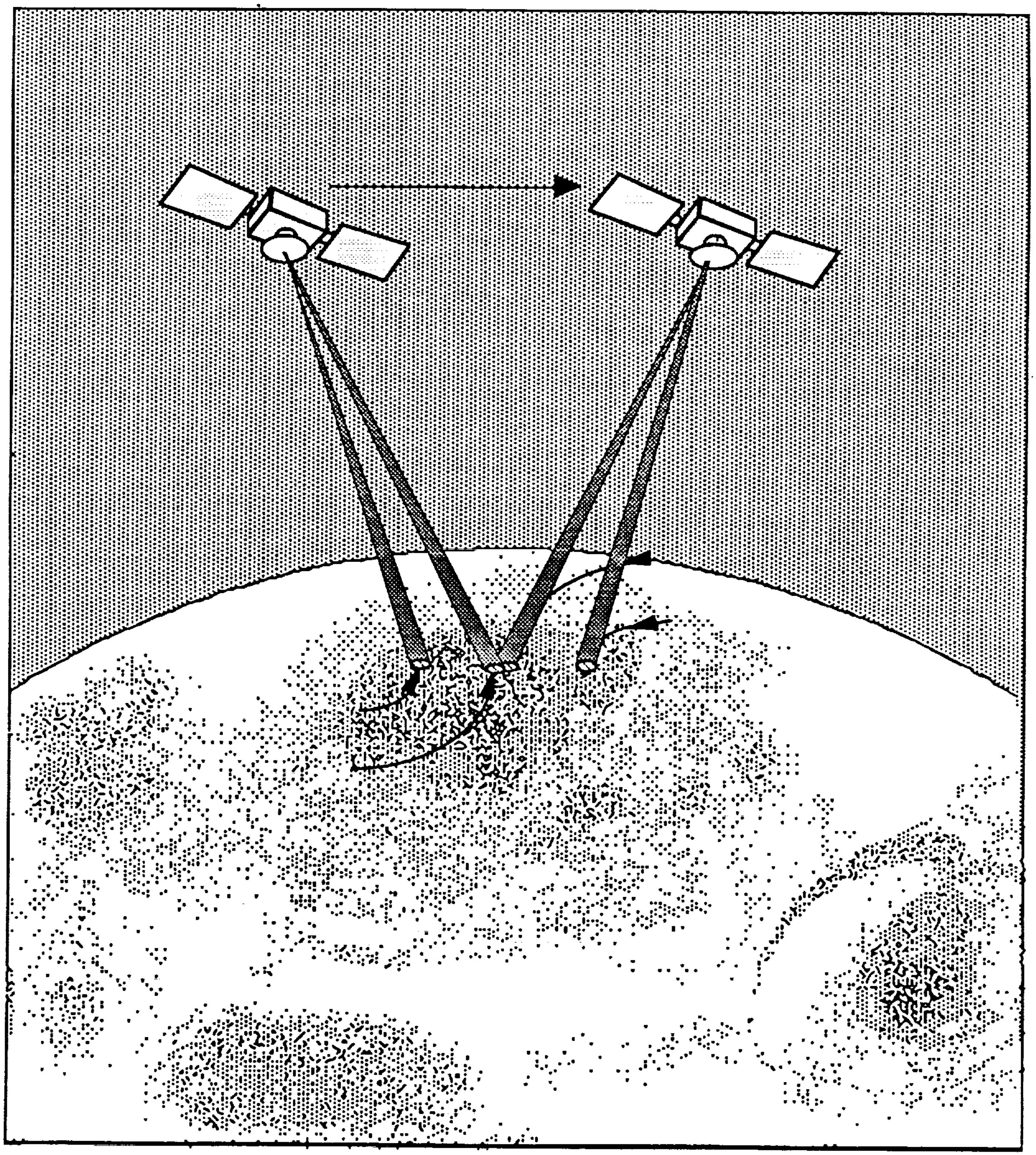

Figure 3.1. Basic concepts of two beam conical scan: the same area can be viewed forward and rearward by the antenna with different looking angles for wind vector component retrieval.

With circular scanning patterns, areas of hydrometeor activity can be illuminated multiple times by the antenna beams when the satellite traverses over these areas. Since wind vectors are three dimensional, one needs at least three measurements of the Doppler shifts from different angles to retrieve a wind vector. In clear air or light clouds, it is often assumed that the vertical components of wind vectors are uncorrelated with the horizontal components, and that the amplitudes of vertical components of wind vectors are very small in comparison to the horizontal components. Under such assumptions, the vertical components of wind fields can be estimated separately from the horizontal components, or even ignored in calculation of the horizontal components of wind vectors. Therefore, it is possible, by measuring the Doppler frequencies of water droplets in these regions from two different angles, that the horizontal wind vectors in the resolution volume can be retrieved. However, in heavy cloud regions and precipitation systems, the vertical wind vectors may not be ignored. In such cases, measurements with three linearly independent pointing angles are necessary to retrieve the wind vectors.

An assumption concerning the wind field was mentioned in Chapter one: the RAWS is used to measure the global and meso-α scale phenomena of the atmosphere. Thus, the measurements made within a 100 km by 100 km area can be averaged to achieve a more reliable measurement of the wind vector in this area.

In Chapter 2, we addressed the radar backscatter from different types of clouds. In this chapter, we will discuss the system parameters of RAWS and conduct an error analysis of the system performance. In addition, we will also discuss strategies of antenna scan patterns, and a method for compensating Doppler shifts caused by satellite motion.

3.2 BASIC CONFIGURATION OF THE SYSTEM

The basic parameters of a conceptual system for the radar wind sounder are listed in Table 3.1. Tradeoffs encountered in selecting the parameters such as antenna elevation pointing angle, scan period, and scan modes are discussed in detail below. Two orbit heights were selected for the conceptual design of the radar wind sounder. One is at 300 km for space-shuttle orbit, and the other is at 830 km for near-polar orbit. These orbit selections were referred to in [9]. In addition, some major obstacles, such as clutter rejection and limit on vertical resolution, are identified in the following discussion.

Table 3.1 Basic Parameters for the Radar Wind Sounder

PARAMETER	10 GHz	35 GHz
Altitude of Satellite	300 km or 830 km	
Target Volume Used in Output (from many individual measurements)	100 km × 100km × 20 km	
Nadir Angle	30° and 35°	
PRF	3500 Hz	
Pulse Width (Compressed)	1 μs	
Time-Bandwidth Product	20	
Antenna Size (Parabolic)	8m	
Antenna Gain	57 dB	68 dB
Horizontal Beamwidth	0.00427 rad	0.00122 rad
Vertical Beamwidth	0.00427 rad	0.00122 rad
Scan Period	10 s	10 s
Vertical Resolution	2 km	1 km
Footprint at 30° (300 km)	1.5 x 1.7 km	0.5 x 0.4 km
Footprint at 30° (830 km)	2 x 5.1 km	1.5 x 1.2 km
Doppler Bandwidth due to Satellite Motion	1900 Hz	
Peak Power	3000 W	
Average Power	210 W	
Receiver Noise Figure	4 dB	
Transmitter Loss	1.5 dB	
Receiver Loss	1.5 dB	
Spacecraft Velocity	7.5 $\mathrm{kms^{-1}}$	

3.2.1 SYSTEM PARAMETERS

OPERATING FREQUENCY

The operating frequencies of RAWS were chosen to be at 10 GHz and 35.5 GHz. However, from the computer simulation study in Chapter 2, we concluded that operating frequencies around 10 GHz may be more appropriate for measuring winds in precipitation, surface winds over the ocean, and rainfall rate. To measure winds from clouds, frequencies around 35 GHz or higher are needed with current technology. By observing the transmission windows in the microwave region presented in Figure 3.2, for frequencies above 20 GHz, windows at frequencies 35.5 GHz, 90 GHz, or 135 GHz are all applicable for measuring wind fields in clouds. Higher frequencies can increase the SNR of radar echoes from thin clouds and reduce the antenna size, but they also endure more extinction, and may not be able to penetrate deep enough through heavy clouds. In this dissertation we will only discuss the case of 35 GHz. The feasibility of using higher frequencies to measure wind fields from space may need further investigation.

ANTENNA GAIN, SIZE, AND BEAM WIDTH

To provide the high gain level and narrow vertical beamwidth required for good vertical resolution, a large antenna is desired. With the technology currently available, the size of an antenna can be made as large as 1000 wavelengths. We chose to use an 8 m diameter parabolic antenna in this conceptual design. It is possible to use this antenna for both 35 GHz and 10 GHz frequencies. For a uniformly illuminated parabolic antenna, the gains of the antenna for both of these frequencies can be calculated with the following formula:

$$\begin{aligned} G_0 &= D_0\,\varepsilon_{ap}\,\varepsilon_t \\ &= \left(\frac{d\pi}{\lambda}\right)^2 \varepsilon_{ap}\,\varepsilon_t \qquad (3.1) \end{aligned}$$

where G_0 is the maximum value of gain, D_0 is the directivity, d is the diameter of the dish of the reflector, ε_{ap} is the aperture efficiency of the parabolic antenna, and ε_t is the antenna efficiency. Typical values for these parameters are ε_{ap} = 60% - 80% andε_t=95% [43]. If we choose ε_{ap}=70%, ε_t =95%, and substitute these values in to (3.1), it follows the antenna gains of G=68 dB at f=35.5 GHz and G = 57 dB at f=10 GHz.

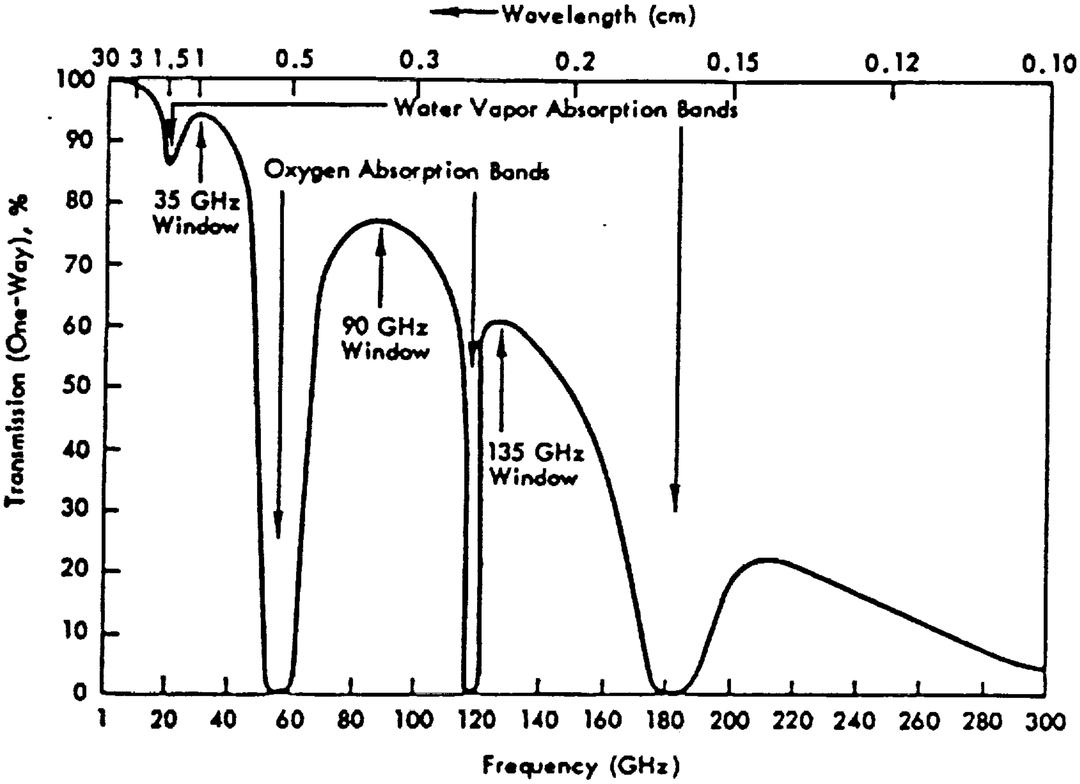

Figure 3.2. Percentage transmission through the earth's atmosphere, along the vertical direction, under clear sky conditions. (From F. T. Ulaby, R. K. Moore, and A. K. Fung, 1981 [25])

The beam widths of the antennam can be calculated using the experimental formula from [43]:

$$G_0 = \frac{30000}{\theta_{1d}\,\theta_{2d}} \qquad (3.2)$$

where θ_{1d} and θ_{2d} are horizontal and vertical beam widths. For a parabolic antenna, from (3.2), $\theta_{1d}=\theta_{2d}=0.07°=1.22$ m rad at 35.5 GHz and $\theta_{1d}=\theta_{2d}=0.244°=4.27$ m rad at 10 GHz.

ANTENNA POINTING ANGLE

There are tradeoffs in selecting the antenna pointing angles, the vertical resolution and the swath width. The vertical resolution imposes a limit on the use of large antenna pointing angles; however, a large pointing angle is desired for achieving large swath width and reducing measurement errors for horizontal components of wind vectors. Figure 3.3 shows the limitation on the antenna pointing angle imposed by the vertical resolution. The vertical resolution not only depends on the pulse length, but also on the antenna pointing angle and beamwidth. Assume that R is the slant range, ϕ_i the elevation angle of the antenna,

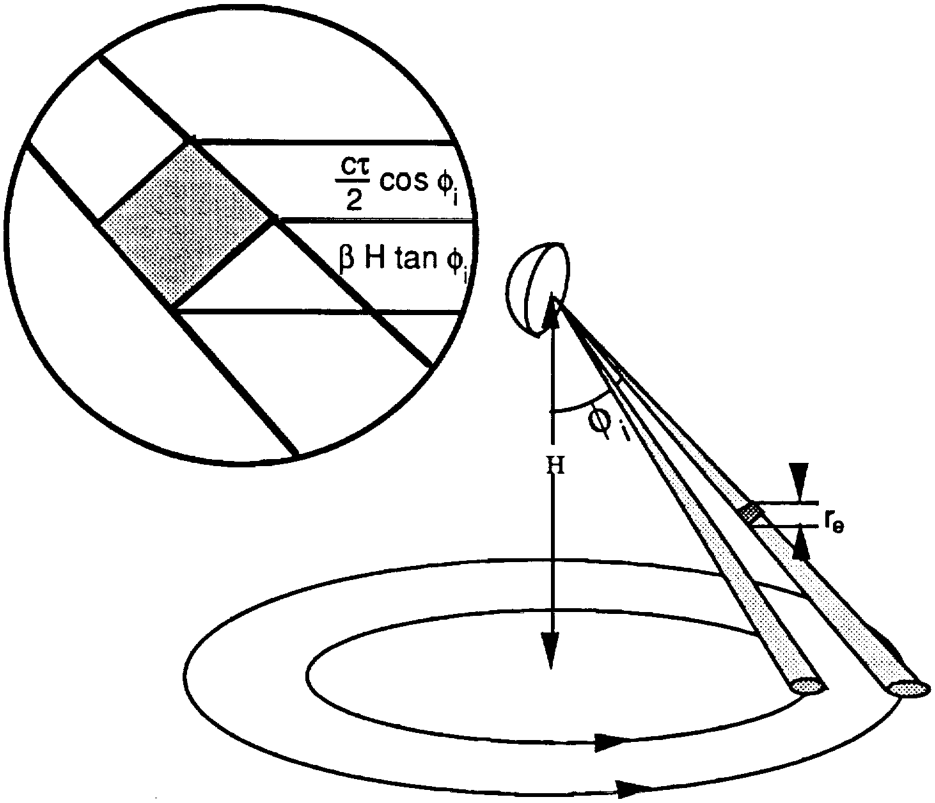

Figure 3.3. Tradeoff between the antenna pointing angle, antenna beamwidths and the vertical resolution, where ϕ is antenna pointing angle, r_e is the edge-to-edge vertical resolution, and H is the height of the antenna.

β the beam width, τ the pulse length (compressed, if chirp is applied), then r_e (the edge-to-edge vertical resolution) is equal to:

$$r_e = \beta R \sin \phi_i + \frac{c\tau}{2} \cos \phi_i \qquad i = 1,2 \tag{3.3}$$

Equation (3.3) shows that the vertical resolution is a sum of two terms. The first term is contributed by the antenna beamwidth, and the second term is contributed by the pulsewidth. For the assumed parameters :

R = 830 km /$\cos\phi_1$
r_e = 1 km
β = 1.22 mrad (35 GHz)
ϕ_1 = 35°

the pulsewidth is limited by the following inequality:

$$\tau \leq 2 \frac{r_e - \beta R \sin \phi_i}{c \cos \phi_i} \tag{3.4}$$

From (3.4), the pulse length τ is limited to less than 1.65 µs. Using the same parameters as above except an orbit height of 300 km (space-shuttle orbit), the pulse length is limited to less than 4.08 µs. However, for f=10 GHz and β=4.27 mrad, the vertical resolution cannot be less than 1 km in 830-km orbit and the pulse length is limited to less than 0.56 µs (to satisfy 1 km vertical resolution in 300 km orbit). The primary limit to resolution is the beam width. Hence, a taller antenna (>8 m) would allow improved vertical resolution.

Another definition of the vertical resolution is called the effective vertical resolution. It is defined as the -6 dB 3-dimensional contour of the radar illumination [44]. With this definition, Kozu (1989) pointed out that the effective vertical resolution for spaceborne radar can be well approximated by [45]:

$$r_{eff} \approx \sqrt{(\beta h \tan \phi_i)^2 + (\frac{c\tau}{2} \cos \phi_i)^2} \tag{3.5}$$

Essentially, equation (3.5) imposes the same constraint on the antenna pointing angle as does equation (3.3). To achieve a small vertical resolution, the pointing angle of the antenna and the beam width also need to be small. With orbit heights of 300 km and 830 km, the swath widths are calculated in the following table

Table 3.2 Swath Widths for Different Orbits and Antenna Pointing Angles

Orbit Height	swath width ($\phi = 35°$)	swath width ($\phi = 30°$)
300 km	420 km	346 km
830 km	1162 km	923 km

Because of the limits on the antenna pointing angle and the vertical resolution, the swath widths of the radar system are smaller than those of LAWS [9].

CLUTTER FROM ANTENNA SIDE LOBES

Clutter is generally defined as any unwanted radar echo. In the context of this dissertation, it mainly consists of the echoes from land and sea. The clutter from the main antenna lobe may not be a problem, since it can be separated from the received signal by range gating. However, the clutter from the antenna sidelobes can be a severe problem to the system. This is due to the fact that the backscatter coefficients of sea and land clutter are much larger than the volume-scatter coefficients of clouds [46-47]. Even when the gains of the antenna side lobes are 40 dB below the main lobe, the power of the clutter may still be higher than that of the signal returned. To solve this problem, we make some suggestions below:

- Using a narrow pulse width and large antenna pointing angle, so that the energy of the clutter can be reduced as a result of reduced cross-section of clutter.
- Designing the antenna such that sidelobes near vertical are very small.

Although a detailed study of clutter rejection is an important issue in the RAWS study, it is beyond the scope of this dissertation.

PRF SELECTION

With t_p the pulse length, r_r the range resolution, and c the speed of light, the range resolution is $r_r = ct_p/2$. To obtain a fine range resolution, it is necessary to have a short pulse length. On the other hand, the frequency resolution requires the that minimum time of measurement be approximately equal to the inverse of the bandwidth of the Doppler filter.

A typical radar pulse length is on the order of microseconds, and the target (wind) speed is on the order of tens of meters per second. To achieve a windspeed resolution of 1 ms^{-1}, the required measurement-time is about 15 milliseconds at 3 cm wavelength (10 GHz), and 4.3 milliseconds at 0.857 cm wavelength (35 GHz). Because of the required range resolution of 1 km, such long pulses cannot be used in the design of RAWS. Therefore, unlike a laser radar (lidar) system which may use a single pulse to measure the Doppler shift, a microwave radar wind sounder must use a train of pulses to measure the mean Doppler frequency and at the same time meet the requirements of range and frequency resolutions.

To avoid range ambiguity for evenly spaced transmitted pulses, the pulse repetition time (PRT) is bounded by the following inequality:

$$PRT \geq 2\,T_{trans} + T_{echo} + T_{guard} \tag{3.6}$$

where T_{trans} is the pulse length of the transmitted pulse (it is expanded pulse width when the chirp technique is applied); T_{echo} is the round trip delay of the electromagnetic wave propagating through a 20 km thick cloud; and T_{guard} is the time required to compensate for variations of the Earth's surface. For a uniformly spaced pulse train, with $T_{trans} = 20\ \mu s$, $T_{echo} = 163\ \mu s$ at 30 deg. antenna pointing angle, and $T_{guard} = 10\mu s$, equation (3.6) leads to the following inequalities:

$$PRT \geq 213\ \mu s$$

$$PRF \leq 4700\ Hz \tag{3.7}$$

For a train of pulse-pair transmission as shown in Figure 3.4, and discussed later in chapter 5, the PRT is bounded by

$$\mathrm{PRT} \geq 2T_2 + 2T_{trans} + T_{echo} + T_{guard} \tag{3.8}$$

Assuming that the pulse width is 20 μs, T_1=PRT, T_2 = 35 μs, and T_{guard} = 10 μs, it follows that

$$\mathrm{PRT} \geq 283\ \mu\mathrm{s}$$

$$\mathrm{PRF} \leq 3523\ \mathrm{Hz}$$

For a quadratic receiver, taking PRF as the sample frequency, the Nyquist frequency is equal to half of the PRF. Thus, to measure 60 ms^{-1} radial wind speeds, the minimum PRFs required to satisfy the Nyquist criterion are equal to

$$\frac{4v}{\lambda} = \begin{cases} 8000\ \mathrm{Hz} & \text{at } f=10\ \mathrm{GHz} \\ 28400\ \mathrm{Hz} & \text{at } f=35.5\ \mathrm{GHz} \end{cases} \tag{3.9}$$

From (3.9), we can see that there is a very severe frequency-ambiguity problem at 35 GHz; the maximum Doppler shift can be as large as 8 times the Nyquist frequency. Later in Chapter 5, we discuss the algorithms for reducing frequency ambiguity problems.

3.2.2 ANTENNA SCAN SCHEMES

Selection of the antenna scan mode was one of the major problems in the design of RAWS that we had to investigate. During the measurements of Doppler frequencies, both the satellite and the antenna beams are in motion, and this may cause changes in the beam position and antenna pointing angles. Such changes may introduce errors in estimation of the mean frequency as well as decorrelation to the returned signals. The changes in antenna pointing angle and beam position can be reduced or minimized by choosing an optimal antenna scan mode. In this

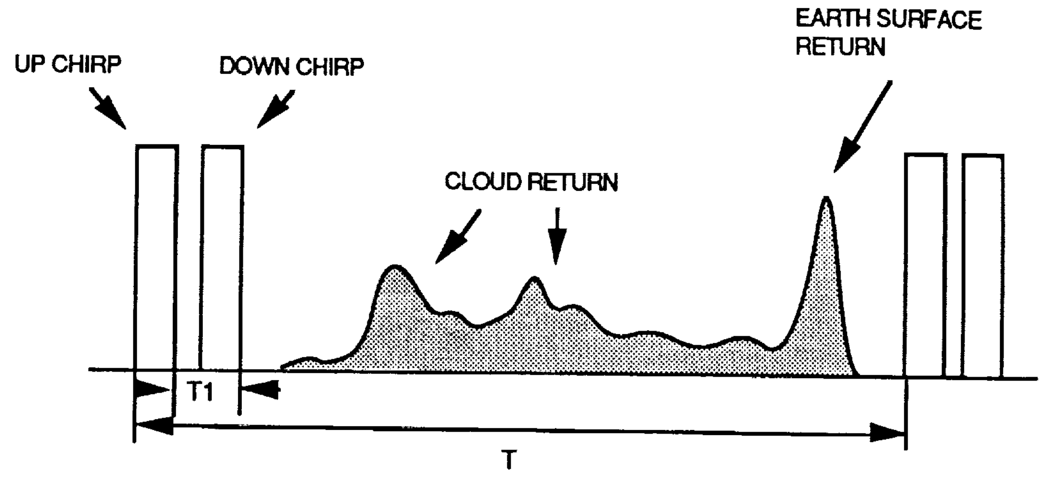

Figure 3.4. Illustration of pulse-pair transmission scheme, and limit on the PRT. T is the PRT, T_1 is inter-pulse spacing.

section, three scanning modes are examined: the first is uniform scan; the second is discrete scan; and the third is a combination of the uniform and the discrete scans. These three scan schemes require different levels of complexity in hardware and also introduce various amount of errors into frequency measurements.

3.2.2.1 UNIFORM SCAN

In a uniform scanning scheme, the antenna rotates with a constant angular speed achieved with a scanning motor or by satellite rotation. However, there is a severe problem with this simple scanning strategy caused by satellite motion and antenna beam rotation. This scan mode is illustrated in Fig 3.5a. For example, assuming the PRF = 3500 Hz and that each measurement contains 256 samples, it would take 256/3500=73.1 ms for each measurement. However, if the uniform scanning period T_s=10 s, during one measurement interval the outer beam would travel 9.6 km and the inner beam 7.96 km with a 300 km orbit. These values are more than 10 times as large as one footprint of the antenna beams at f=35 GHz. Such a large displacement in antenna beam can cause a serious decorrelation in the returned signals. In addition, the antenna pointing angle changes nearly 2.6° during each measurement. Such a large change in antenna pointing angle is bound to cause a large error in calculations of the wind vectors. The only way to reduce the

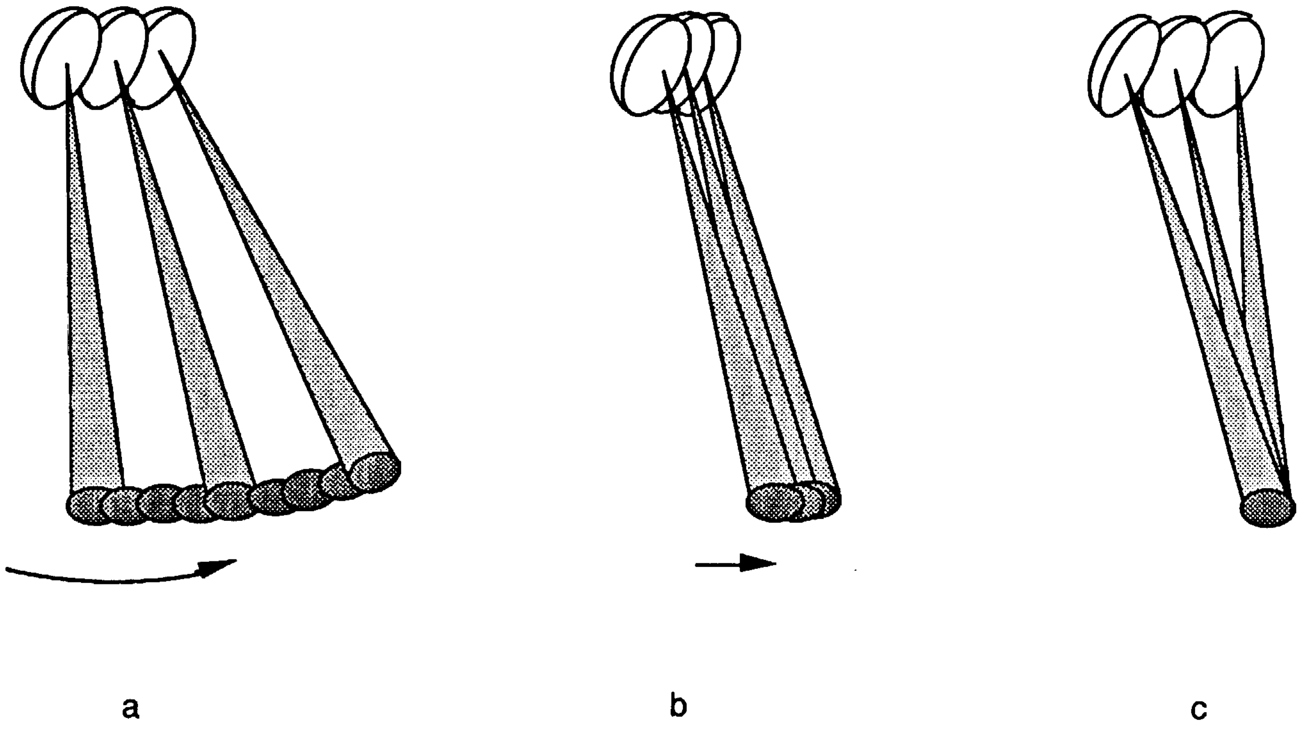

Figure 3.5. Antenna scan pattern; a) uniform scanning; b) discrete scanning; c) a combination of the uniform and the discrete scanning.

changes in pointing angle and displacement in antenna beam is to lengthen the scan period. However, because of the required horizontal resolution of measured wind field, the density of measurements is limited to at least once per 100 km by 100 km. This imposes a limit on the scan period being less than 27 s.

3.2.2.2 DISCRETE SCAN

The second mode, shown in Fig 3.5b, is a discrete scan which assures that the pointing angle does not change during each measurement. The only decorrelation introduced is due to the satellite motion; the beam travels 0.54 km during a measurement of 256 samples. However, there is no antenna pointing error during the measurement. Strictly speaking, the discrete scheme needs to be semi-discrete, as the motion of the antenna beam from one position to the next cannot be at a very high speed. Otherwise, the phase lock loop (PLL) used to track the Doppler shift of clutter caused by satellite motion may lose track of the Doppler frequency from the clutter (see section 3.2.3). Considering the size of the antenna the discrete scan is difficult to implement mechanically. Electronic scan for such a large antenna may also be too costly and complicated to be achievable. However, use of a set of phased arrays cannot be ruled out.

3.2.2.3 COMBINATION OF UNIFORM AND DISCRETE SCAN

The third scheme is to focus the beam to the center of the resolution volume while a measurement is being made. This strategy can be implemented by a combination of both electronic and mechanical methods. For example, the reflector of the antenna can be controlled by a motor, and the antenna feed can be an electronically scanned phased array. During each measurement, the feed moves the beam back and forth to focus on the center of the resolution volume, while the reflector rotates at a uniform speed. This scheme, shown in Fig 3.5c, can greatly reduce the decorrelation problem which was inherent in the uniform scan-scheme. However, the change in pointing angle, during each measurement, can introduce estimation errors. The angle change can be calculated by the following expression:

$$\Delta\phi \simeq \frac{v\,T_m}{R} \tag{3.10}$$

where $\Delta\phi$ is the angle difference between the initial and final pointing angle in a measurement of the mean frequency, T_m is the measurement time, R is the slant range, and v is the satellite speed. Assuming that the measurement time is T_m=73 ms (256 pulses), with satellite speed v = 7500 ms^{-1}, then the angle difference is equal to:

$$\Delta\phi \simeq \begin{cases} 2 \text{ mrad} & \text{for space shuttle orbit} \\ 0.6 \text{ mrad} & \text{for near polar orbit} \end{cases}$$

Such a small change in antenna pointing angles may not introduce any significant error in retrieving wind vectors as we will see later in section 3.3.3.

In comparison of the three scan modes, we may conclude that the uniform scan is not a satisfactory scheme; the discrete mode may be too costly to implement; the combination of uniform and discrete scan is the optimal choice among the three.

3.2.2.4 SCAN TRAJECTORY

The coordinates of the two beam trajectories in a Cartesian system can be expressed as:

$$x = h \times \tan \phi_i \times \cos \omega t + vt$$

$$y = h \times \tan \phi_i \times \sin \omega t \qquad i = 1,2 \qquad (3.11)$$

where

ϕ_i = the antenna's elevation angle
ω = the angular speed of scan
v = the speed of satellite
h = the height of the satellite orbit.

Figure 3.6 presents the trajectories of the antenna beams at orbits of 300 km and 830 km.

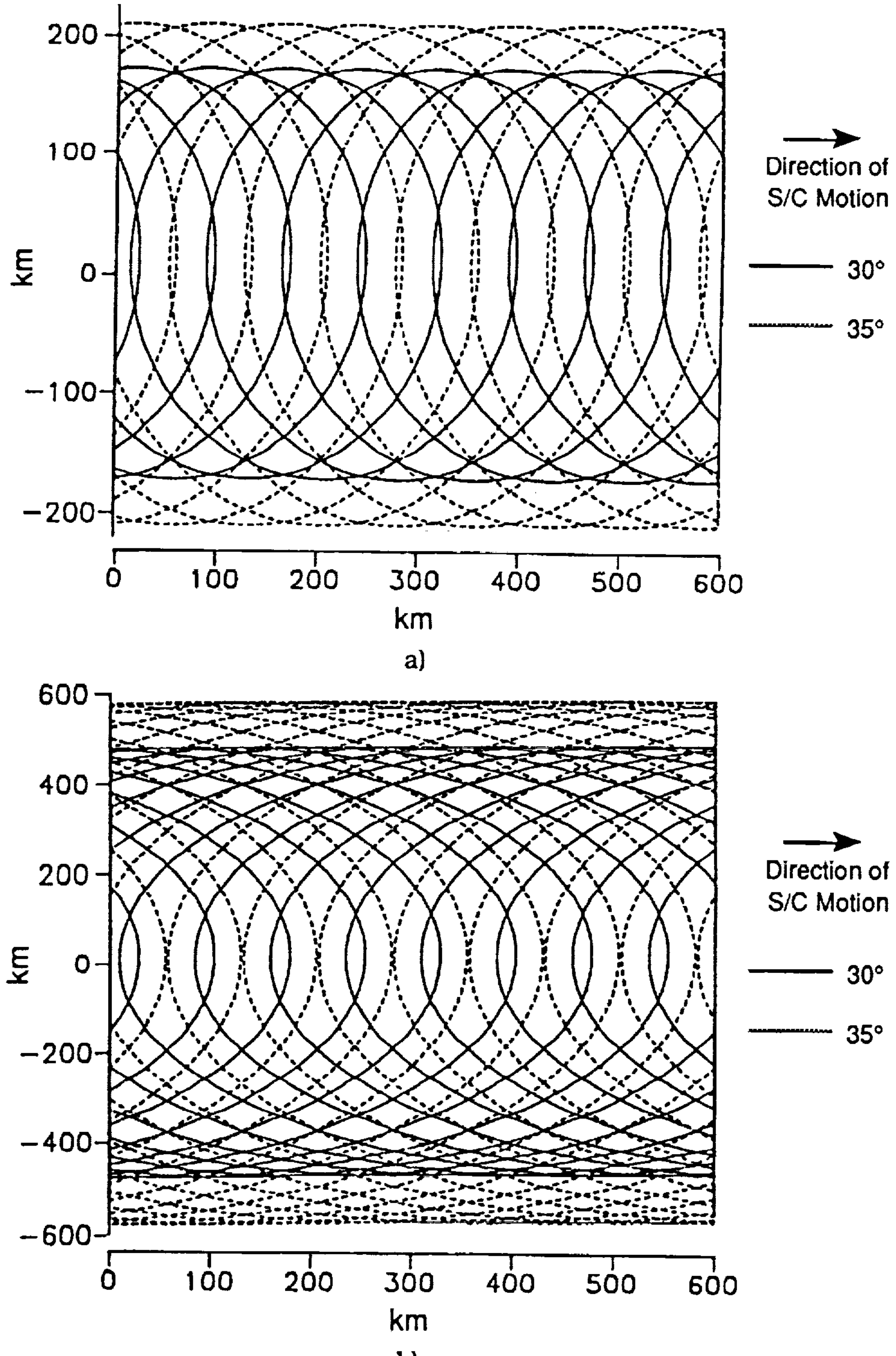

a)

b)

Figure 3.6. Antenna scan trajectories at 30 deg. and 35 deg. pointing angles with scan period = 10 s; a) at 300 km orbit; b) at 830 km orbit.

This figure shows that all four trajectories intersect only at very few points. It can be seen that if the measurements are made at the places where at least two trajectories intersect, the measurements would not be uniformly distributed. Namely the marginal area would get more measurements than the central region. The same problem has also been experienced in the research on LAWS. An adaptive laser shot pattern was suggested to cope with this problem. This adaptive shot pattern is designed to control slew rates of the scanner and schedule pulse suppression in regions of low information potential [23]. A similar method can be applied to RAWS. In fact, the RAWS has the advantage of two antenna beams which can lead to a more evenly distributed measurement pattern. However, we leave this topic for future study.

With the intention of simplifying the analysis of the error bounds of the estimation of wind speed in the next section, we will consider the measurements are being made only at places where two beam trajectories intersect. This may not be necessary in practice, since we have assumed that the wind field being measured is much larger than the resolution volume. Thus, all of the measurements of Doppler frequencies in a 100 km by 100 km area could be freely combined to derive the wind vectors in this area. However, measurements of Doppler frequency with pointing vectors close together may give more accurate estimates.

To further simplify the error analysis in the following section, assume that we only want to make measurements at the intersections of the trajectories of the antenna beams with the same elevation angle. We can pre-calculate these points with the following equation

$$(2n+1)\pi - 2\theta = \omega t \qquad n = 0,1,2,\ldots$$

$$2\,h \tan\phi_i \cos\theta = vt$$

or

$$\frac{2\omega h \tan\phi_i}{v} \cos\theta + 2\theta - (2n+1)\pi = 0 \qquad n = 0,1,2,\ldots. \tag{3.12}$$

where

v = satellite speed
h = orbit height
ϕ_i = elevation angle
θ = horizontal angle

With T_S=10 s, ϕ_1=30° and ϕ_2= 35°, the above equation can be solved numerically. Table 3.3 lists the positive angles at which two trajectories intersect. Since the trajectories of beams are symmetrical about the ground track of the satellite, the negative angles can be obtained by adding minus signs to the values listed in Table 3.3.

Table 3.3 Roots of equation (3.12)

θ in rad (ϕ = 30°)	θ in rad (ϕ = 35°)
0.307	0.2567
0.79	0.702
1.084	0.964
1.3357	1.182
	1.38

3.2.3 TRACKING THE DOPPLER SHIFT CAUSED BY SATELLITE MOTION

In the context of calculating the error bound for wind speed we made the assumption that the Doppler shift due to the satellite motion could be accurately compensated. In the following, we will discuss a strategy used to compensate this Doppler shift. As shown in Figure 3.7, which illustrates a simplified block diagram of the radar system, two stages are used in compensating the Doppler shift by tracking the mean Doppler frequency of clutter return. In the first stage, the compensation is accomplished through an inertial navigation system sending antenna pointing angle information to a control processor. The control processor tunes a voltage-controlled oscillator (VCO) to counterbalance the Doppler shift caused by satellite motion according to the information given. This is an open-loop system; the compensation error is dependent on the accuracy of the information provided by the inertial navigation system. The second stage compensation is carried out by a closed loop tracking system. This tracking system can be implemented by a digital phase lock loop, an analog phase-lock loop, or a combination of a Kalman filter and a phase lock loop. In the following, we assume that the second stage compensation is performed by a second-order analog phase lock loop.

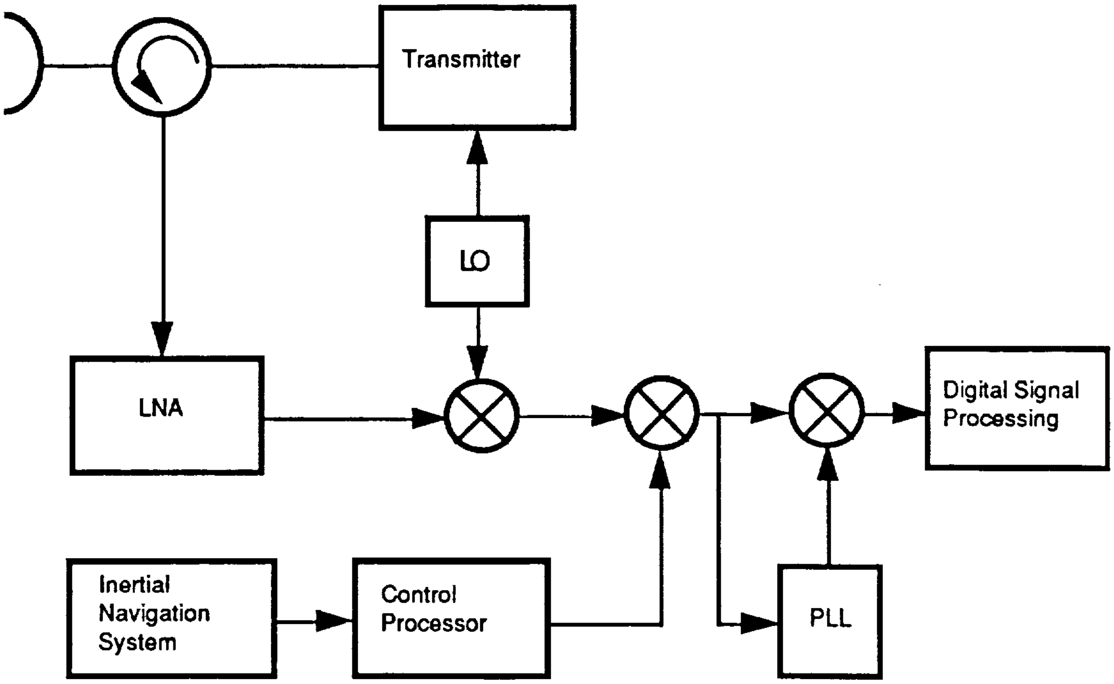

Figure 3.7. Functional Block Diagram of Radar Wind Sounder. It shows the two stage tracking of the Doppler shift caused by satellite motion.

Denote the velocity of the satellite, **u**, the pointing vectors **r** and the Doppler shift f_D. Asume the satellite is heading in x direction. Then **u**, **r** and f_D can be expressed as:

$$\mathbf{u} = v\,\mathbf{x}$$

$$\mathbf{r} = \sin\theta\cos\phi\,\mathbf{x} + \sin\theta\sin\phi\,\mathbf{y} + \cos\theta\,\mathbf{z}$$

and

$$f_D = \frac{2\mathbf{u}}{\lambda}\cdot\mathbf{r} \tag{3.13}$$

Then, the bound of the remaining Doppler frequency after the first-stage compensation can be expressed as

$$\Delta f_D \approx \frac{2v}{\lambda}[\cos\theta\cos\phi\,\Delta\theta + \sin\theta\sin\phi\,\Delta\phi]$$

$$< \frac{2v}{\lambda}\cos(\theta - \phi)\max(\Delta\theta, \Delta\phi) \qquad (3.14)$$

where $\Delta\theta$ and $\Delta\phi$ are remaining antenna pointing errors after the compensation by the first-stage tracking. If the pointing errors can be reduced to less than 1 mr by the inertial navigation system of the satellite (according to the LAWS report [9], the pointing error is on the order of tens of microradians), the bound of Δf_D is about 2 kHz at f=35.5 GHz.

In the following, a computer simulation of the error of the dynamic tracking carried out by a second-order phase-lock loop is completed. Investigation of more advanced tracking methods is left to further studies.

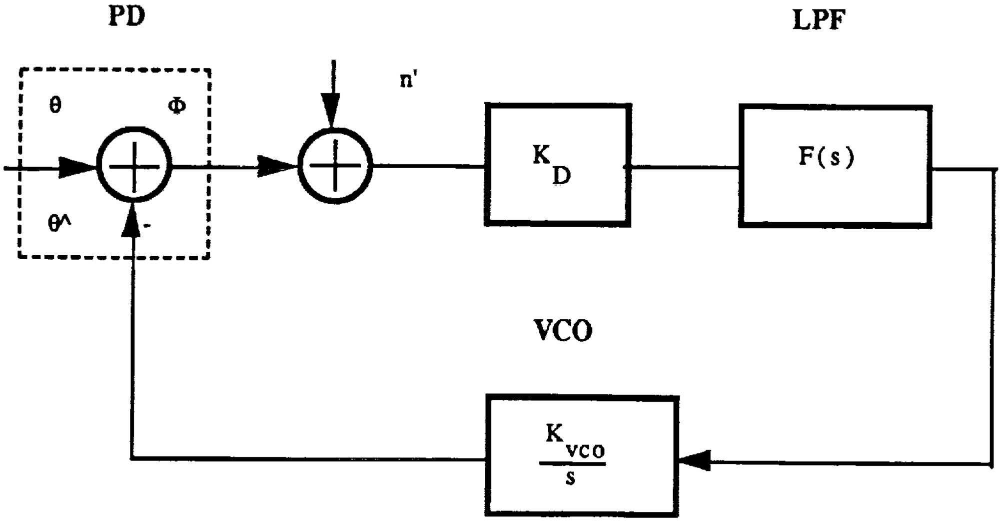

Figure 3.8. Equivalent linearized baseband model of a PLL.

3.2.3.1 FREQUENCY TRACKING BY A PHASE LOCK LOOP

As shown in Figure 3.8, a phase lock loop (PLL) consists of a phase detector (PD), a low pass filter, and a voltage-controlled oscillator(VCO). The low-pass filter can be first, second, or third order, which is also referred to as the order for the PLL. The input signal to the PLL is usually modeled as the sum of the signal s(t) and the noise n(t)

$$y(t) = s(t) + n(t)$$

with

$$s(t) = A(t) \sin(\omega_0 t + \phi(t))$$

$$n(t) = n_c \cos \omega_0 t + n_s \sin \omega_0 t$$

where both n_c and n_s are narrow-band Gaussian noise processes. The phase detector can be modeled by an ideal multiplier whose output equals

$$\varepsilon(t) = K_D \left[\sin(\Phi(t) + n'(t))\right]$$

with

$K_D = K_{vco} A$

K_{vco} = amplitude of the VCO signal

θ = phase of the input signal

$\hat{\theta}$ = phase of VCO

$\Phi = \theta - \hat{\theta}$ = phase error

and n'(t) is also a narrow band Gaussian noise which has the following relation with the input noise n(t)

$$n'(t) = \frac{n_c(t)}{A} \cos\hat{\theta} + \frac{n_s(t)}{A} \sin\hat{\theta}$$

LINEAR APPROACH

When the phase error Φ is very small, the PLL can be approximated by a linear system with the following transfer function

$$\frac{\hat{\theta}(s)}{\theta(s)} = H(s) = \frac{K_{vco} K_D \frac{F(s)}{s}}{1 + K_{vco} K_D \frac{F(s)}{s}} \tag{3.15}$$

For a second order PLL with perfect integrators, the error transfer function can be written as [48-49]:

$$\frac{\theta_e(s)}{\theta_i(s)} = \frac{s^2}{s^2 + 2\xi\omega_n s + \omega_n^2} \tag{3.16}$$

with ξ the loop damping factor, ω_n the natural frequency. The input noise power to a phase lock loop is equal to

$$P_N = \frac{1}{2\pi} \int_{-\infty}^{+\infty} S_{nn}(\omega)\, d\omega = N_0 B_{IF} \tag{3.17}$$

where $S_{nn}(\omega)$ is power spectral density of input signal, B_{IF} is IF bandwidth. The bandwidth of the phase-lock loop is generally much smaller than the IF bandwidth and is defined as:

$$B_L = \frac{1}{2\pi} \int_{-\infty}^{+\infty} |H_{nn}(\omega)|^2 d\omega \quad \text{Hz} \tag{3.18}$$

The SNR in the loop is defined as

$$\rho=\frac{1}{\sigma_{\hat{\theta}}^{2}}=\frac{A^{2}}{N_{0}B_{L}}=\mathrm{SNR}_{i}\frac{B_{IF}}{B_{L}} \tag{3.19}$$

where SNR_i is input SNR. For more detailed descriptions of these parameters in a phase-lock loop, one can refer to [48], [50], [51].

LOCK LIMIT, HOLD-IN RANGES

The hold-in range is defined as the input frequency range over which the loop can sustain a lock status. The hold-in range for a frequency offset of PLL is shown [48] as

$$\Delta\omega_{H}=\pm K_{vco}K_{D} \tag{3.20}$$

Similarly, the maximum permissible rate of change of input frequency is limited by

$$\Delta\omega'=\omega_{n}^{2} \tag{3.21}$$

These two parameters are important in computer simulations of the PLL since the input signal cannot have a frequency offset or a change of frequency rate larger than those set by (3.20-3.21). Otherwise, the loop would lose the tracking.

NON-LINEAR ANALYSIS

Linear analysis is valid when the input phase error is small and the loop SNR is high. However, to study the dynamic behavior of PLL's, we need to consider the non-linear properties of the PLL. As an analytical solution is difficult to achieve for a second or a higher order PLL, we resort to computer simulation for the tracking problem by the PLL. First, we need to develop a state variable equation for a second order PLL. An equivalent function block diagram of a second order PLL with perfect integrators is shown in Figure 3.9.

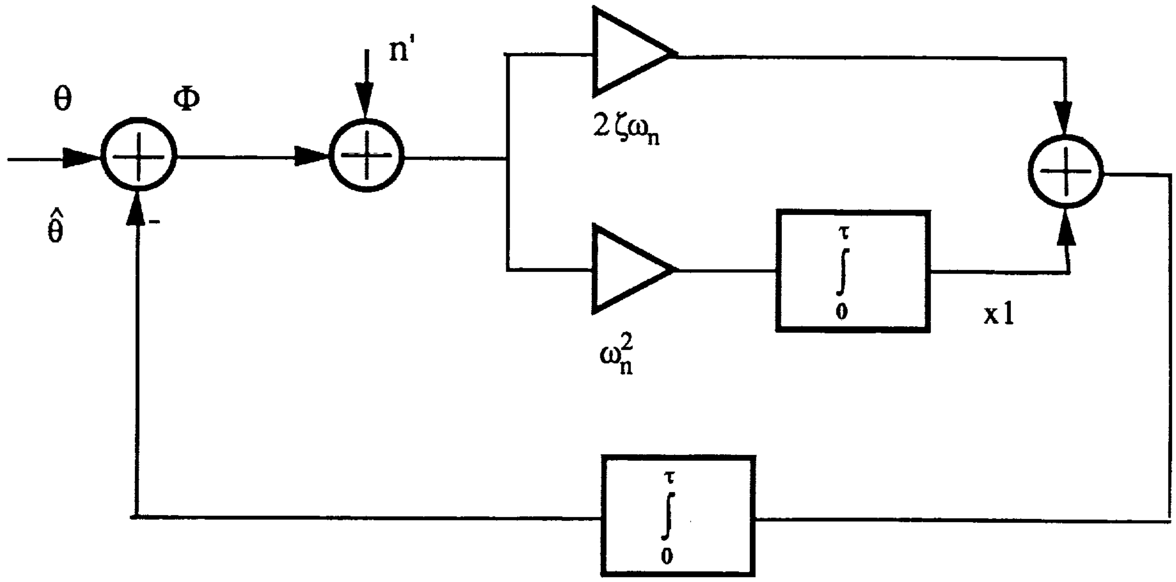

Figure 3.9. Equivalent block diagram of a second order PLL with perfect integrators.

The corresponding state variable equation is:

$$d\Phi / dt = -2\zeta\omega_n [\sin\Phi + n'] - x + d\theta/dt \qquad (3.22)$$

$$dx / dt = \omega_n^2 [\sin\Phi + n']$$

In the computer simulation of this stochastic system represented by (3.22), the following parameters are chosen:

$d\theta/dt = 2000\, u(t) \sin\omega_s t$, input signal to the PLL

where u(t) is a unit step function.

ω_s = angular speed of scan

$\zeta = 0.5$

$\omega_n = 100$

n' = a narrow band Gaussian random process, generated by an AR(1) filter.

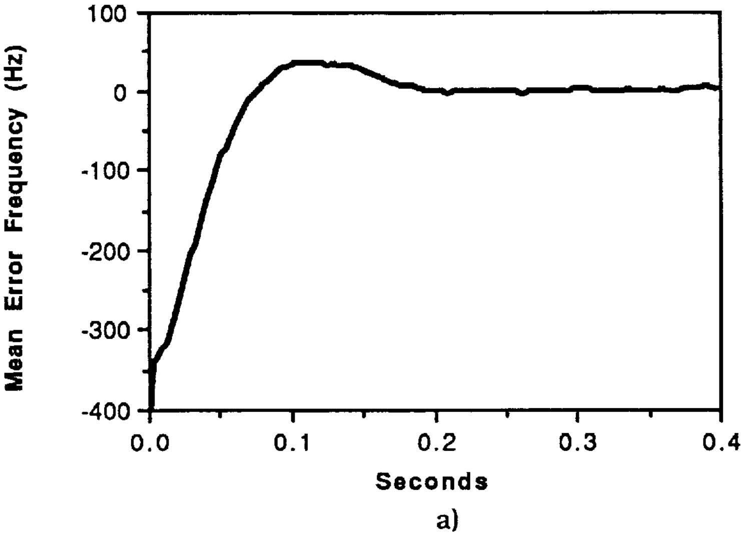

a)

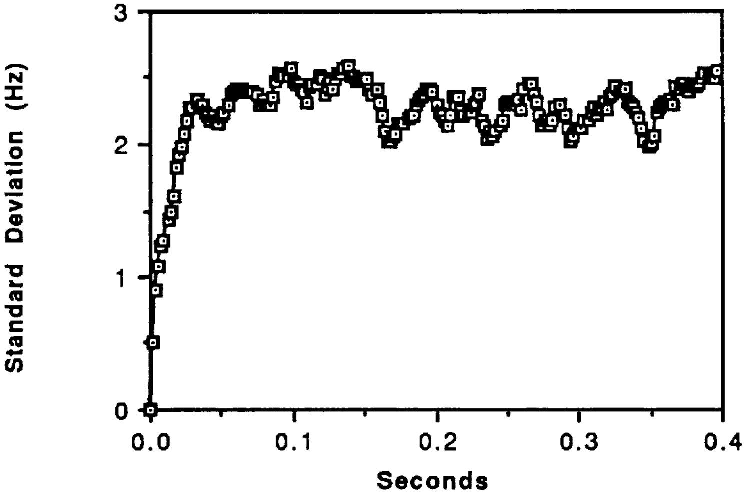

b)

Figure 3.10. Monte-Carlo simulation of tracking error by a second order PLL with perfect integrator; a) ensemble average; b) standard deviation of frequency error

A 4th-order Runge-Kutta method is used in the simulations. It was shown that using the Runge-Kutta method in computer simulation of a random system, the result is equivalent to the definition of Ito stochastic equation [52-54]. Figure 3.10 presents the Monte Carlo simulation. As expected the RMS error of tracking frequency depends on the SNR in the loop. When the SNR is high the RMS error in frequency tracking is very small.

3.3 MEASUREMENT ERRORS OF WIND SPEED DUE TO ANTENNA POINTING ERROR AND FREQUENCY MEASUREMENT ERROR

3.3.1 BASIC EQUATIONS

The Doppler frequencies observed by the radar can be represented as

$$f_{Di} = \frac{2(u_w - u_s - u_a)}{\lambda} \bullet r_i \qquad i = 1,2,3 \qquad (3.23)$$

where

$\mathbf{u_w}$ = the velocity of the wind field

$\mathbf{u_s}$ = the velocity of the spacecraft

$\mathbf{u_a}$ = the velocity of the phase center of the antenna

$\mathbf{r_i}$ = the antenna pointing vectors

λ = the wavelength

Assume that the Doppler shift due to the motion of the satellite and the rotation of the antenna can be accurately compensated, and let f_i be the measured mean Doppler frequencies, ϕ_i be the antenna elevation pointing angles, θ_i be the antenna azimuth pointing angles, and W_x, W_y, W_z be the x,y,z components of the wind velocity. We can rewrite equation (3.23) in a matrix form:

$$F_D = A\, W\, 2/\lambda \qquad (3.24)$$

where

$$F_D = \begin{vmatrix} f_1 \\ f_2 \\ f_3 \end{vmatrix} \qquad W = \begin{vmatrix} w_x \\ w_y \\ w_z \end{vmatrix} \qquad (3.25)$$

$$r_i = \sin\phi_i \cos\theta_j\, x + \sin\phi_i \sin\theta_j\, y + \cos\phi_i\, z \qquad (3.26)$$

with i=1, 2,3 and j=1,2,3

So **A** has the following form:

$$\mathbf{A} = \begin{vmatrix} \sin\phi_1\cos\theta_1 & \sin\phi_1\sin\theta_1 & \cos\phi_1 \\ \sin\phi_2\cos\theta_2 & \sin\phi_2\sin\theta_2 & \cos\phi_2 \\ \sin\phi_3\cos\theta_3 & \sin\phi_3\sin\theta_3 & \cos\phi_3 \end{vmatrix} \tag{3.27}$$

In practice ϕ_i and θ_j can only equal to a limited set of values which depend on the antenna pointing angles, the antenna scan schemes, and the measurement pattern used in the system. For example, the elevation angle ϕ_i can only be equal to 30° or 35°.

Furthermore, if we assume that the vertical component is independent of the horizontal components and can be estimated separately from the horizontal components, we can write the above matrices in a two-dimensional format.

$$\mathbf{A} = \begin{vmatrix} \sin\phi_1\cos\theta_1 & \sin\phi_1\sin\theta_1 \\ -\sin\phi_2\cos\theta_2 & \sin\phi_2\sin\theta_2 \end{vmatrix} \tag{3.28}$$

and

$$\mathbf{F_D} = \begin{vmatrix} f_1 \\ f_2 \end{vmatrix} \qquad\qquad \mathbf{W} = \begin{vmatrix} w_x \\ w_y \end{vmatrix} \tag{3.29}$$

Notice that the elements in $\mathbf{F_D}$ of (3.29) are not direct measurements of the Doppler frequencies. They are equal to the subtraction of the Doppler shifts caused by the vertical component of the hydrometeor motion from the measured Doppler frequencies.

3.3.2 ERROR ANALYSIS

The major sources of errors in calculating the wind fields are a) estimation errors of the mean Doppler frequencies, b) estimation errors of antenna pointing angles, and c) tracking errors of the mean Doppler frequency caused by satellite motion. In the following section, we assume that the Doppler shift caused by satellite motion is accurately compensated, and discuss only the error bounds of wind measurements resulting from antenna pointing errors and estimation errors of mean Doppler frequencies.

3.3.3 ERROR BOUND CAUSED BY FREQUENCY UNCERTAINTY

When we express the linear equation of (3.24) in a vector form, and under the assumption that there is no antenna pointing error, the error resulting from uncertainties in frequency measurements is equal to

$$\delta W_f = A^{-1}\, \delta F_D\, \lambda/2 \tag{3.30}$$

where $\delta \mathbf{F}_D$ is the frequency uncertainty and $\delta \mathbf{W}_f$ is the error in the wind-field estimates. To derive the upper bound of equation (3.30), we take $\mathbf{A}^{-1}$ as a linear operator in a metric space. The definition of the norm of $\mathbf{A}^{-1}$ in a metric space is equal to

$$||A^{-1}|| = \max_{||\mathbf{x}||=1} ||A^{-1}x|| \tag{3.31}$$

where $\mathbf{x}$ is an any unit vector in the metric space [55]. It is known for a linear operator in a metric space that the following relationship holds:

$$||A\,x|| \le ||A||\,||x|| \tag{3.32}$$

where $\mathbf{x}$ is any vector in the metric space. Using this equation, the upper bound of equation (3.30) can be expressed as:

$$||\delta W_f|| \le ||A^{-1}||\, ||\delta F_D||\, \lambda/2 \tag{3.33}$$

Up to now we did not specify which norm or metric space to be used in this discussion. The choice of norm often depends upon the objective and analysis, as well as mathematical convenience. It is usually difficult to find the norm of a linear operator in an arbitrary metric space. However, if the metric space is chosen to be l_∞space, the norm of $\mathbf{A}^{-1}$ is well derived as the maximum row sum of absolute magnitudes in $\mathbf{A}^{-1}$[55-56]:

$$||A^{-1}|| = \max\left\{\sum_{j=1}^{N} |a_{ij}|\right\} \qquad i = 1,2,...,M \tag{3.34}$$

where N and M are numbers of columns and rows in $\mathbf{A}$ respectively. With $||\mathbf{A}^{-1}||$ defined as in (3.34), we can always find a unit vector $\delta\mathbf{F}_D$ such that when $\delta\mathbf{F}_D$ is substituted into equation (3.33), then the left side of (3.33) is equal to the right side. Therefore, equation (3.33) is the minimum upper bound of measurement errors in the l_∞space. With values in a limited set of pointing angles θ given in Table 3.3, from equation (3.34), we have numerically calculated the norm of $\mathbf{A}^{-1}$ The results are listed in Table 3.4.

Table 3.4 Norm of linear operator $\mathbf{A}^{-1}$in l_∞ space

θ_1 in rad	$\|\|\mathbf{A}^{-1}\|\|$	θ_2 in rad	$\|\|\mathbf{A}^{-1}\|\|$
0.307	6.617	0.2567	6.866
0.79	2.843	0.702	2.69
1.084	4.27	0.964	3.06
1.336	8.57	1.182	4.6
		1.38	9.2

Therefore, under the assumed condition, from equation (3.33) the upper bound of the measurement errors of the wind fields due to uncertainty in frequency measurement is

$$|| \delta W_f || < 4.6 \lambda \, || \delta F_D || \quad (3.35)$$

so that if the required wind measurement error is to be less than 1 ms^{-1}, the errors of mean Doppler frequency measurements need to be less than 23 Hz. This result may be overly optimistic since it does not take into account errors in the measurements of the vertical components of wind vectors.

3.3.3 ERROR DUE TO UNCERTAINTIES IN ANTENNA POINTING ANGLES

The error analysis due to the antenna pointing error involves the analysis of a non-linear operator in a metric space. The analysis of a non-linear operator is usually much more difficult than that of a linear operator. If the operator is differentiable (in our case, it certainly is), the errors resulting from small errors in antenna pointing angle θ and ϕ can be expressed as [56]:

$$|| \delta W_a || = \frac{\lambda}{2} \left|\left| \left(\sum_{i=1}^{M} \frac{d}{d\phi_i} A^{-1} \delta\phi_i + \sum_{j=1}^{N} \frac{d}{d\theta_j} A^{-1} \delta\theta_j \right) F_D \right|\right| \quad (3.36)$$

where $\delta \mathbf{W}_a$ are vectors of errors, $\delta\phi_i$ and $\delta\theta_j$ are antenna pointing errors, and M and N are numbers of different elevation angles and different horizontal angles in matrix **A** respectively. Again, by using the relationship $|| \mathbf{A} \mathbf{x} || \leq || \mathbf{A} || \, || \mathbf{x} ||$ and $\mathbf{F}_D = \mathbf{A} \mathbf{W} \, 2/\lambda$, the above equation can be rewritten as

$$|| \delta W_a || \leq \left|\left| \left(\sum_{i=1}^{M} \frac{d}{d\phi_i} A^{-1} \delta\phi_i + \sum_{j=1}^{N} \frac{d}{d\theta_j} A^{-1} \delta\theta_j \right) A \right|\right| \, || W || \quad (3.37)$$

where

$$\left\| \left(\sum_{i=1}^{M} \frac{d}{d\phi_i} A^{-1}\,\delta\phi_i + \sum_{j=1}^{N} \frac{d}{d\theta_j} A^{-1}\,\delta\theta_j \right) A \right\| \tag{3.38}$$

is a non-linear operator. We calculated the norm of this non-linear operator in a l_∞ space with the angles listed in table 3.3. For $\delta\phi = 0.001$ rad and $\delta\theta = 0.001$ rad, the norm is listed in Table 3.5.

Table 3.5 Norm of non-linear operator (3.38) in l_∞ space

Space shuttle orbit		Near polar orbit	
θ_1 in rad	$\|\cdot\|$	θ_1 in rad	$\|\cdot\|$
0.307	0.0086	0.2567	0.0093
0.79	0.0027	0.702	0.0029
1.084	0.0051	0.964	0.0034
1.336	0.0113	1.182	0.006
		1.38	0.0125

According to the value in Table 3.5, the wind error caused by an antenna pointing error of 0.001 rad can be calculated with equation 3.37:

$$\| \delta \mathbf{w}_a \| \le 0.0125 \, \| \mathbf{w} \|$$

3.3.4 THE TOTAL ERROR BOUND

The compound error in one measurement due to both uncertainties in frequency measurement and in pointing angle can be written as:

$$\| \delta w_f \| \le \alpha \, \| F_D \| + \beta \, \| w \| \tag{3.39}$$

where α and β are constants whose values are dependent upon the antenna pointing angles, the scan mode, and the measurement pattern as well as the number of independent measurements. For a single measurement of a wind vector, under the condition discussed in the section 3.3.3, α is 4.6λ and β is 0.0125. If the second term in equation (3.39) is ignored, to obtain 1 ms^{-1} accuracy in measurements of wind vectors, the frequency errors need to be less than 23 Hz. Notice, from equation (3.39), that the measurement error resulting from the antenna pointing error is increased with the true wind speed.

3.4 CONCLUSIONS AND RECOMMENDATIONS FOR FURTHER STUDY

a) The second term of equation (3.44) depends upon the true windspeed. When the windspeed increases, the error in the measurement due to a fixed antenna pointing-angle error also increases.

b) Throughout the numerical calculations of the norms, we have assumed that the vertical components of the wind vectors were known. In practice, the estimation or measurement of vertical velocity certainly contains error. Therefore, the norm should be larger than those calculated in this chapter.

c) We have assumed that the Doppler shift due to satellite movement can be very accurately compensated. Otherwise it will cause a bias in the wind measurement due to the compensation errors.

d) The above error analysis is based upon the errors in measurements of the mean Doppler frequency and estimation of the Doppler shift of the satellite. However, these estimation errors and measurement errors are usually functions of the SNR of the received signal. A final analysis concerning SNR of the system should be performed.

e) The error analysis conducted above is crude; there may be other factors which need to be considered in evaluation of the performance. A method used in the LAWS study may also be applicable to the RAWS: namely error analysis through computer simulation. In that method, the error is analyzed by using a Monte Carlo technique; each source of error is considered independently, and values are assigned to the sources by using random number generators that have the appropriate distribution functions. This can be used as a topic of future study.

f) Comparing the prf of a lidar system (about 8 Hz for LAWS) and the prf of a radar system (3480 Hz in our case), it seems that the radar system has an advantage of using higher prf than the lidar system. However, for measurement of Doppler shift, the lidar only needs one pulse while the radar system needs 64 or more pulses. Thus the radar system only has a slight advantage on prf over the lidar system with the current technology.

Chapter 4

Estimation of Moments of Power Spectrum

4.1 MOMENTS OF SPECTRUM

In Doppler radar signal processing, iare often required to estimates of the moments of the power spectra of radar echoes. An ith moment of the power spectral density of echoed signal, m_i, is defined as:

$$m_i = \frac{\int_{-\infty}^{+\infty} f^i S(f)\, df}{\int_{-\infty}^{+\infty} S(f)\, df} \tag{4.1}$$

where S(f) is the power spectral density function of the signal. For most weather radars, only the first three moments are important [44]:

(1) mean power of the signal or zeroth moment which indicates the total signal energy returned from the target. In wind measurements from clouds, the zeroth moment is proportional to the echo from hydrometeors, and it may also reflect the attenuation caused by clouds or precipitation. This information may be useful for deriving the precipitation rate. However, it does not directly relate to the winds.

(2) the mean Doppler velocity or the first moment of the normalized power spectral density is a measure of the radial component of the target velocity. This is an essential parameter in the estimation of wind vectors, and reflects a weighted average radial velocity of wind fields.

(3) The second moment is useful for deriving the root-mean-square (RMS) width of the power spectrum (or spectral width). It is a measure of the velocity dispersion, i.e., the shear or turbulence within a resolution volume.

In the study of airborne radar wind sensors, the first moment is the fundamental variable for deriving the Doppler shift caused by the wind-driven droplets in clouds. The spectral width derived from the first and the second moment may be useful for determining the error in estimates of the first moment. In this chapter, we discuss the algorithms for estimating the first moment of the power spectral density. Monte Carlo simulations were applied to evaluate the second-order statistics of the algorithms discussed in this chapter. Since all of the estimators are functions of the SNR and the spectral width, results of the computer simulations are presented with the RMS errors as functions of SNRs and spectral widths. The discussion and the computer simulations are based on normalized frequencies which range from -1 to 1. However, the results can be easily converted to a specific application like RAWS, by multiplying the results with the Nyquist frequency.

4.2 INTRODUCTION TO RANDOM SIGNALS AND SPECTRAL ANALYSIS

4.2.1 RANDOM PROCESS

Before we discuss the algorithms for estimating the moments of the frequency spectrum, let us briefly review some pertinent concepts of random processes and their power spectral densities.

STATIONARY PROCESS

A process x(t) is said to be a wide sense(or weakly) stationary process if and only if both the expected value and the variance of the random process are constants and its covariance between the values at any two time points, t_1 and t_2, depends only on (t_2-t_1), the interval between the time points, and not on the location of the points along the time axis. Mathematically, we can express these conditions as:

$$E(x(t)) = \mu$$

$$\mathrm{var}(x(t)) = \sigma^2$$

$$R_{xx}(t_1,t_2)= E(x(t_1)\, x^*(t_2)) = R_{xx}(t_2-t_1) \tag{4.2}$$

Radar echoes are often assumed to be stationary random processes; at least over short periods, most radar echoes do resemble stationary processes. There are cases in which the radar echoes cannot be considered as stationary processes. One such example is that the antenna sweeps over several beamwidths during a measurement, the radar echoes may come from several different resolution volumes. Therefore, the spectrum of the radar echo may be gradually changing during the measurement, and may not be considered as a stationary random process.

ERGODIC PROPERTIES OF A RANDOM PROCESS

In addition to the assumption of stationarity, we also assume that the radar echoes are ergodic random processes. A random process x(t) is said to be ergodic if its time averages equal its ensemble averages. In almost all of the cases, we may only be concerned with the ergodicities of a few parameters of a random process. For example, the ergodicities of the mean and the autocorrelation are essential to spectral analysis.

4.2.2 POWER SPECTRAL DENSITY

For a stationary random process, the autocorrelation function and the power spectral density are defined as

$$R_{xx}(\tau)= E(x(t+\tau)\, x^*(t)) \tag{4.3}$$

$$S(f) = \int_{-\infty}^{+\infty} R_{xx}(t)\, e^{-j2\pi ft}\, dt \tag{4.4}$$

The autocorrelation function $R_{xx}(\tau)$ is the Fourier transform of the power spectral density S(f), and provides the basis for spectral analysis.

As a practical matter, one does not usually know the statistical autocorrelation function. Thus, it is often necessary to assume that the random process is ergodic in its first and second moments. The statistical autocorrelation function of an ergodic random process can be written as:

$$R_{xx}(\tau) = \lim_{T\to\infty} \frac{1}{2T} \int_{-T}^{+T} x(t+\tau)\, x^*(t)dt \tag{4.5}$$

From this equation, it can be shown that the PSD of an ergodic random process is equal to :

$$S(f) = \lim_{T\to\infty} E\left\{ \frac{1}{2T} \left| \int_{-T}^{+T} x(t) \exp(-j2\pi ft) \right|^2 \right\} \tag{4.6}$$

The expectation operator is required in the above equation since the ergodicity does not couple through the Fourier transform; that is, the limit in the above expression without the expectation operator does not converge in any statistical sense [57] [58].

4.3 COMPUTER SIMULATION OF RANDOM SIGNALS

4.3.1 SHAPE OF THE DOPPLER SPECTRUM

There are two important parameters in describing a stationary random process; one is the probability density function; and the other is the power-spectral-density function. A radar echo consists of the sum of the return signal and noise. The noise is often assumed to be white and Gaussian. Since the radar echoes from a resolution volume are from multiple scatterers, it is reasonable to assume that the radar echoes have Gaussian probability distributions as implied by the central limit theorem. Hence, the power of a radar echo should have an exponential distribution.

The shapes of spectra of weather-radar echoes are influenced by both the shapes of the transmitted pulses and the antenna patterns. If we assume that both the shapes of transmitted pulses and the radar pattern can be approximated by Gaussian functions, the shapes of spectra of weather echoes can be approximated by the convolutions of two Gaussian functions, and, should also resemble Gaussian functions. In addition, as the Fourier Transform of a Gaussian function results in a Gaussian function, the autocorrelation function of a weather radar echo is often assumed to be Gaussian. In the following discussion, we will always make the assumption that the shape of the spectrum of a weather radar echo is Gaussian.

In the computer simulation of weather radar echoes, besides the shapes of spectra, we also need to consider the spectral widths of the radar echoes. In the case of RAWS, because of the high speed of the spacecraft, the spectral widths of the weather radar echoes are determined primarily by the beamwidth of the antenna. For example, as derived in Chapter 3, the 3 dB bandwidth of the Doppler frequency of a returned radar signal at 35 GHz is roughly equal to

$$B_D = \frac{2v}{\lambda}\beta = \frac{2v}{L} = 1875 \text{ Hz}$$

where v is the velocity of the spacecraft, λ is the wavelength, β is the antenna beamwidth and L is the antenna aperture. The ratio of the bandwidth of the Doppler frequency to a 3500 Hz PRF is equal to

$$\frac{B_D}{2f_N} = \frac{1875}{3500} = 0.53$$

In a pulsed-Doppler radar, the PRF acts like a sampling frequency to the weather radar echoes. Therefore, from the above calculation, the bandwidth of the Doppler frequency of radar echoes is approximately half of the Nyquist interval. If we consider that turbulence, wind shear, motion of the antenna beam, and target drift all would add decorrelation effects to the returned signals and broaden their spectra, the actual radar-signal spectral widths may be greater than calculated above. A quantitative study of the effect of antenna scan rate on signal decorrelation can be found in [59].

4.3.2 GENERATING RANDOM VARIABLES WITH SPECIFIC PDFS

In computer simulations of radar signals, it is often necessary to generate random processes with determined probability density functions and correlation functions. In this section, we review some of these methods for generating a random variable with a specified probability density function (PDF). In the next section, we discuss how to generate a random process with a specified autocorrelation function.

Generating random variables with a specific PDF often starts with generating a series of uniformly distributed random numbers. Since the computer-generated random sequence is quasi-random, the random-number generator should be chosen according to the application. For Monte Carlo simulations with several hundred runs, and each run requiring thousands of samples, we need to choose a random number generator which produces statistically uncorrelated numbers with a very long cycle. For example, in the simulations performed in this chapter, the random number generator is chosen from [60], and this generator has a cycle of 2^{30}.

Generating random variables other than those with uniform distributions can be achieved through performing transformations on uniformly distributed random variables. It is known that if two random variables x and y are related by the expression $x = f(y)$, then the PDF of y is equal to [61]:

$$p(y) = p(x) \left| \frac{dx}{dy} \right| \tag{4.7}$$

In particular, if x is a uniform random variable one can obtain the desired random variable by the transformation $y=F^{-1}(x)$, where F(y) is the distribution function of y. For generating some random variables, multi-variable transformations may be needed. Let x_1 and x_2 be uniform random variables and y_1 and y_2 be random variables with the desired probability distributions. Then the joint PDF of y_1 and y_2 is

$$p(y_1, y_2)\, dx\, dy = p(x_1, x_2) \left| \frac{\partial(x_1, x_2)}{\partial(y_1, y_2)} \right| dx\, dy \tag{4.8}$$

where $\left| \frac{\partial(x_1, x_2)}{\partial(y_1, y_2)} \right|$ is the Jacobian determinant.

GENERATING A GAUSSIAN DISTRIBUTION

An important example of the use of variable transformations is the Box-Muller method for generating random deviates with a normal distribution,

$$p(y)dy = \frac{1}{\sqrt{2\pi}\,\sigma} e^{-y^2/2\sigma^2} dy \tag{4.9}$$

Consider the transformation between two uniform random variables on (0,1), x_1, x_2 and two quantities y_1, y_2,

$$y_1 = \sqrt{-2 \ln x_1} \cos (2\pi x_2)$$

$$y_2 = \sqrt{-2 \ln x_1} \sin (2\pi x_2) \tag{4.10}$$

Equivalently we can write

$$x_1 = e^{\left[-\frac{1}{2}(y_1^2 + y_2^2)\right]}$$

$$x_2 = \frac{1}{2\pi} \arctan \frac{y_2}{y_1} \tag{4.11}$$

Now the Jacobian determinant can readily be calculated:

$$\frac{\partial(x_1, x_2)}{\partial(y_1, y_2)} = e^{\left[-\frac{1}{2}(y_1^2 + y_2^2)\right]} \tag{4.12}$$

Therefore, y_1 and y_2 all have normal distributions as a result of the transformation.

GENERATING AN EXPONENTIAL DISTRIBUTION

The power of a weather radar signal is often exponentially distributed. It can be generated from a uniform distribution. Let x be a uniformly distributed random variable and y be an exponentially distributed random variable. With the transform $x = F(y) = \exp(-y)$, y has an exponential distribution.

GENERATING A RAYLEIGH DISTRIBUTION

The voltages of weather signals generally have Rayleigh distributions, which can be expressed as follows:

$$p(y) = \frac{y}{\sigma} e^{-y^2/2\sigma} \tag{4.13}$$

Therefore, with the transform $x = F(y) = e^{-y^2/2\sigma}$, $y = \sqrt{2\sigma(-\ln(x))}$ has a Rayleigh distribution.

4.3.3 GENERATION OF A RANDOM PROCESS WITH A SPECIFIC AUTOCORRELATION FUNCTION

4.3.3.1 Using An ARMA Model

A large number of random processes can be classified as certain autoregression and moving-average processes with p as the order of autoregression and q as the order of moving average. Such autoregression and moving average processes are usually denoted as ARMA(p,q). Even some random processes, which cannot be classified as ARMA(p,q), may be approximated by certain ARMA(p,q) models. Therefore, we may use an ARMA model to simulate the weather radar echoes. The spectra of radar signals returned from weather targets are expected to be Gaussian in shape. We may use an autoregression model, AR(p), to approximate such a process.

An ARMA(p,q) modeling only gives the desired autocorrelation function of the process. To make the random process have a specific probability distribution often requires a non-linear transformation after the ARMA modeling. In practice, such a non-linear transformation is often difficult to implement. A detailed study of such methods for generating random processes with specified spectra and probability distributions can be found in [62] .

4.3.3.2 Using An Inverse Fourier Transform

Here, we describe a method using an inverse FFT to generate weather-like signals. This method was discussed in [63] and [64]. We applied this method in generating weather radar echoes with Gaussian power spectral densities and exponential probability distribution functions in the computer simulations of this chapter. As discussed in section 4.2.2, a weather radar signal normally has a Gaussian-shaped spectrum, and its power is exponentially distributed. The detailed steps for generating weather signals with an inverse FFT method are depicted below:

- The first step is to specify the power spectrum of the weather radar echo from a target by

$$G_n = \frac{1}{\sqrt{2\pi}\,\sigma} e^{-(f_n - f_m)^2/2\sigma^2} \qquad n=0,1,\ldots,M-1 \qquad (4.14)$$

where

f_n = n th discrete frequency
M = total number of discrete frequencies
G_n = the discrete spectral coefficient corresponding to f_n
f_m = the power-weighted mean frequency
σ = is the standard deviation of the spectrum, which is defined as spectral width.

In all the computer simulations of this chapter, f_n and f_m were normalized with a Nyquist interval [-1.0, 1.0]. When f_n or f_m are not in the range of -1.0 to 1.0, aliasing occurs and the spectrum folds into the interval [-1.0, 1.0].

- Second, we assume the additive noise present in the real signal is white, i.e., it has a constant spectral density, and also consider that both simulated signal and noise powers must be exponentially distributed to represent the weather signal. Then, we can write the power spectral coefficient for frequency f_n as:

$$S_n = -\ln(x_n)\left[K\,G_n + \frac{P_N}{M}\right] \qquad (4.15)$$

where $0 \le x_n \le 1$ and is uniformly distributed. P_N, the total noise power, can be arbitrarily set to unity. K is equal to

$$K = \mathrm{SNR} \Big/ \sum_{n=0}^{M} G_n \qquad (4.16)$$

- The third step is to decompose the power spectrum into its real, A_n, and imaginary, B_n, components, adhering to the requirement that the phase angles of the sinusoid comprising the spectrum (i.e., the phase spectrum of the time signal) be uncorrelated and uniformly distributed between $(-\pi,\pi)$.

$$A_n = S_n^{1/2} \cos(2\pi y_n)$$

$$B_n = S_n^{1/2} \sin(2\pi y_n) \qquad (4.17)$$

where y_n is a random variable uniformly distributed between(0,1). Notice that $S^{1/2}$ has a Rayleigh distribution, while A_n and B_n have Gaussian distributions.

- The final step is to generate the complex time signal by performing an inverse Fourier transform of A_n and B_n.

$$Z_n = I_n + jQ_n = \sum_{i=0}^{M-1} (A_i + jB_i)\, e^{j2\pi ni/M} \qquad (4.18)$$

where M is the number of samples.

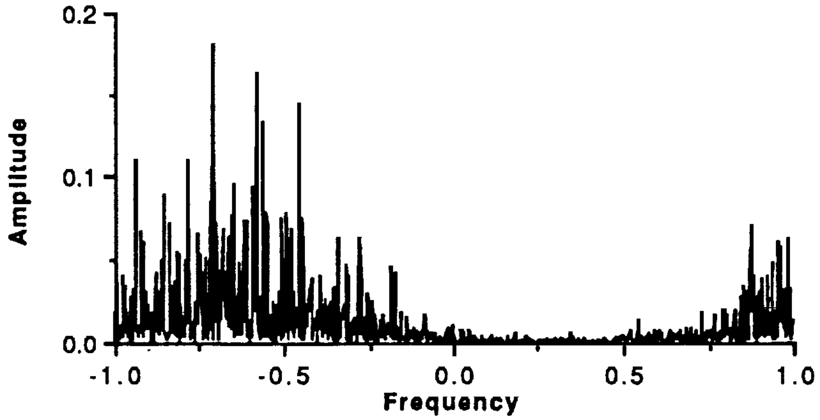

Figure 4.1. Example of computer simulated spectrum of a random signal with spectrum width $\sigma = 0.3$, mean frequency -0.7, and SNR 10 dB.

An example of computer simulated weather radar echo is shown on Figure 4.1. The frequency is normalized to [-1,1]. The mean frequency and the standard deviation are -0.7 and 0.3 respectively. In the computer simulations of this chapter, the total number of sample, M, is chosen as 1024.

4.4 ESTIMATION OF THE MOMENTS OF THE DOPPLER SPECTRUM

The algorithms for estimating of the first moment of the power spectral densities of radar signals can be classified into the following following three categories:

- Algorithms based on the Fast Fourier Transform(FFT) of the signal.
- Algorithms based on the covariance function of the signal (also called pulse-pair method).
- Algorithms based on parametric modeling, such as the autoregressive (AR) and the moving average (MA) models. Only the autoregressive method will be discussed in this chapter.

The algorithms based on the FFT method and the ARMA-model method require evaluation of the power spectral density (PSD) of the return signal first, and

C-2

subsequently the mean of the PSD. The algorithms based on covariance function do not require the calculation of the PSD of the signal. The ARMA methods may not be as efficient as the covariance and the FFT methods when the order of the model is high. In the following sections, we will discuss each of these algorithms in more detail.

4.4.1 FFT METHOD

The amplitude spectrum for a digital signal is often expressed as:

$$X(e^{j\omega}) = \sum_{-\infty}^{\infty} x(n)\, e^{-j\omega n} \tag{4.19}$$

In practice, however, the amount of data is always limited. One of the most widely used PSD estimators, based upon an FFT operation, is typically referred to as the periodogram. For data samples $x_0,\ldots,x_{N-1}$, the periodogram estimate of the PSD is defined as:

$$\hat{S}(f) = \frac{1}{N\Delta t} \left| \Delta t \sum_{n=0}^{N-1} x_n\, e^{-j2\pi f n \Delta t} \right|^2 \tag{4.20}$$

where N is the number of data, Δt is the sampling interval, and f is in the range of $-1/(2\Delta t) \leq f \leq 1/(2\Delta t)$. Use of the periodogram permits us to evaluate the PSD at N equally spaced frequencies $f_m = m\Delta f$ Hz, for m=0,1,...,N-1 and $\Delta f = 1/N\Delta t$. If the Δf factor is incorporated into $\hat{S}(f)$, then (4.20) can be written as:

$$S_m = \hat{S}(f_m)\Delta f = \frac{1}{N} \left| X_m \right|^2$$

$$= \frac{\left| \sum_{n=0}^{N-1} x_n e^{-j2\pi mn/N} \right|^2}{N} \tag{4.21}$$

where X_m are the coefficients discrete Fourier transform (DFT) of x(n).

Not only is the periodogram a biased estimator of the power spectrum, but it is also not a consistent estimator, i.e. when N goes to infinity, $\hat{S}(f)$ may not converge to its mean value statistically [58]. This phenomenon is primarily caused by the absence of an expectation operator in the above equation. Several methods can be used to reduce the variance of the periodogram PSD estimators. One of these methods is to divide a long data sequence into M short sequences, and separately applying each sequence to the periodogram. The results are then averaged.

Estimation of the mean of the PSD with the periodogram is straightforward,

$$\hat{f} = \frac{1}{f_F} \frac{\sum_{m=0}^{M-1} f_m S_m}{\sum_{m=0}^{M-1} S_m} \qquad (4.22)$$

where $f_F = \frac{1}{2\Delta t}$ is the Nyquist frequency, and f_m is defined as $\frac{i}{M\Delta t} - f_F$. $\hat{f}$ ranges from -1.0 to 1.0. It can be shown that (4.22) generally is not a consistent estimator for the mean frequency. Only when the spectral lines are mutually independent, is (4.22) a consistent estimator (see Appendix 4.1).

In equation (4.22), we did not consider the effect of noise. However, the estimate of mean frequency of the PSD is often biased by the noise. If we write the power spectral density for $S(f_m)$ as a sum of the spectra of the signal and noise,

$$S(f_m) = S_m + n_m$$

with S_m and n_m as the discrete spectral densities of the signal and noise respectively at frequency f_m. Equation (4.22) can now be expressed as follows:

$$\hat{f} = \frac{1}{f_F} \frac{\sum_{m=0}^{M-1} f_m (S_m + n_m)}{\sum_{m=0}^{M-1} (S_m + n_m)}$$

$$= \frac{1}{f_F} \frac{\sum_{m=0}^{M-1} f_m (S_m + n_m)}{(S + N)}$$

$$= \frac{m_S}{1 + N/S} + \frac{m_N}{1 + S/N} \qquad (4.23)$$

where m_S is the first moment of the signal spectrum, m_N is the first moment of the noise spectrum, and N/S is the inverse of the SNR. Therefore the bias caused by the noise is equal to

$$\text{Bias} = \frac{m_S N/S}{1 + N/S} + \frac{m_N}{1 + S/N} \qquad (4.24)$$

Notice that in equation (4.24) the bias is a linear function of m_S. When the noise is white, the second term of (4.24) is zero, andthe bias approaches zero as the mean frequency, m_S, approaches zero. This is illustrated by Figure 4.2. When the mean frequency is zero, there is no bias caused by noise.

In addition to the bias caused by noise, the estimator is also biased by aliasing of the spectrum of the signal. From Figure 4.2, it can be observed that, at 0 dB SNR, the estimate suffers a considerable amount of bias. The estimate is about half of the true value of the mean frequency. At 10 dB SNR, the bias is negligibly small in the middle part of the Nyquist interval, and the estimates almost agree with the true values of the mean frequencies. However, when the mean frequency approaches the ends of the Nyquist interval, the estimates starts to curve towards the 0 frequency. This phenomenon is caused by the aliasing of the spectra of the signals. In summary, the FFT estimator of (4.22) only works well when the

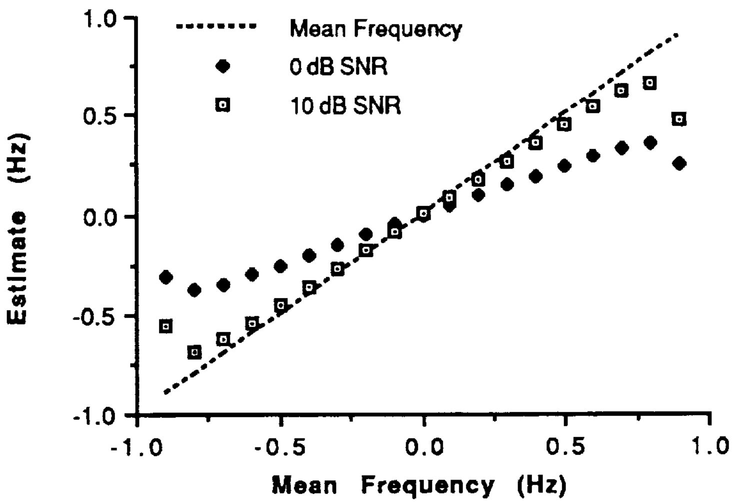

Figure 4.2. Simulation of FFT estimator without de-aliasing and noise suppression, under the condition $\sigma = 0.1$, SNR = 0 dB, and 10 dB, and the number of runs = 200.

signal-to-noise ratio is high and the signal is free of frequency aliasing. In case of poor SNR and frequency aliasing, the estimated mean frequencies yield very large errors as shown in Figure 4.2. In the next two sections, we discuss noise suppression and de-aliasing algorithms that can remove or reduce the bias due to the noise and frequency aliasing.

4.4.1.1 Estimation of The Mean With Noise Suppression

If we assume that the signal and noise are uncorrelated, and the spectral density of the noise can be estimated separately, one way to reduce the bias caused by frequency aliasing is to subtract the noise spectral density, $N(f_m)$, from the derived spectral density and calculate the mean of the resulting spectrum, i.e.,

$$\hat{f} = \frac{1}{f_F} \frac{\sum_{m=0}^{M-1} f_m (S(f_m) - N(f_m))}{\sum_{m=0}^{M-1} (S(f_m) - N(f_m))} \qquad (4.25)$$

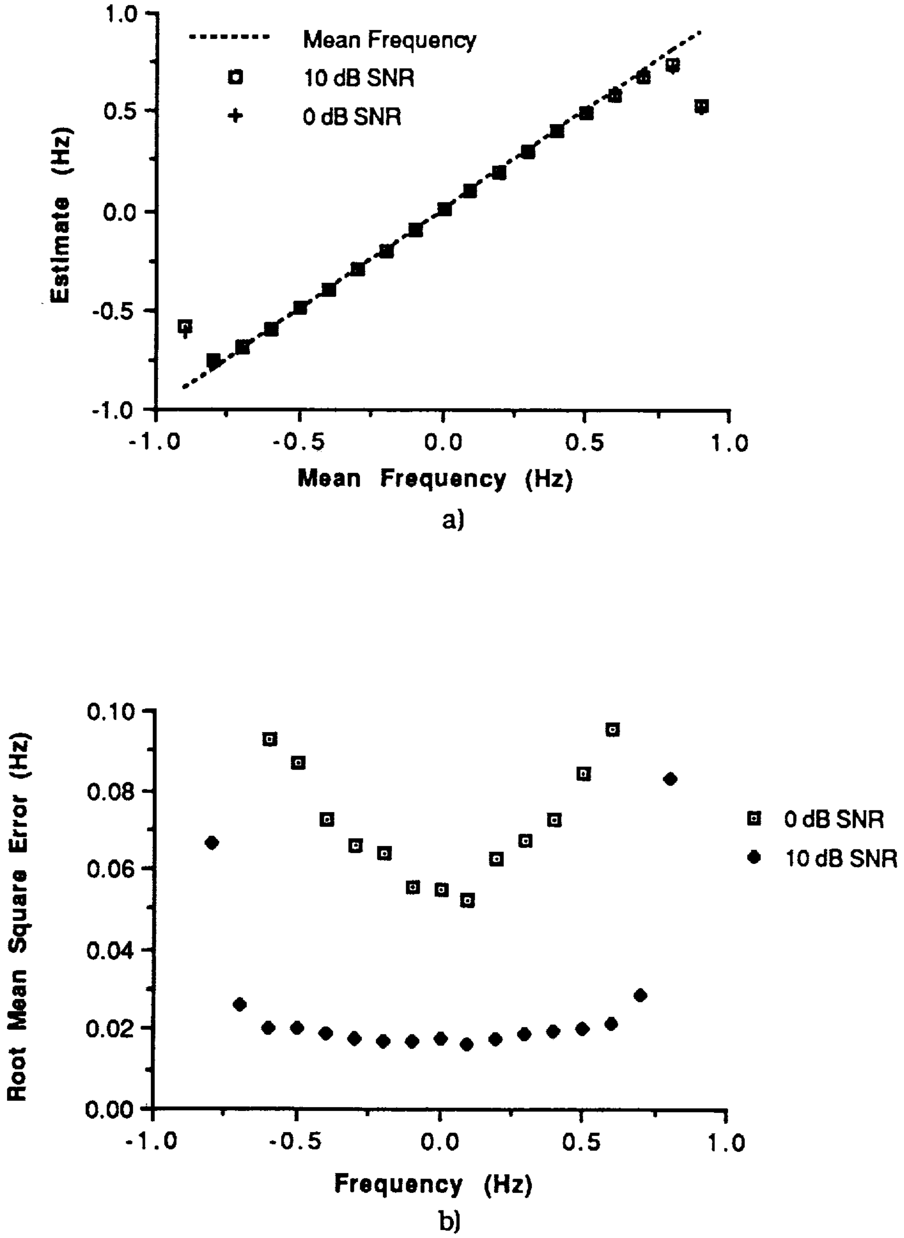

Figure 4.3. Monte Carlo simulation of FFT estimator with noise suppression; a) estimate under the condition $\sigma = 0.1$, SNR = 0 dB, and 10 dB, with 200 runs; b) RMS errors as functions of frequency and the spectral width of power spectrum of signal.

Although this estimator may result in some spectral lines with negative values, the biases are effectively removed from the estimates. This method was examined by Sirmans and Bumgarner [64] with computer simulations. Their results can be summarized as follows: the FFT with noise suppression is an estimator of mean frequency unbiased by noise even for a low SNR and the standard deviation of the estimate with the noise suppressed is comparable to the standard deviation of the signal plus noise mean estimates.

Some of the results of the computer simulations for the noise suppression scheme are presented in Figure 4.3., which shows that the bias caused by noise is removed by the noise suppression. However, the estimates of the mean frequency of the signal are still biased at the frequencies near the ends of the Nyquist interval because of frequency aliasing.

4.4.1.2 FFT Method with De-aliasing

As shown in previous sections, the performance of the FFT method is severely degraded by aliasing of the spectrum. This is particularly noticeable when the spectral width of the signal is large. The effective unambiguous frequency measured by the FFT estimator can be significantly reduced without application of a de-aliasing method. One method to reduce the effect of aliasing is to shift the peak of the spectrum to the center of the Nyquist interval (at zero frequency) before applying the FFT estimator, and add the shifted frequency back in the final estimate. Such an algorithm was discussed by Zrnic [65]. In the computer simulations performed in this chapter, we used a similar method as explained below:

- a) Smooth the periodogram by weighted running average. The size of the window used in the smoothing was selected proportional to the spectral width of the PSD. The maximum size of the window was limited to half of the Nyquist interval.

- b) Search for the peak of the smoothed spectrum of the data, then locate its position, say f_p.

- c) Shift the entire spectrum such that the peak f_p is now at zero frequency.

- d) Apply the following formula to estimate the mean frequency ,

$$\hat{f} = f_p + \frac{1}{f_F} \frac{\sum_{m=0}^{M-1} f_m S'_m}{\sum_{m=0}^{M-1} S'_m} \qquad (4.26)$$

where $S'_m = S_{m-p}$.

In implementing such an algorithm, tradeoffs are encountered in choosing the size of the smoothing window. If the window size is too small compared with the spectral width of the data, the algorithm may select a frequency peak which is not close enough to the true mean frequency, and the bias caused by frequency aliasing cannot be effectively removed. On the other hand, if the width is too large, it will increase the uncertainty of the location of the peak frequency. In the computer simulations performed, we chose the widths of the smoothing windows to be proportional to the spectral width of the signals.

Some results of Monte-Carlo computer simulations of such an algorithm are presented in Figures 4.4. In these computer simulations, the Nyquist intervals are normalized to [-1, 1]. The standard deviation of the spectrum are chosen to be 0.1. The RMS error of the estimate is defined as:

$$\text{RMS ERROR} = \sqrt{\frac{\sum_{m=1}^{M} (\hat{f}_m - \bar{f})^2}{M}} \qquad (4.27)$$

where $\hat{f}_m$ is mth estimate of the mean frequency $\bar{f}$, and M is number of runs.

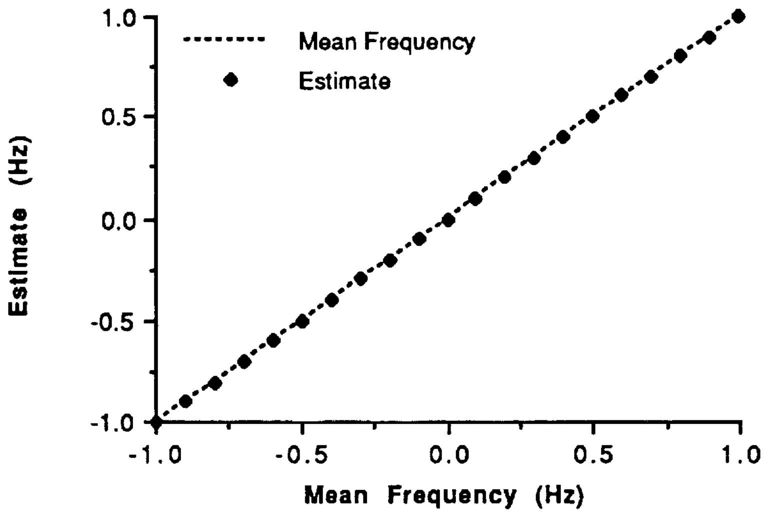

a)

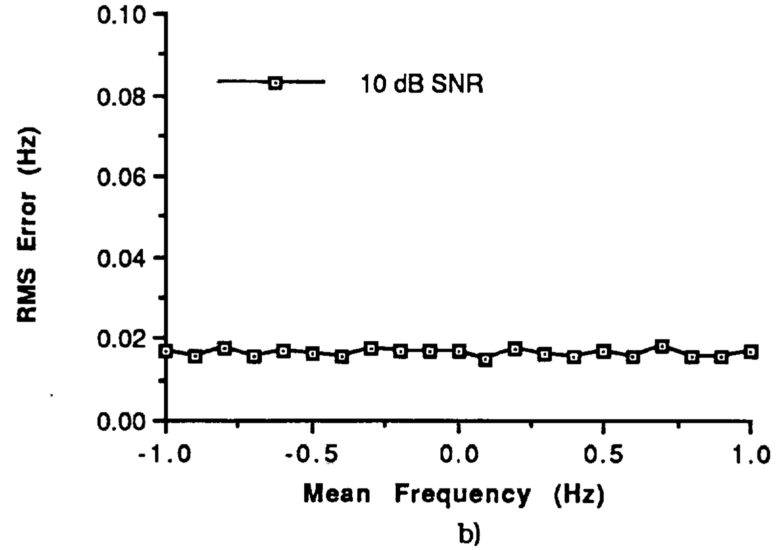

b)

Figure 4.4. FFT Estimator with de-aliasing applied with $\sigma=0.1$, SNR=10 dB, a) the plot of ensemble average of estimates; b) plot of RMS error with 200 runs. For the RAWS parameters, the scale would be from -1.75 kHz to + 1.75 kHz. The frequency shown here is normalized to the Nyquist frequency.

These results show that the de-aliasing algorithm improves the performance of the FFT estimator significantly. Even at a SNR of 0 dB, the estimate is still able to converge to the true mean frequency, indicating the de-aliased FFT estimator is an unbiased estimator of mean frequency.

The fact that the de-aliasing method reduces the bias caused by noise is in agreement with equation (4.25). This equation indicates that, as the mean frequency goes to zero, the bias caused by noise also goes to zero. After applying step c) in the de-aliasing algorithm, the bias caused by noise acts like a zero-mean random variable. Hence, the estimates can converge to the true values of the mean frequencies. However, this is only true when the noise is white For colored noise, noise suppression may need to be applied before applying the de-aliasing algorithm.

4.4.2 THE COVARIANCE ESTIMATOR

The covariance method for computing the moments of the Doppler spectrum has come into widespread use in recent years. These methods have been discussed in many papers: Rummler[66], [67], Benham and Groginsky [68], Miller and Rochwarger[69], Sirmans and Bumgarner[64], [70], and others. The covariance method is a time-domain estimator. Therefore, it does not need to estimate the power-spectral density. One obvious advantage of this method is that it requires fewer computations. In addition, this method does not require equal time interval between sampled pairs, This property makes it possible to combine this method with waveform modulation for removal of range and frequency ambiguities (see Chapter 5).

The following covariance method for estimating the mean of the spectral density is described by Sirmans and Bumgarner [64]. This method, also called pulse-pair processing, is based on the fact that the moments of a random variable x

$$m_n = E(x^n) \tag{4.28}$$

are related to the derivatives of its characteristic function $\Phi(\omega)$, the Fourier transform of its probability density function with a reversal in sign, by

$$j^n m_n = \frac{d^n \Phi(0)}{d x^n} \tag{4.29}$$

Since the autocorrelation function and the power spectral density S(f) constitute a Fourier transform pair, the moments of the power spectral density are related to the derivatives of the autocorrelation function by an equation similar to (4.29):

$$m_n = j^n \frac{R'(0)}{R(0)} \tag{4.30}$$

Expressing the covariance function in a polar form

$$R(\tau) = A(\tau) \exp[j2\pi g(\tau)]$$

where $A(\tau)$ is a real even function of τ and $g(\tau)$ is a real odd function of τ. The mean of the PSD is equal to

$$\hat{f} = \frac{1}{j\pi}\left[\frac{R'(\tau)}{R(\tau)}\right]_{\tau=0} = \left[\frac{d}{d\tau} g(\tau)\right]_{\tau=0} \tag{4.31}$$

Notice that $A'(\tau)$ is an odd function so that $A'(0) = 0$. This is also true for $g(0)$. Therefore $\hat{f}$ can be approximately written as

$$\hat{f} \simeq \frac{g(\tau) - g(0)}{\tau} = \frac{g(\tau)}{\tau} = \frac{1}{\pi\tau} \mathrm{Arg}[R(\tau)] \tag{4.32}$$

In the computer simulations, a maximum-likelihood unbiased estimator of $R(\tau)$ was used [69]:

$$\hat{R}_{xx}(\tau) = 1/N \sum_{n=0}^{N-1} X_{n+1} X^*_n \tag{4.33}$$

$$\hat{f} = \frac{1}{\pi\tau} \arctan\left(\frac{\operatorname{Im}(\hat{R}_{xx}(\tau))}{\operatorname{Re}(\hat{R}_{xx}(\tau))} \right) \tag{4.34}$$

where X_{n+1} and X_n are complex samples of data, spaced τ seconds apart, and $\hat{f}$ ranges from -1.0 to 1.0.

One important fact to note is that a large interspacing between two pulse pairs does not reduce the accuracy of the covariance method. On the contrary, according to [71], when the interspacing increases, the accuracy of the covariance method should also increase because more independent samples of $R(\tau)$ can be achieved. The results of the Monte-Carlo simulation presented in Figure 4.5 agree with this fact: the estimator with longer spacing between pulse pairs give smaller RMS errors. The data used were computer simulated weather radar signals with Gausian spectra. To select different spacing of pulse pairs, the following formula was used to calculate $R(\tau)$:

$$\hat{R}(\tau) = \sum_{i=1}^{M} x(i*k + 1)\, x^*(i*k)$$

where k is interspacing of pulse pairs. Figure 4.5a shows that the covariance estimator is a consistent estimator of the mean frequency.

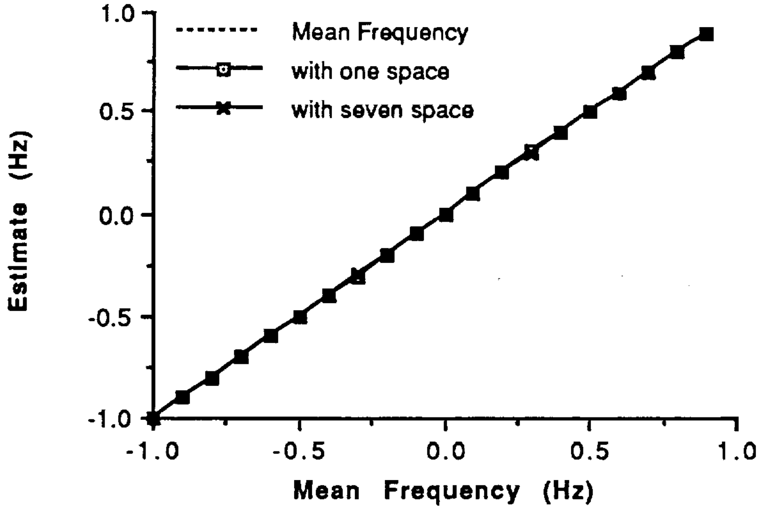

a)

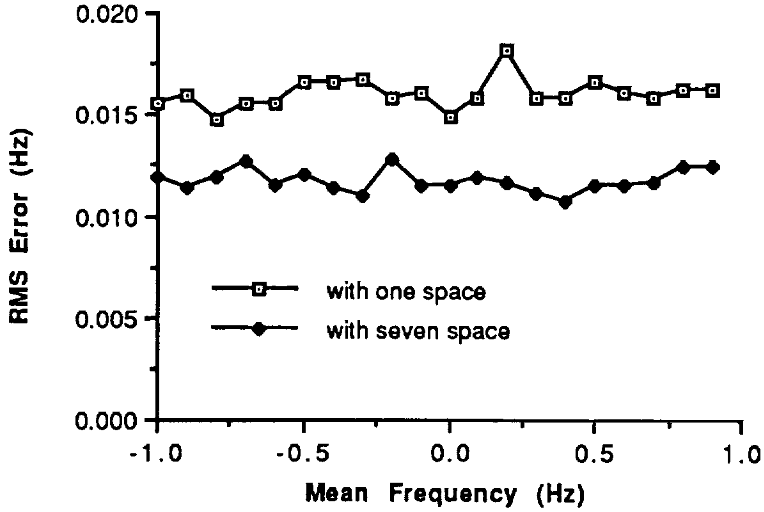

b)

Figure 4.5. Computer Simulation of the Covariance Method with 128 pairs of samples a) mean estimate, with inter-pulse-pair spacing = 1, 7, SNR = 10 dB, $\sigma = 0.1$; b) RMS errors with 200 runs. For the RAWS parameters the scale would be from -1.75 kHz to + 1.75 kHz. The frequency shown here is normalized to the Nyquist frequency.

4.4.3 THE PARAMETRIC METHODS

Many deterministic and stochastic discrete-time processes encountered in practice are well approximated by certain rational transfer function models. Such models, known as the ARMA models, represent random processes, whose PSD are to be estimated in terms of linear difference equations of the following form:

$$x(n) = \sum_{i=1}^{p} a_{p,i}\, x(n-i) + \sum_{k=0}^{q} b_{q,k}\, e(n-k) \tag{4.35}$$

where $b_{q,0}$ is 1 and e(n) is a zero-mean white Gaussian noise sequence. x(n) may be viewed as the response of a linear time-invariant filter whose input is a white noise sequence. The transfer function of such a filter has the form

$$H(f) = \frac{\Theta(f)}{\Phi(f)} = \frac{\sum_{k=0}^{q} b_{q,k} e^{-j2\pi fk}}{1 - \sum_{k=1}^{p} a_{p,i} e^{-j2\pi fi}} \tag{4.36}$$

Equation (4.36) consists of two parts: the autoregressive part and the moving-average part. The autoregressive (AR) portion consists of the poles of the filter and is the denominator of H(f); the moving average (MA) portion consists of the zeros of the filter and is the numerator of H(f). The PSD of the random process x(n) is given by

$$S_{xx}(f) = H(-f)\, H(f)\, S_{nn}(f) = |H(f)|^2 \sigma_{m}^2 \tag{4.37}$$

where σ_{nn}^2 is the variance of the input noise, or the power spectral density of the noise.

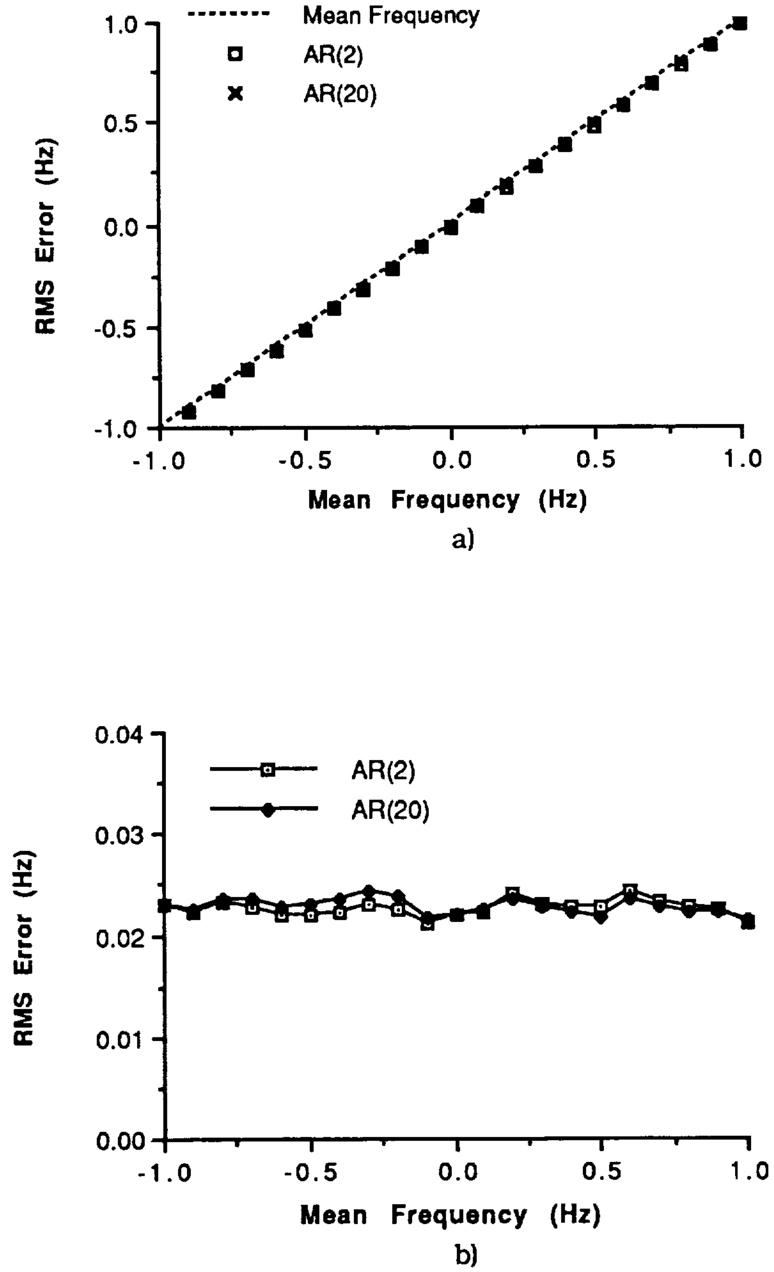

Figure 4.6. Computer Simulation of AR(2) and AR(20) estimators with 200 runs, SNR = 10 dB, σ=0.1, and 128 samples for each run; a) plot of mean estimates; b) plot of RMS errors. For the RAWS parameters the scale would be from -1.75 kHz to + 1.75 kHz. The frequency shown here is normalized to the Nyquist frequency.

To examine the performance of the parametric method in evaluating the first moment of the power spectrum of radar echoes, we will concentrate our attention on the Autoregressive models. Because the power spectrum of the radar echo is expected to be Gaussian in shape, it can be approximated by an all-pole form of a transfer function, or an Autoregressive model as follows:

$$x(n) = \sum_{i=1}^{p} a_{p,i}\, x(n-i) + e_n \tag{4.38}$$

where

e_n = white noise

p = number of poles of the autoregressive model

$a_{p,i}$ = coefficients

There are two ways to solve for the coefficients $a_{p,i}$: one is to use the Yule-Walker equation; the other is to use the Levinson-Durbin Algorithm. Both of these methods are discussed in numerous papers and text books concerning time-series analysis [57],[72],[73] and [74]. In the following, we will only discuss the Levinson-Durbin algorithm. The Levinson-Durbin algorithm requires only order $O(p^2)$ operations, as opposed to $O(p^3)$ for Gaussian elimination in solving the Yule-Walker equation. The algorithm proceeds recursively to compute the parameter sets :

$$\{a_{11}, \sigma_1^2\}, \{a_{21}, a_{22}, \sigma_2^2\}, \ldots, \{a_{p1}, a_{p2}, \ldots, a_{pp}, \sigma_p^2\}$$

where $a_{i,j}$ are estimates of the coefficients, and σ_p^2 is the estimate of the variance of e_n. Note that an additional subscript has been added to the AR coefficients to denote the order. The final set at order p is the desired solution. In particular, the recursive algorithm is initialized by

$$a_{11} = -\frac{R_{xx}(1)}{R_{xx}(0)}$$

$$\sigma_1^2 = (1 - |a_{11}|^2)\, R_{xx}(0)$$

with the recursion for k = 2, 3, ..., p given by

$$a_{kk} = \frac{-\left[R_{xx}(k) + \sum_{n=1}^{k-1} a_{k-1,n} R_{xx}(k-n)\right]}{\sigma_{k-1}^2} \qquad (4.39)$$

$$a_{ki} = a_{k-1,i} + a_{kk} = a_{k-1,k-i}^{*} \qquad (4.40)$$

$$\sigma_k^2 = \left(1 - |a_{kk}|^2\right) \sigma_{k-1}^2 \qquad (4.41)$$

Once the coefficients have been calculated, the power spectral density can be determined from the following

$$S_{AR}(f) = \frac{\sigma^2 \Delta t}{\left|1 + \sum_{k=1}^{p} a_k e^{-2j\pi f k \Delta t}\right|^2} \qquad (4.42)$$

The estimate of the first moment can be determined from equation (4.22). Some of the computer simulation results are presented in Figure 4.6. Figure 4.6a shows the ensemble average of the estimates for AR(2) and AR(20); Figure 4.6b shows the RMS errors for AR(2) and AR(20). It shows that the increase of the order of the AR model does not improve the accuracy of the estimates.

4.4.4 RANDOM SAMPLES AND SPECTRUM ESTIMATION

It is well known that with the conventional equally-spaced samples, aliasing will occur if the power spectrum falls out of the Nyquist interval. However, with unequally spaced samples, we may achieve estimates of the power spectrum of a stationary random process that are not aliased. Perhaps the best known result is that Poisson sampling of a stationary process is alias-free [75]. In the following section, we choose a sampling scheme

$$t_n = nT + y(\Delta T_n - 0.5)T \tag{4.43}$$

where ΔT_n is a random variable having a uniform distribution on interval [0,1] and y is in the range [0,1]. To evaluate the power-spectral density, we used an intuitive formula, which is similar to the definition of PSD for a continuous random signal, given below

$$S(f) = \sum_{n=0}^{N-1} x(t_i)\, e^{-j\omega t_i}\, \Delta_i \tag{4.44}$$

where $\Delta_i = t_{i+1} - t_i$. To evaluate the first moment, we used the definition:

$$m = \lim_{B\to\infty} \frac{1}{B} \int_{-1/2B}^{1/2B} f\, S(f)\, df \tag{4.45}$$

When y = 0, this sampling scheme is identical to the equally spaced sampling scheme and the power-spectrum estimate is equivalent to the DFT method. When y = 1.0, this sampling scheme achieves maximum randomness. Computer simulations were performed using this scheme. The results show that for a signal with a small spectrum width ($\sigma_N < 0.1$), the random sampling scheme does give an alias-free estimate of the power spectrum with reduced SNR. However, when the spectrum width is large, the shape of the estimated PSD is not discernable. Some work done on random sampling can also be found in [76].

4.5 RESULTS OF COMPUTER SIMULATIONS, CONCLUSIONS, AND FUTURE WORK

4.5.1 MONTE CARLO SIMULATION OF THE ESTIMATORS

To compare the statistical properties of the algorithms discussed in this chapter, several Monte-Carlo simulations were completed, each with 200 runs and 128 samples, to calculate the RMS errors for each of the algorithms under different frequencies, spectral widths, and SNRs. The frequencies are normalized to two Nyquist intervals; one is the unit Nyquist interval from -1.0 Hz to 1.0 Hz, the other is from -1750.0 Hz to 1750.0 Hz used by the RAWS. The RMS errors are calculated according to equation (4.27).

The results are presented in Figures 4.7 to 4.12. In Figures 4.7 to 4.9, the RMS errors are plotted as functions of both SNRs and frequencies. In Figures 4.10 to 4.12, the RMS errors are presented as functions of SNRs and spectral widths of the signals. The results indicate that all three estimators are unbiased; the ensemble averages of the estimates converge to the true mean frequencies of the signals. The RMS errors of estimates in these algorithms are independent of frequency. However, the RMS errors are linear functions of the spectral widths of the spectra of the signals in the range of 0.0 Hz to 0.4 Hz for the unit Nyquist interval, or in the range of 0.0 Hz to 700 Hz for RAWS's Nyquist interval.

In comparing of Figures 4.7 to 4.9, it can be seen that when the SNR is high, for example 10 dB, all three estimators give similar performance in term of mean-square errors in estimation. However, when the SNR decreases to 0 dB, the covariance method produces the smallest estimate errors of the three; at 0 dB SNR, the AR(2) estimator is slightly better than the FFT estimator. Previous work performed with these estimators appeared to indicate that the AR(p) modeling should require more computation than the FFT estimator. However, when the order of the autoregressive model p is low, such as 2 in our simulation, the estimator based on an autoregressive model may need less computation power than the FFT estimator.

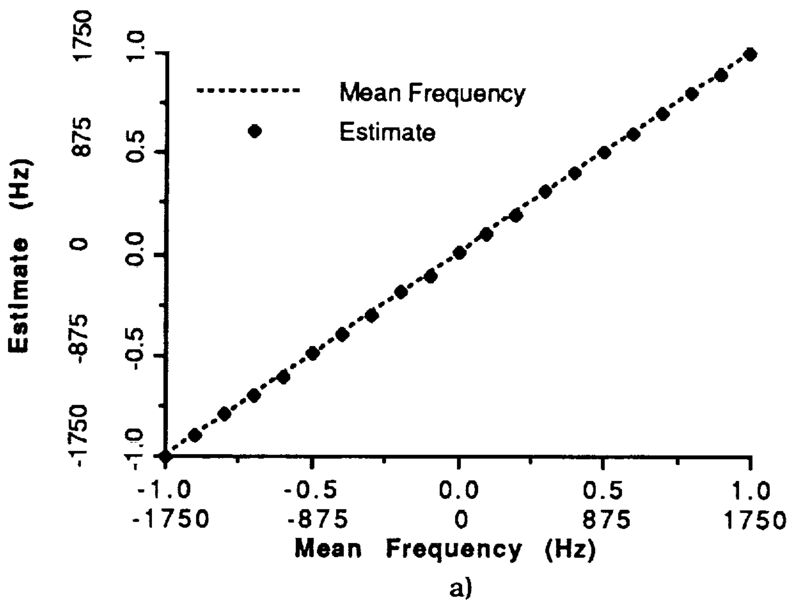

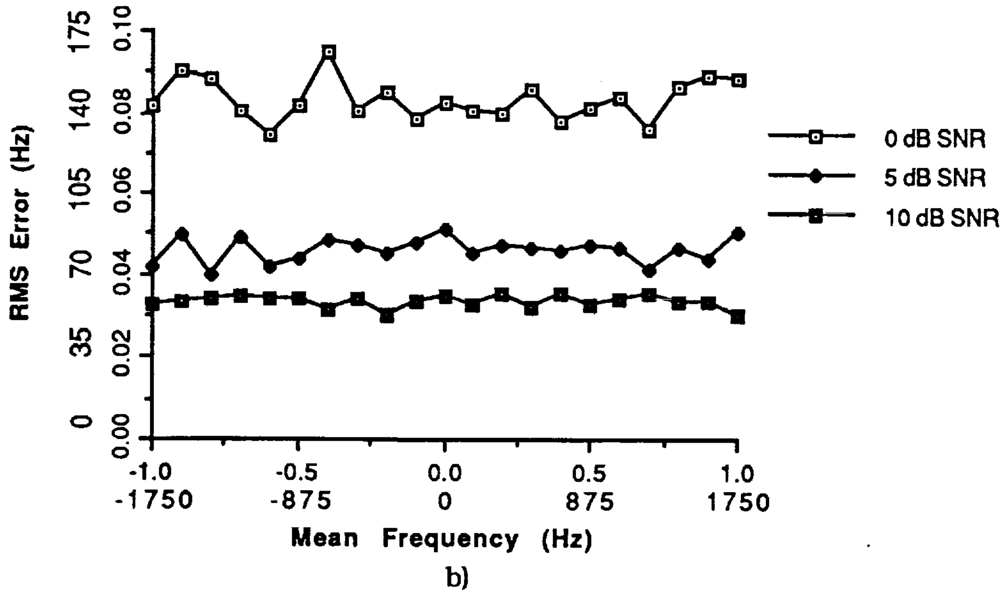

Figure 4.7. Monte Carlo Simulation of FFT estimator with de-aliasing, with 200 runs, and 128 samples for each run; a) Expectation simulated; b) RMS error as a function of SNR, and frequency. Both normalized (-1, 1) and RAWS (-1750, 1750) frequency scales are shown.

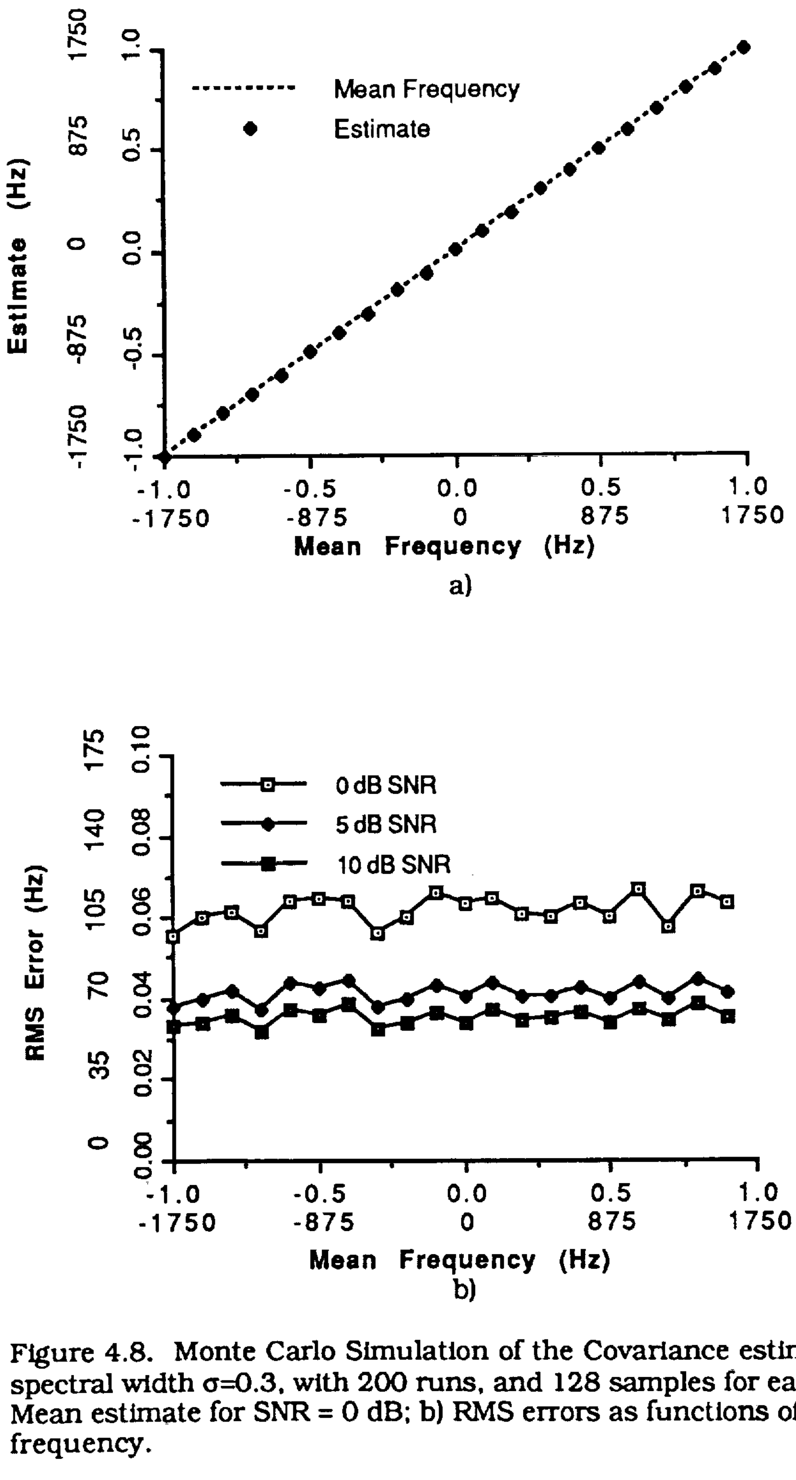

a)

b)

Figure 4.8. Monte Carlo Simulation of the Covariance estimator, the spectral width σ=0.3, with 200 runs, and 128 samples for each run; a) Mean estimate for SNR = 0 dB; b) RMS errors as functions of SNR and frequency.

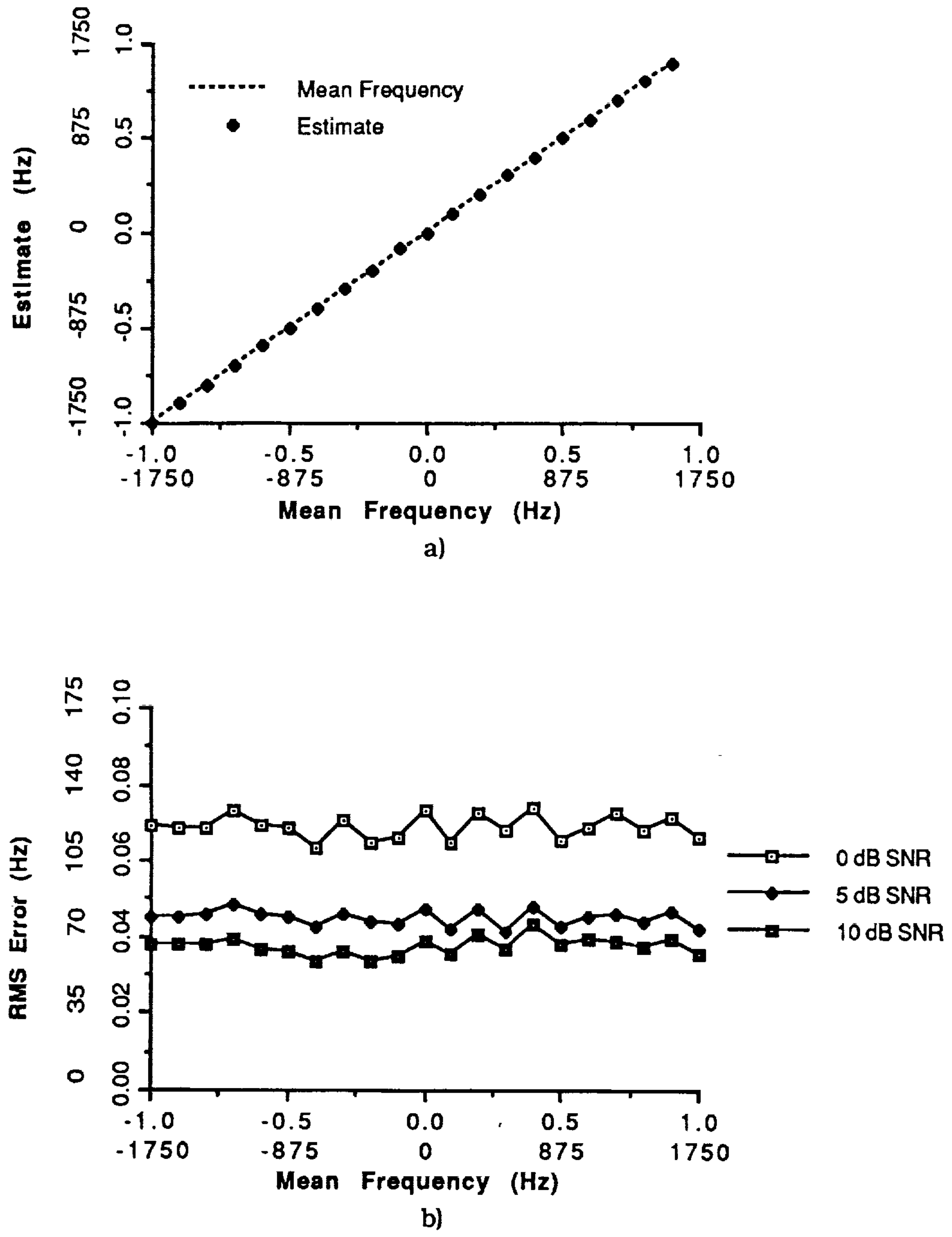

a)

b)

Figure 4.9 Monte Carlo Simulation of the Autoregressive, AR(2), method, with 200 runs, and 128 samples for each run; a) Expectation simulated; b) RMS error as a function of SNR and frequency.

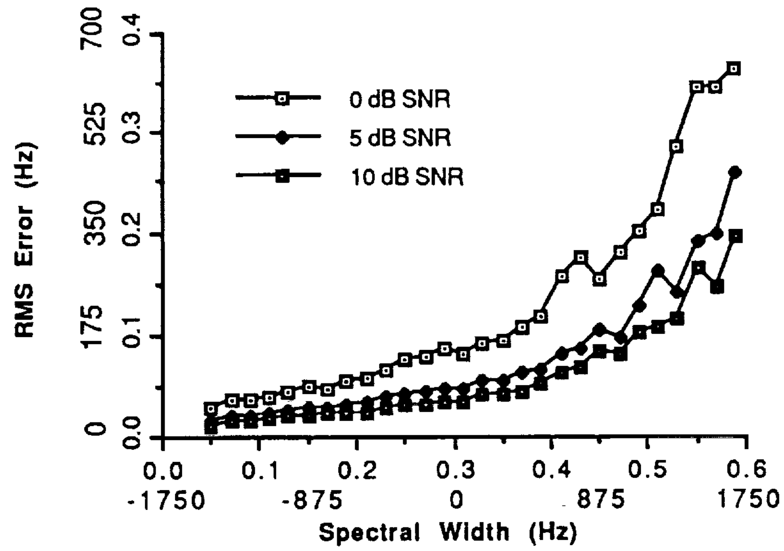

Figure 4.10. Monte Carlo simulation of FFT estimator with RMS error as functions of SNR and spectral width. A fixed mean frequency 0.5 is used in this simulation.

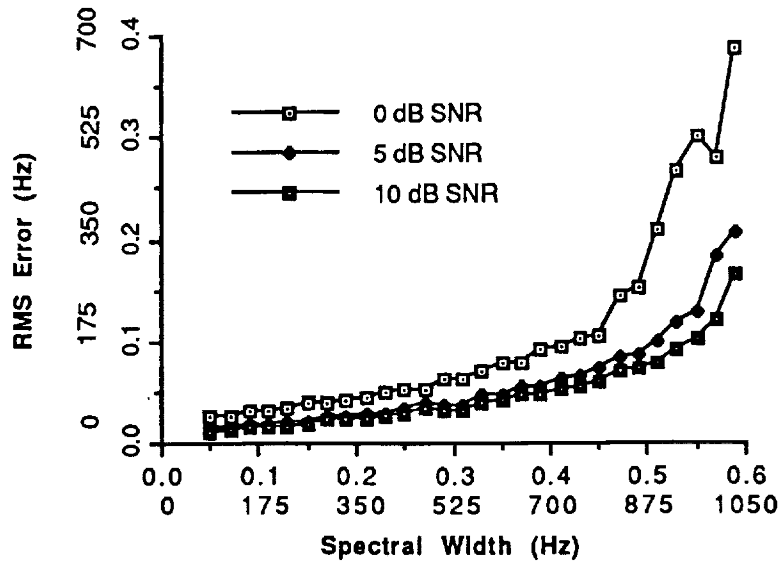

Figure 4.11. Monte Carlo simulation of the covariance estimator with RMS error as functions of SNR and spectral width. A fixed mean frequency 0.5 is used in this simulation.

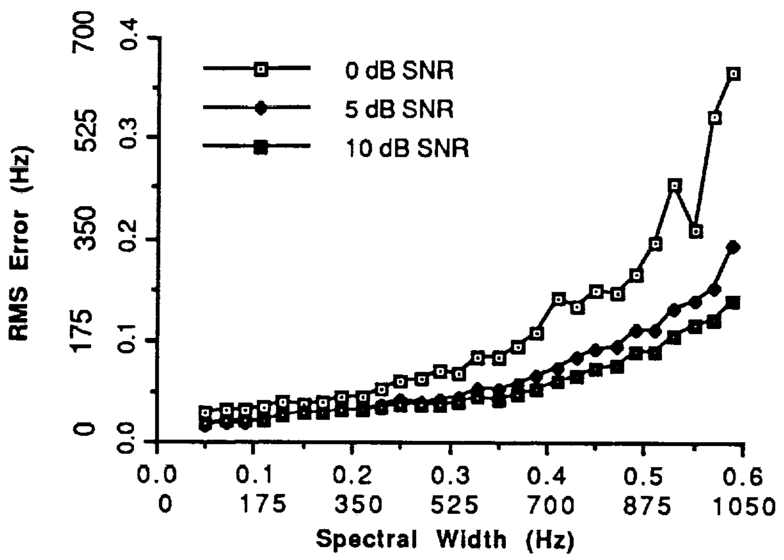

Figure 4.12. Monte Carlo simulation of AR(2) estimator with RMS error as functions of SNR and spectral width. A fixed mean frequency 0.5 is used in this simulation.

4.5.3 CONCLUSIONS AND FURTHER WORK

The de-aliased FFT, the covariance estimator, and the AR estimator are comparable in performance. The errors in the estimates depend on the spectral width and SNRs of the input signals. The errors are mainly functions of the spectral widths of the signals when the SNR is above 5 dB. As discussed in the introduction, the spectral widths of the signals in RAWS are expected to be half of the Nyquist interval. In such cases, all the estimators discussed in this chapter produce large estimation errors, about 10% of the Nyquist frequency. This means, for a 3500 Hz PRF, the RMS errors are around 175 Hz. Part of the estimate error is caused by aliasing of frequency spectrum. To reduce the estimation error caused by aliasing of the spectrum, we need either to increase the PRF or to reduce the inter-spacing between the two pulses in the covariance method. In Chapter 5, we discuss how to use the latter combined with waveform modulations to mitigate the ambiguity problems as well as to reduce the estimation errors caused by aliasing of spectrum.

In this chapter, we discussed the performance of several estimators of mean frequency: the FFT estimator, the covariance estimator, and the estimators based on autoregressive models. The covariance estimator seemed to produce slightly smaller errors than the FFT estimator and the autoregressive-model-based estimators in the computer simulations. However, this is true only under the condition that the power spectrum is symmetric and has only one peak. In practice, interference caused by leakage from the transmitter, or clutter, may cause the returned signals to be non-symmetric or have more than one peak. In these cases, the covariance method may not work as well as the other estimators. We only discussed two autoregressive-model-based estimators, AR(2) and AR(20). The results showed that there was no difference between these two estimators in terms of the estimation errors. We also discussed the random sampling method to estimate spectra of signals. Because of limits on time and volume, we did not investigate the random sampling method in great depth.

APPENDIX 4A PROOF THAT THE FFT ESTIMATOR FOR MEAN IS CONSISTENT

To prove that (4.22) is a consistent estimator of mean frequency, we must show that as M approaches infinity, the variance of (4.22) approaches zero. Let $S(f_i)$ be denoted as $S_i\,\Delta f$, and without loss of generality, assume that

$$\sum_{i=0}^{M-1} S(f_i) = 1\,,$$

then

$$\operatorname{var}\Big(\sum_{i=0}^{M-1} f_i\, S(f_i)\Big) = E\left[\left(\sum_{i=0}^{M-1} f_i\, S_i\right)^2\right]\Delta f^2 - \left[\left(\sum_{i=0}^{M-1} f_i\, E(S_i)\right)\right]^2 \Delta f^2$$

$$= \sum_{i=0}^{M-1}\ \sum_{j=0}^{M-1} f_i f_j\,(E(S_i\, S_j) - \bar{S}_i\bar{S}_j)\Delta f^2$$

$$= \sum_{i=0}^{M-1}\ \sum_{j=0}^{M-1} f_i f_j\, \rho_{S_i S_j}\, \sigma_i \sigma_j\, \Delta f^2 \qquad (4.46)$$

Theoretically, the above result is bound by the following inequalities:

$$\sum_{i=0}^{M-1} f_i^2 \sigma_i^2 \Delta f^2 \quad \sum_{i=0}^{M-1}\ \sum_{j=0}^{M-1} f_i f_j\, \rho_{S_i S_j}\, \sigma_i \sigma_j \Delta f^2 \le \sum_{i=0}^{M-1}\ \sum_{j=0}^{M-1} f_i f_j\, \sigma_i \sigma_j \Delta f^2 = (E(m_1))^2$$

(4.47)

where

m_1 = the first moment of the power spectrum

M = total number of samples

ρ_{ij} = cross correlation coefficients between spectral line i and spectral line j

σ_i = standard deviation of spectral line i

When the spectral lines are mutually independent, the cross-correlation coefficients are

$$\rho_{i,j} = \begin{cases} 1 & \text{when } i = j \\ 0 & \text{when } i \neq j \end{cases}$$

Under this condition, when M goes to infinity, the variance of the FFT estimator approaches zero because $\Delta f \approx 1/M$. Therefore, the estimator is a consistent estimator. On the other hand, if the spectral lines are not mutually independent, the variance is bounded by the square of m_1. Therefore, when spectral lines are not mutually independent, only when m_1 is equal to zero is the FFT estimator a consistent estimator.

Chapter 5

Algorithms for Removal of Range and Frequency Ambiguities

5.1 INTRODUCTION

The characteristics of radar echoes from weather targets impose limitations and tradeoffs on applications of Doppler radar systems for weather observation. Such limitations come from two facts: a) weather targets are distributed quasi-continuously over large spatial regions (tens to hundreds of kilometers), and the strength of radar echoes from a significant weather target easily spans an 80 dB power range [59]; b) the mean Doppler frequencies of radar echoes from weather targets are often higher than the maximum unambiguous frequency of the radar system. In other words, the inherent ambiguity problem in radar systems becomes more prominent in weather radars.

For pulsed-Doppler radars, the unambiguous range, r_a, is generally defined as the maximum distance that a transmitted pulse can travel to a target and echo back to the radar receiver before the next pulse is transmitted. The maximum unambiguous frequency is generally considered as half of the PRF. When a target area is located beyond the unambiguous range, the echoes returning from that area arrive after the next pulse is transmitted. This creates what is commonly referred to as range ambiguity. Radars having uniform PRF and without some form of coding from pulse to pulse cannot discriminate between echoes coming from targets located within the unambiguous range,and those outside this range.

The maximum unambiguous velocity, v_a, measured by a Doppler radar is related to the maximum unambiguous frequency by

$$v_a = \pm \lambda \, prf / 4$$

where λ is the radar wavelength. A velocity higher than the maximum unambiguous velocity causes frequency ambiguity. Range ambiguity and velocity ambiguity are not independent; it can be shown that $v_a r_a = \lambda c/8$. This relation indicates that either the unambiguous range or unambiguous velocity can be increased only at the expense of the other.

For example, in the conceptual model of RAWS described in Chapter 3, the PRF is set to 3500 Hz to avoid range ambiguity. However, if the radar needs to measure 60 m s^{-1} wind speed, the maximum Doppler frequency of radar echoes caused by wind will be 14200 Hz at 35 GHz. This frequency is 8 times as large as the Nyquist frequency of 1775 Hz, and will certainly create frequency-ambiguity problems. In such a case, the true mean frequency of the signal cannot be measured correctly with the conventional methods because of frequency aliasing. On the other hand, if we choose the PRF high enough to satisfy the Nyquist criterion, say PRF = 29000 Hz, there will be no frequency ambiguity. However, with a maximum range of 20 km the radar echoes from different transmitted pulses will overlap. Therefore, to satisfy the required maximum frequency and range of RAWS we have to solve the radar ambiguity problems.

The algorithms developed thus far for reducing radar ambiguities can be classified into one of the following categories:

- Interpulse phase coding: in an interpulse phase coding method, the transmitted pulses are modulated with a sequence of discrete phase codes. At the receiver, a coherent reference signal is used to correlate with the received signals from a specific trip. The objective of the phase coding is to make signals returned from different trips have poor cross correlations. Therefore, the interference between echoes from different trips can be reduced. In general, after coherent processing, the interference from overlaid echoes appears like white noise.

- Multiple pulse-repetition-frequency methods or multiple pulse-repetition-time methods. These methods are also known as staggered PRF or staggered PRT methods. In these methods, pulses are transmitted with two or more different PRF's or PRT's. The estimates from each PRF or PRT can be combined or correlated to find the true mean frequencies of the signals. With staggered PRF or staggered PRT methods, the maximum unambiguous frequency of a radar system can be extended.

- Polarization coding from pulse to pulse and frequency hopping from pulse to pulse: Doviak and Sirmans [81] suggested an orthogonal polarization coding for successive pulses. In this method, two orthogonal polarizations are used for two successive pulses. Therefore, the overlaying between the radar echoes from the first trip and the second trip is reduced by the polarization of the antenna. However, the depolarization by hydrometeors and the radar system limits this method to about 20 dB of suppression of the interference. The frequency-hopping method was suggested by Doviak and Zrnic [44]. In that method, consecutive pulse pairs are transmitted at different frequency steps; therefore, the echoes from different pulse pairs can be separated by filters.

- Since the wind profiles are normally continuous in both frequency and space, the frequency ambiguities could be corrected by removing the discontinuities in the wind profiles. Such a method was demonstrated by Jiro [82].

The first three algorithms mentioned above are related to inter-pulse coding in either phase, polarization or pulse position. In this chapter, we will further discuss these methods, and compare their performance with computer simulations. Since the radar ambiguity function is a widely used tool for analyzing and studying the ambiguities of waveforms of radar signals [83], we will also discuss the algorithms for removal of radar ambiguities in term of their radar ambiguity functions. To compare the performances of different algorithms, Monte Carlo simulations were performed to calculate the second-order statistics of these algorithms. In addition, a new algorithm for reducing range and Doppler ambiguities using waveform modulation is discussed.

5.2 INTERPULSE PHASE CODING

In the following sections, we will examine the performance of different ambiguity-removal methods through the interpretations of their radar ambiguity functions. As we know, a radar ambiguity function can be used to show the properties of range resolution, frequency resolution, and the distribution of ambiguities for a particular waveform. We will correlate the radar ambiguity functions of the algorithms discussed in this chapter with their performance in estimating the mean frequencies. Before discussing the algorithms, we briefly review the properties of ambiguity functions. A detailed discussion on ambiguity functions of radar waveforms can be found in [82].

5.2.1 RADAR AMBIGUITY FUNCTIONS

The response function for a radar signal has two basic forms:

$$\chi_u(\tau, \phi) = \int_{-\infty}^{+\infty} u(t)\, u^*(t+\tau)\, e^{-j2\pi\phi t}\, dt \tag{5.1}$$

$$\chi_u(\tau, \phi) = \int_{-\infty}^{+\infty} U(f+\phi) U^*(f)\, e^{-j2\pi f\tau}\, df \tag{5.2}$$

where u(t) is the transmitted signal and U(f) is the Fourier transform of u(t). The response functions given in (5.1) and (5.2) were derived by using the definition of a matched filter and thus are sometimes called the matched-filter response functions. The ambiquity function is defined as $|\chi|^2$.

The function $\chi(\tau,\phi)$ for a fixed ϕ and a fixed τ describes the amplitude modulation of the signal at the output of a receiver filter from a target with a Doppler shift ϕ relative to the center frequency of the filter and a delay τ from the time to which the filter is matched. The response function can also be interpreted as the correlation between the transmitted complex waveform u(t) shifted by the Doppler frequency ϕ, $u(t)e^{-j\pi\phi t}$, and u(t) itself, where the shift $\phi=0$ occurs at time T_0. When $\phi=0$, the response function reduces to the autocorrelation function of the transmitted signal u(t). To avoid misinterpretation, hereafter in this chapter we refer to $|\chi|$ as the ambiguity function.

Several of the important properties of a radar signal can be determined from its ambiguity function. An ambiguity function has its peak value centered at the origin, indicating that the largest signal output occurs when a target has the range and velocity to which the filter is matched. In practice, being matched to a particular range and Doppler means that the filter is (1) sampled at the time corresponding to the round-trip delay of the transmitted signal to a target and (2) tuned in frequency to the Doppler shift corresponding to the radial velocity of the target.

Targets which appear at ranges and velocities such that $|\chi(\tau,\phi)|$ is about as large as $|\chi(0,0)|$ are indistinguishable to the radar. The width of the peak about (0,0) defines the resolution of the waveform. Other peaks away from (0,0) correspond to the ambiguities of the waveform. The minimum distance in the delay-time domain between the peaks other than the origin and the peak in the origin corresponds to the maximum unambiguous range; similarly, the minimum distance in the Doppler-frequency domain between the peaks other than the origin and the one in the origin corresponds to the maximum unambiguous frequency.

Ambiguity functions can also be used to study clutter rejection. Clutter can be described as any unwanted backscatter. Waveforms having $\chi(\tau,\phi) \simeq 0$ in the region of the $\tau\phi$ plane where clutter exists generally have good clutter-rejection properties. More precisely, the summation over the entire $\tau\phi$ plane of the product of $|\chi(\tau,\phi)|^2$ with the clutter distribution over the $\tau\phi$ plane determines the total interfering clutter signal. The energy of the clutter can be calculated from the following equation:

$$C = \iint_{-\infty}^{+\infty} p(\tau, \phi)\, \sigma(\tau, \phi)\, \left|\chi(\tau, \phi)\right|^2 d\tau\, d\phi \qquad (5.3)$$

where $\sigma(\tau,\phi)$ is the backscatter cross section of the clutter, and $p(\tau,\phi)$ is the density function of clutter. Notice the spreading loss factor $(4\pi)^3 R^4$ is omitted in the above equation.

A cross-ambiguity function describes the situationwhen the receiver filter is matched to a modulation v(t) which is different from the transmitted modulation u(t). The cross-ambiguity function is defined in the following forms:

$$\chi_{uv}(\tau, \phi) = \int_{-\infty}^{+\infty} u(t)\, v^*(t + \tau) e^{-j2\pi\phi\tau}\, dt \qquad (5.4)$$

or $$\chi_{uv}(\tau, \phi) = \int_{-\infty}^{+\infty} U(f+\phi)\, V^*(f)\, e^{-j2\pi f\tau}\, df \qquad (5.5)$$

A cross-ambiguity function can also indicate information about the range and frequency ambiguities as does an ambiguity function.

As examples of ambiguity functions, the following figures present two ambiguity functions: one is for a rectangular pulse:

$$u(t) = \frac{1}{\sqrt{\delta}} \mathrm{rect}\left(\frac{t}{\delta}\right) = \begin{cases} \frac{1}{\sqrt{\delta}} & |t| \leq \frac{\delta}{2} \\ 0 & \text{elsewhere} \end{cases}$$

where δ is the pulse width. The ambiguity function of u(t) is

$$\chi(\tau,\phi)=\begin{cases}\mathrm{rect}\left(\frac{\tau}{2\delta}\right)e^{j\pi\phi\tau}\frac{(\delta-|\tau|)}{\delta}\frac{\sin\pi\phi(\delta-|\tau|)}{\pi\phi(\delta-|\tau|)} \\ 0 \quad \text{when } |\tau|\geq\delta\end{cases} \tag{5.6}$$

The other example is a rectangular, linear FM pulse:

$$u(t)=\frac{1}{\sqrt{\delta}}\mathrm{rect}\left(\frac{t}{\delta}\right)e^{j\pi\alpha t^2}$$

The ambiguity function of above u(t) is

$$\chi(\tau,\phi)=\begin{cases}\mathrm{rect}\left(\frac{\tau}{2\delta}\right)e^{j\pi\phi\tau}\frac{(\delta-|\tau|)}{\delta}\frac{\sin\pi(\alpha\tau+\phi)(\delta-|\tau|)}{\pi(\alpha\tau+\phi)(\delta-|\tau|)} \\ 0 \quad \text{when } |\tau|\geq\delta\end{cases} \tag{5.7}$$

As we have mentioned, the ambiguity function represents the output of a matched filter. The Doppler frequency information is contained in the factor $e^{j\pi\phi\tau}$. These ambiguity functions are plotted in Figure 5.1. As indicated by equation (5.7), the peak of a signal with a Doppler shift ϕ_0 would also shift in time by amount $\tau_0=\phi_0/\alpha$. However, as α is usually very large, on the order of 10^{+12}, τ_0 would be very small in comparison to δ and can be ignored in most cases.

5.2.2 RANDOM-PHASE CODING

Random-phase coding is a method used for removing range ambiguities. A random-phase method was first applied in the RONSARD radar [84] using the random phase inherent in the magnetron transmitter. The phase coding was used to remove the bias in the estimate of the mean frequency due to overlying echoes by measuring the transmitted phases and using them to compensate for the phases of the received signals. At the receiver, only the echoes from the first trip were made coherent, and all the overlaid echoes from other trips were incoherent and appeared as increased white noise. Therefore, the bias in the estimate of mean frequency caused by interference could be reduced.

Laird suggested a phase-coding scheme in which the phase of the transmitted pulse is coded with binary random number 0 or π [85]. By employing a coherent reference, this scheme could re-cohere radar echoes from any particular trip and make the echoes from other trips appear like white noise. However, because the phase coding method only spreads the energy of interference echoes in the frequency domain, and does not reduce the total energy of the interference echoes, only one trip can provide a sufficiently large SNR for reliable measurement. As a result, the random phase coding method has limited use.

Therefore, the random phase-coding scheme cannot effectively recover the echoes from a trip if the energy of interfering echoes from other trips is strong. For this reason, Siggia developed an adaptive filter for processing the random phase coded radar signal [86]. The adaptive filter can reduce the effect of interfering echoes and increase the effective SNR. However, a significant improvement can be achieved only when the spectrum of the radar echo has a narrow width [87], and this method is computationally intense.

Computer simulations of ambiguity functions for three different phase-coded pulse trains were presented in Figures 5.2, 5.3 and 5.4. Figure 5.2 shows the ambiguity function of a uniformly spaced pulse train with no phase coding. As expected, the uncoded pulse train generates periodic range and frequency ambiguities. Figure 5.3 shows the ambiguity function of a uniformly spaced pulse train with random phase coding as used in [85]. We can see that the range ambiguities are reduced, the energy of interferences is distributed across the whole Nyquist interval and acts like white noise. However, the frequency ambiguities are unchanged. A similar statement can be applied to Figure 5.4, which shows the ambiguity function of a uniformly spaced pulse train modulated with a 13-bit long Barker-code.

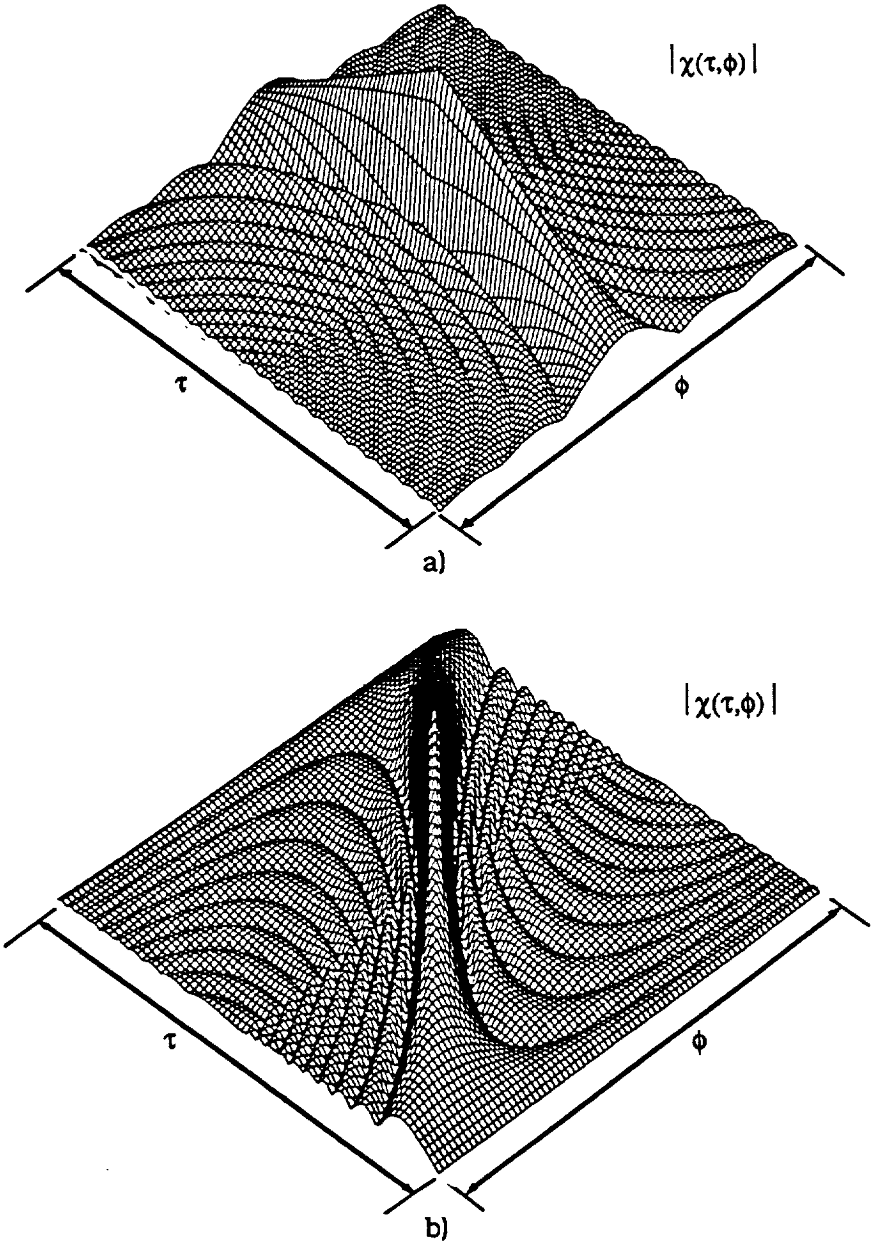

Figure 5.1. Examples of ambiguity function: a) ambiguity function for single rectangle pulse, b) ambiguity function for single linear FM modulated pulse. Absolute value shown for response function. Ambiguity function is square of response function, but contrasts are too great to show effectively on a 3-D graph. All other graphs in Chap. 5 labelled "ambiguity function" are actually response-function magnitudes.

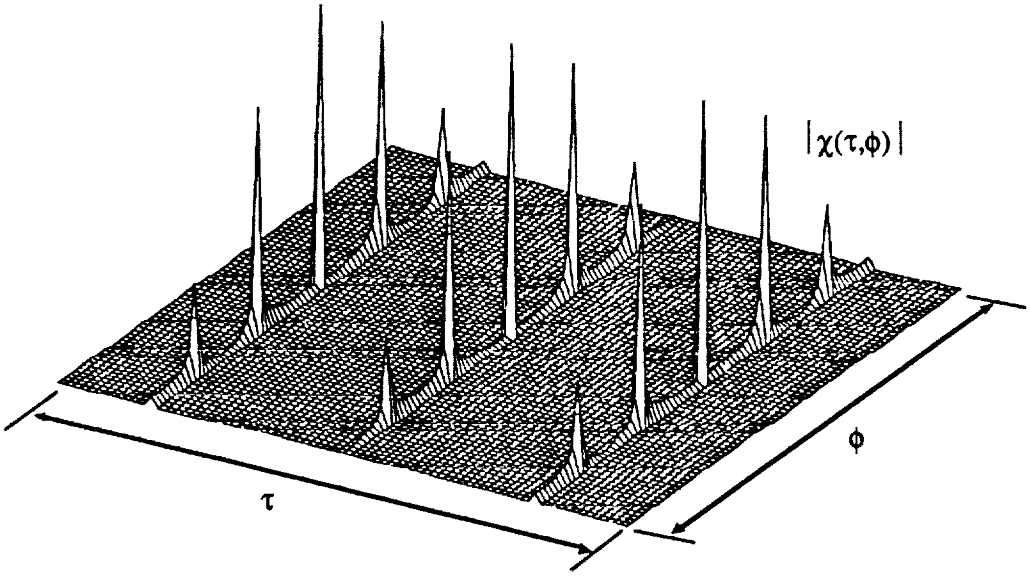

Figure 5.2 Ambiguity function of uniformly spaced pulses in which the pulse shape is Gaussian and total pulse number is 30.

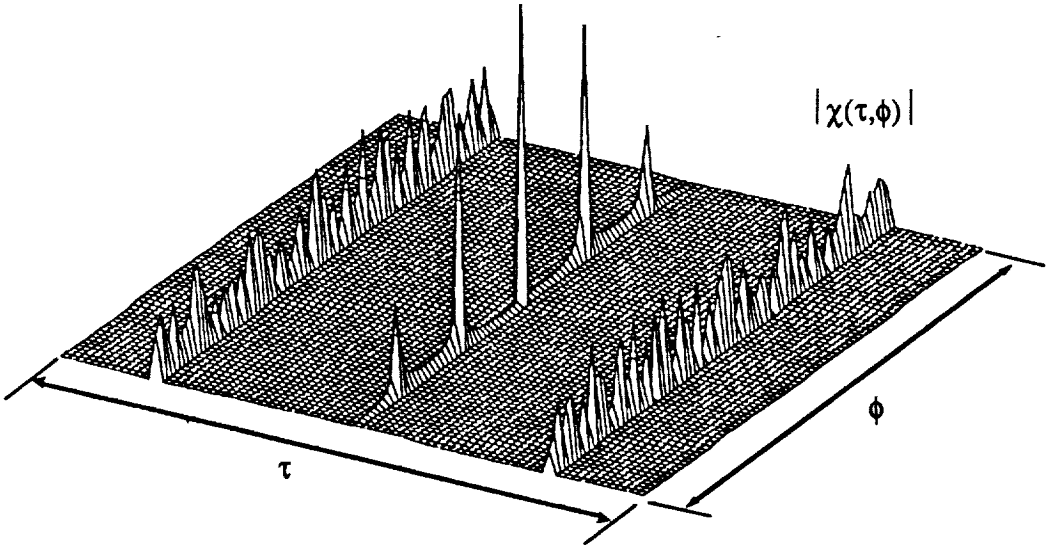

Figure 5.3. Ambiguity function of uniformly spaced pulses with random phase coding, the total pulse number is 30.

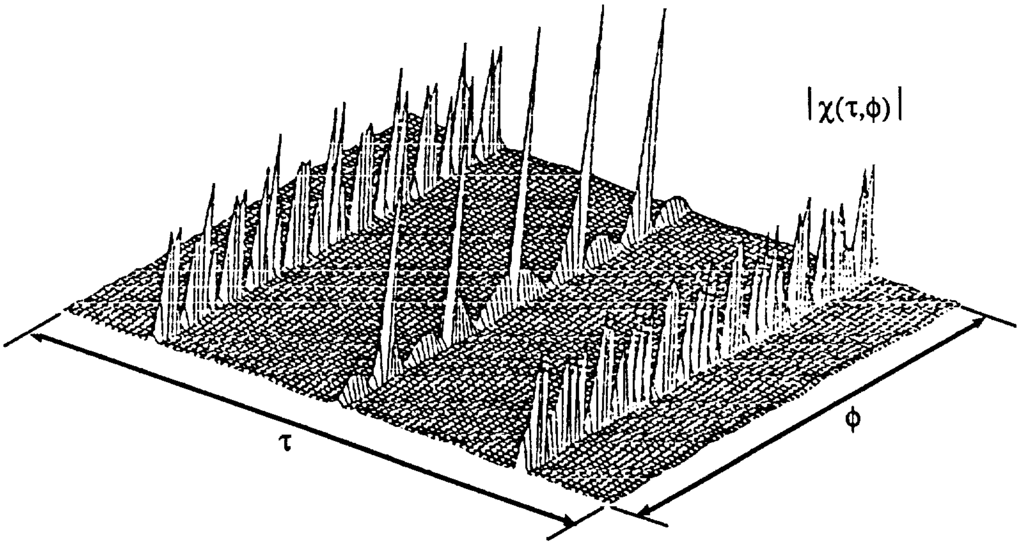

Figure 5.4. Ambiguity function of uniformly spaced pulses with Barker phase coding, the total pulse number is 13.

In summary, random phase-coding methods can be used to correlate signals returned from a specific trip and make the echoes from other trips appear like white noise. Thus, the frequency measured will not be greatly biased by the interference from other trips. Taking another point of view, the phase coding methods can be viewed as multiplying the transmitted pulses by a random signal sequence in the time domain; therefore, without a matched receiver, the spectrum of the received signal would look like white noise too.

However, the random phase coding does not reduce the total energy of the interference. Instead, it spreads out the spectrum of the interference over the entire Nyquist interval. Therefore, the interferences would act like white noise and deteriorate the SNR if proper filtering were not applied. Since only the signal returned from one particular trip would have large enough SNR (> 3 dB) for reliable estimate of the mean Doppler frequency, in practice the random phase-coding scheme may not be able to retrieve the mean frequency from echoes of an arbitrary trip.

5.2.3 DETERMINISTIC PHASE CODING

Zrnic and Mahapatra further studied the adaptive filter method discussed by Siggia for processing random phase-coded signals, and concluded that effective improvements in suppression of overlaid echoes are possible only when overlaid echoes have narrow spectral widths [87]. Sachidananda and Zrnic proposed an alternative phase coding method which can reduce the correlation of an overlying echo signal to zero at one-pulse lag [88]. With this phase coding, the covariance ("pulse-pair") estimator can give an unbiased estimate of mean frequency in presence of overlaid echoes from adjacent trips. The sequence of codes they suggested is $\pi/4, -\pi/4, \pi/4 \ldots$. At the receiver a sequence of $-\pi/4, 0, -\pi/4, \ldots$ is used to correlate the first trip echoes, and a sequence of $0, -\pi/4, 0, \ldots,$ is used to correlate the second trip echoes. This phase-coding scheme can make the autocorrelation functions of either the first trip echoes or the second trip echoes equal to zero. Therefore, the measurements of the mean frequency for either the first pulse or the second pulse are not affected by echo overlaying, provided that the overlaying of echoes is only due to two adjacent pulses.

The ambiguity function of a pulse train with such a coding scheme is shown on Figure 5.5. Figure 5.2 shows the ambiguity function of a corresponding pulse train without phase coding. One interesting point to note here is that one can arrive at a conclusion similar to that drawn from [88]. That is, all of the peaks of the range ambiguities from even trips are reduced to zero along the τ ($\phi=0$) axis. This is expected since the ambiguity function is reduced to the autocorrelation function along the τ axis. However, we also found that this scheme shifted the peaks of the ambiguities along the $\tau = \pm T, \pm 3T \ldots$ axes towards the τ axis for all of the even trips. This means that the unambiguous frequency for the second trip echoes are reduced to a smaller range.

From the above discussion, we can conclude that all the phase coding methods can be used to reduce the range ambiguity which results in flattening the peaks of the ambiguity function on the $\tau\phi$ plane. However, the distances between these peaks along the frequency axis is not changed by the phase coding methods.

As a result, the maximum unambiguous frequency remained unchanged. Therefore, phase coding is suitable for high PRF situations where the frequency ambiguity is not a problem.

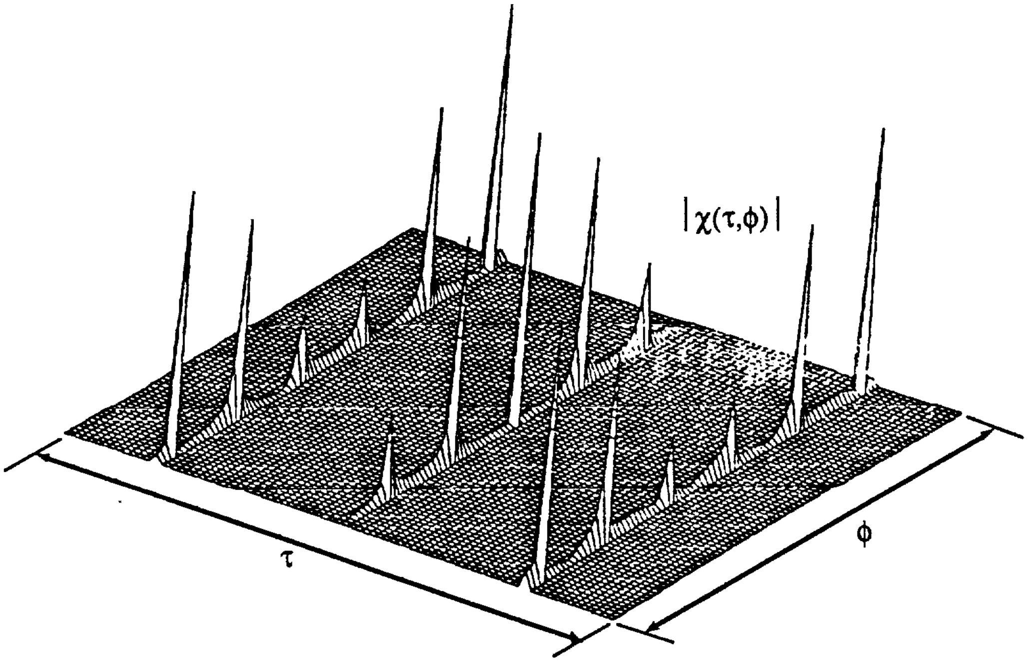

Figure 5.5. Ambiguity function for uniformly spaced pulses with $-\pi/4$, $\pi/4$, ..., $-\pi/4$, $\pi/4$ inter-pulse coding,the pulse shape is Gaussian, and total number of pulses is 30.

One other problem with the phase-coding methods is that the leakage from the transmitter may interfere with the receiver's operation if the isolation between the transmitter and receiver is not nearly perfect. This may be a serious problem for a chirp radar as an expanded pulse often lasts several tens of micro-seconds, and during the transmitting period the receiver cannot receive useful signals.

5.3 MULTIPLE PRF AND FREQUENCY AMBIGUITY REMOVAL

There have been many staggered PRF or PRT methods proposed for solving range and frequency ambiguities. Hennington (1981) suggested a method of transmitting a train of short pulses following by a long pulse to reduce the frequency ambiguity of the targets [89]. The long pulse was used to estimate the reflectivity of the targets; the short pulses were used to estimate the moments of the frequency spectrum. However, this scheme may not be applicable to a spread target. Sirmans et al suggested a staggered-prf method using two or more prfs to extend unambiguous frequencies [90]. Similar methods also were proposed by Sachidananda and Zrnic [88] and Ludloff and Minker [91]. In the remainder of this section, we will examine only two of these methods: the method discussed by Ludloff and Minker will be called "STAGGERED PRF METHOD-A," and the method discussed by Sachidananda and Zrnic will be called "STAGGERED PRF METHOD-B."

5.3.1 STAGGERED PRF METHOD — A

This algorithm was intended to be used in solving the blind speed problem of a MTD (moving target detector) radar [91], but it may also be applied to Doppler weather radar applications. The algorithm resolves the frequency ambiguity by illuminating a target with a set of pulse bursts with different PRF's F_k, where k=1,2,...,K. Let $\hat{f}_{0,k}$ be the measured Doppler frequencies associated with prf F_k. These measured frequencies may be different from the true frequencies because of frequency aliasing. However, for each prf F_k the true frequency can be found among the following $\hat{f}_{i,k}$ frequencies:

$$\hat{f}_{i,k} = \hat{f}_{0,k} + I_k F_k \qquad i=\ldots,\ -1,0,1,\ldots \tag{5.8}$$

To search for the true frequency, the algorithm systematically searches for those integers I_k that cause all estimates $\hat{f}_{i,k}$ with different k to fall within a small frequency interval or correlation bin. The average of the estimates provides an improved estimate $\hat{f}_T$ with reduced standard deviation

$$\hat{f}_T = \frac{1}{K}\sum_{k=1}^{K}(\hat{f}_{0,k} + I_k F_k) \tag{5.9}$$

and extended unambiguous frequency because $\hat{f}_T$ may be much larger than any F_k. From now on, let us consider the case that $K = 2$ with the stagger ratio

$$F_1 : F_2 = m : n$$

where m and n are relatively prime numbers and $m < n$ by definition. The expanded unambiguous frequency interval is

$$f_u = nF_1 = mF_2 \tag{5.10}$$

PROBABILITY OF FALSE CORRELATION

Although this algorithm reduces the standard deviations of the estimates of the mean frequency, it does introduce false correlation occasionally. The false correlations occur mainly at those locations where $f_{l,k}$ frequencies approach one another with the minimum possible distance d_{min} in frequency. There is a simple relationship between d_{min} and F_k given by [91]:

$$d_{min} = \frac{F_2}{n} = \frac{m}{n^2}F_1 \tag{5.11}$$

Let us assume the estimates are normally distributed. Then, if we define the difference between the two estimates as x, the probability density function for x has the following form :

$$p(x) = \frac{1}{\sqrt{2\pi(\sigma_1^2 + \sigma_2^2)}} \exp\left(- \frac{(x - \bar{x})^2}{2(\sigma_1^2 + \sigma_2^2)} \right) \tag{5.12}$$

where $\bar{x}$ is equal to 0 for a true frequency measurement and equal to d_{min} for false measurements. Since

$$\sigma_2^2 = \left(\frac{m}{n}\right)^2 \sigma_1^2$$

if we let $F_2 = 1$, the false measurement probability can be approximated as:

$$P((\hat{f} - f_T) > 0.5\, d_{min}) = 1 - \int_{-0.5/n}^{0.5/n} p(x)\, dx$$

$$= 1 - \int_{-0.5/n}^{0.5/n} \frac{1}{\sigma_1 \sqrt{2\pi(1 + (m/n)^2)}} \exp\left(- \frac{x^2}{2\sigma_1^2((m/n)^2 + 1)} \right) dx \tag{5.13}$$

Here, σ_1 is approximately a linear function of the spectral width of the signal. As a result, when the standard deviation of the power spectral density increases, the probability of false measurement also increases as shown in Figure 5.6. It also can be observed that the difference between the false measurement and the true frequency is usually one or more Nyquist intervals. Thus, it is possible to correct these false estimates by continuity or the method we are going to discuss in the next section. The $f_{i,k}$ can be estimated with the FFT method, the AR method, or the covariance method.

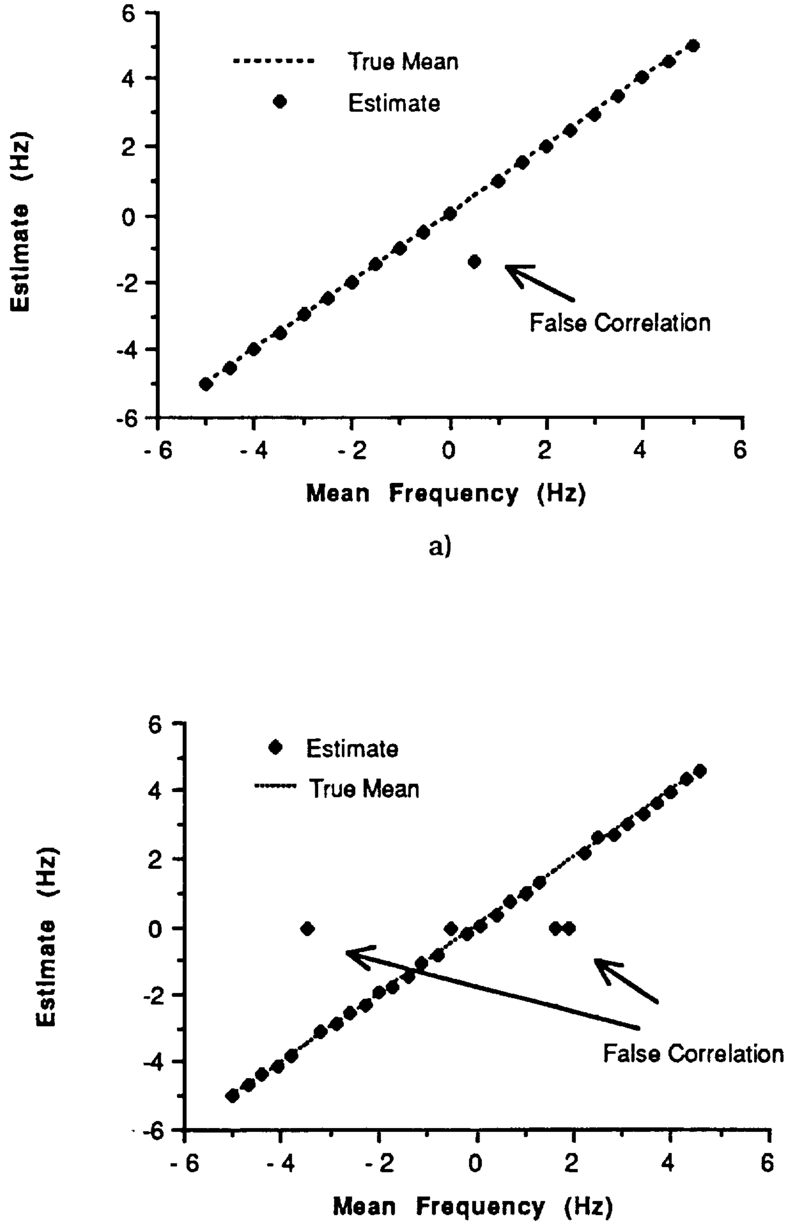

a)

b)

Figure 5.6. Simulation of STAGGERED PRF-A method, a) $\sigma = 0.1$, SNR = 0 dB, b) $\sigma = 0.3$, SNR = 0 dB. Normalized frequencies are shown.

5.3.2 STAGGERED PRF METHOD - B

This staggered PRT method was described by Zrnic and Mahapatra [87]. In this scheme, the pulses are transmitted alternatively with two different pulse repetition intervals, T_1 and T_2. The frequency estimate is determined by a formula derived from the covariance method:

$$f_T = \frac{1}{\pi(T_2 - T_1)} \arg\left(\frac{R(T_2)}{R(T_1)}\right)$$

$$= \frac{1}{\pi T_2(1 - K)} \arg\left(\frac{R(T_2)}{R(T_1)}\right) \tag{5.14}$$

where R(t) is the autocorrelation function of the radar echoes, and K is a constant equal to T_1/T_2. The maximum unambiguous velocity depends on the difference of T_1 and T_2, and is equal to:

$$f_{max} = \frac{1}{\pi(T_2 - T_1)} \tag{5.15}$$

The variance of this estimator can be derived from (5.14),

$$VAR(\hat{f}) = \frac{1}{\pi(T_2 - T_1)} VAR(\theta_1 - \theta_2) \tag{5.16}$$

where θ_1 and θ_2 are equal to $\arg(R(T_1))$ and $\arg(R(T_2))$. A more detailed analysis can be found in [87]. From this equation, we can observe that the standard deviation of the estimate increases as the difference between T_1 and T_2 decreases. The results of a computer simulation are presented in Figure 5.7. These results indicate that the A method is superior to the B method in terms of RMS errors; however the B method does not give false estimates (individually big errors).

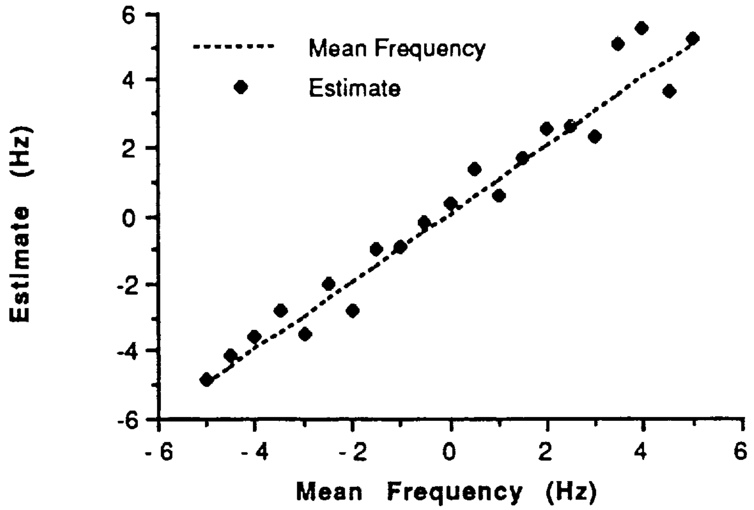

Figure 5.7. Simulation of STAGGERED PRF-B method with T_1/T_2 = 0.875, σ=0.3, SNR = 0 dB. Normalized frequency is shown.

5.3.3 RANDOM PULSE POSITION CODING

The multiple PRT methods discussed above can be classified as special cases of random pulse position coding. The general pulse train with pulse-position coding and phase coding can be expressed as:

$$y(t) = \sum_{n=0}^{N-1} u(t - nT_0 - \Delta_n)\, e^{j\phi_n(t-nT-\Delta_n)} \quad (5.17)$$

where Δ_n is the displacement from nT_0 and ϕ_n represents the phase coding. The form of the ambiguity function for equation (5.17) and the properties of the ambiguity function of the position coding were reported in [92]. We will not proceed further on this topic.

5.4 WAVEFORM MODULATION AND AMBIGUITY REMOVAL

5.4.1 WAVEFORM MODULATION REDUCES RANGE AMBIGUITY

The current algorithms developed for removal of range and frequency ambiguities are primarily involved with inter-pulse coding in either phase or time. In this section, we will discuss the utilization of waveform modulation on transmitted pulses to reduce range ambiguities. Furthermore, as shown later, waveform modulation can be combined with the covariance method discussed in Chapter 4 to solve the frequency-ambiguity problem.

Waveform design has found many applications in radar and communication systems. In radar systems, waveform design is often related to clutter rejection and pulse compression. In communication systems, it is used in the area of spread spectrum communications for code multiplexing [93 - 94].

The basic concept of waveform modulation for range-ambiguity reduction can be illustrated in an example from code multiplexing in a communication system. Waveform modulation allows two different signals to be transmitted in the same bandwidth and time interval, and at the receiver, the two signals can be separated by the process of correlation detection. This can be shown mathematically: assume $s_1(t)$ and $s_2(t)$ are two different waveforms(or codes), and $s_1(t) + s_2(t)$ is the receiver input. For receiving signal $s_1(t)$, a reference signal $s_1(t)$ is used at the receiver to correlate with the input signal. Let T be the signal integration time, and the correlator's output may be expressed as:

$$y(t) = \frac{1}{T}\int_0^T (s_1(t) + s_2(t))s_1(t)\,dt$$

$$= \frac{1}{T}\int_0^T s_1^2(t)\,dt + \frac{1}{T}\int_0^T s_1(t)s_2(t)\,dt \qquad (5.18)$$

The first term in (5.18) is the signal output and the second term represents interference from $s_2(t)$. The interference level is therefore determined by the cross correlation of $s_1(t)$ and $s_2(t)$. The usefulness of such a system is determined by the cross correlation of the codes used. There are various coding techniques, such as Barker codes, m-sequence, and random phase-coding. Most of these codes are able to keep the sidelobe at the level of 1/N of the main lobe, with N is the total length of a code [94].

Instead of using discrete coding (mostly binary), we may consider using continuous waveform modulations. The main task is to find a set of continuous waveforms with low cross correlations and study the effective SNR at the receiver. One such candidate is linear frequency modulation (FM), also known as chirp. For example, two pulses modulated with different linear-FM waveforms may have low cross correlation. To simplify the following discussion, we consider waveforms having the same time intervals and bandwidths. There may be many other linear or non-linear FM waveforms with low cross correlations. However, the discussion of those waveforms is beyond the scope of this study.

Assume two Gaussian pulses u(t) and v(t) are modulated with conjugate linear FM, namely the first pulse in the pair is modulated with up chirp and the second with down chirp:

$$u(t) = (2a)^{1/4}\, e^{-\pi a t^2 + j\pi\alpha t^2} \qquad (5.19)$$

$$v(t) = (2a)^{1/4}\, e^{-\pi a t^2 - j\pi\alpha t^2} \qquad (5.20)$$

where $(2a)^{1/4}$ is a constant to normalize the maximum value of the ambiguity function to 1. The second assumption made is that the pulses are transmitted in pairs spaced by a time interval T_2. The transmitted pulse-pair train is expressed as

$$y(t) = \sum_{n=0}^{N-1} u(t - nT_1) + v(t - nT_1 - T_2) \qquad (5.21).$$

At the receiver, there are two channels. One is matched to the signal u(t) and the other is matched to v(t) as shown in Figure 5.8. The output from channel I and channel II are given as correlations between the received signals and the impulse response of the matched filter.

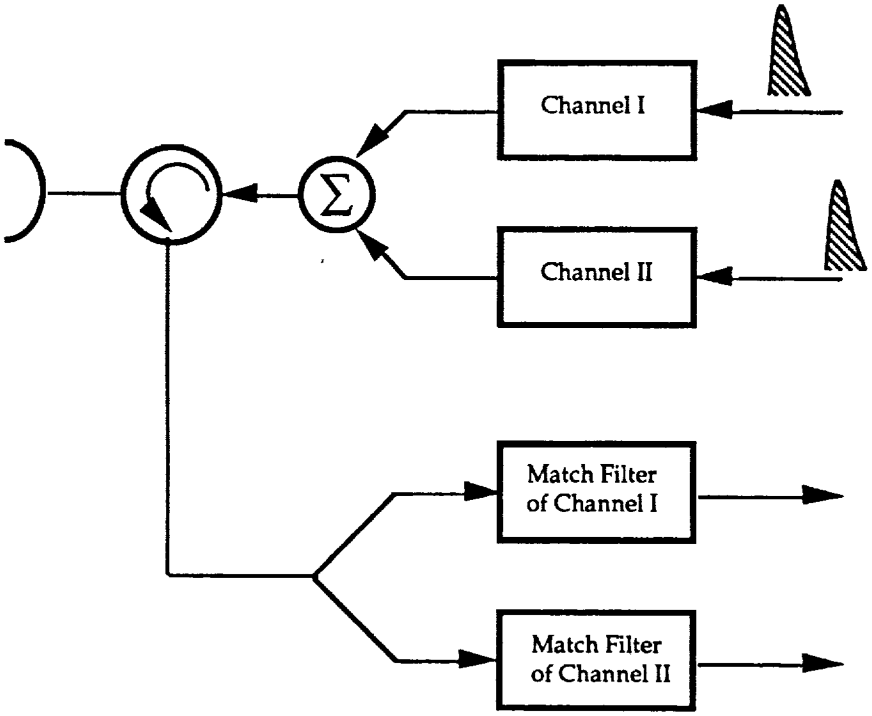

Figure 5.8. Configuration of dual-modulation receiver.

To examine the output of each matched filter, we need to calculate the ambiguity function and cross-ambiguity functions of the waveforms represented by (5.21). In fact, the cross-ambiguity functions are the outputs of the matched filters. The ambiguity function of such a pulse train can be calculated from the following integral:

$$\chi_u(\tau,\phi) = \int_{-\infty}^{+\infty} y(t)y^*(t+\tau)\,dt$$

$$= \chi_{\Sigma u}(\tau,\phi) + \chi_{\Sigma v}(\tau,\phi)\, e^{-j2\pi\phi T_2} + \chi_{\Sigma uv}(\tau - T_2,\phi)$$

$$+ \chi_{\Sigma vu}(\tau + T_2,\phi)\, e^{-j2\pi\phi T_2} \qquad (5.22)$$

The analytical forms of $\chi_{\Sigma u}$, $\chi_{\Sigma uv}$, $\chi_{\Sigma v}$ and $\chi_{\Sigma vu}$ are listed below. A detailed derivation of these functions is included in Appendix 5.A.

$$\chi_{\Sigma u}(\tau,\phi) = \begin{cases} \displaystyle\sum_{m=-(N-1)}^{N-1} e^{-j\pi(N-1-m)\phi T_0}\chi_u(\tau-mT_0,\phi)\frac{\sin((N-m)T_0\pi\phi)}{\sin(\pi T_0\phi)} \\ \text{when } |\tau-mT_0| \le \delta \\ 0 \qquad \text{elsewhere} \end{cases}$$

$$\chi_{\Sigma v}(\tau,\phi) = \begin{cases} \displaystyle\sum_{m=-(N-1)}^{N-1} e^{-j\pi(N-1-m)\phi T_0}\chi_v(\tau-mT_0,\phi)\frac{\sin((N-m)T_0\pi\phi)}{\sin(\pi T_0\phi)} \\ \text{when } |\tau-mT_0| \le \delta \\ 0 \qquad \text{elsewhere} \end{cases}$$

$$\chi_{\Sigma vu}(\tau,\phi) = \begin{cases} \displaystyle\sum_{m=-(N-1)}^{N-1} e^{-j\pi(N-1-m)\phi T_0} \chi_{vu}(\tau - mT_0, \phi) \frac{\sin((N-m)T_0\pi\phi)}{\sin(\pi T_0\phi)} \\ \text{when } \left| \tau - mT_0 \right| \le \delta \\ \\ 0 \qquad \text{elsewhere} \end{cases}$$

$$\chi_{\Sigma uv}(\tau,\phi) = \begin{cases} \displaystyle\sum_{m=-(N-1)}^{N-1} e^{-j\pi(N-1-m)\phi T_0} \chi_{uv}(\tau - mT_0, \phi) \frac{\sin((N-m)T_0\pi\phi)}{\sin(\pi T_0\phi)} \\ \text{when } \left| \tau - mT_0 \right| \le \delta \\ \\ 0 \qquad \text{elsewhere} \end{cases}$$

Also from appendix 5.A we obtain

$$\chi_u(\tau,\phi) = e^{j\pi\tau\phi}\, e^{-\pi/2\left(a\tau^2 + \frac{(\alpha\tau+\phi)^2}{a}\right)} \tag{5.23}$$

$$\chi_v(\tau,\phi) = e^{j\pi\tau\phi}\, e^{-\pi/2\left(a\tau^2 + \frac{(\alpha\tau-\phi)^2}{a}\right)} \tag{5.24}$$

$$\chi_{uv}(\tau,\phi) = \sqrt{\frac{a}{a - j\alpha}}\, e^{-\frac{\pi}{2}(-a\tau^2 + \frac{a\phi^2}{a^2 + \alpha^2})}\, e^{-j\frac{\pi}{2}(-\alpha\iota^2 - 2\phi\tau + \frac{\alpha\phi^2}{a^2 + \alpha^2})} \tag{5.25}$$

$$\chi_{uv}(\tau,\phi) = \sqrt{\frac{a}{a + j\alpha}}\, e^{-\frac{\pi}{2}(-a\tau^2 + \frac{a\phi^2}{a^2 + \alpha^2})}\, e^{j\frac{\pi}{2}(-\alpha t^2 + 2\phi\tau + \frac{\alpha\phi^2}{a^2 + \alpha^2})} \qquad (5.26)$$

The outputs from channel I and II are the cross correlations:

$$\text{channel I:} \quad \chi_{\Sigma u}(\tau,\phi) + \chi_{\Sigma uv}(\tau - T_2,\phi) \qquad (5.27)$$

$$\text{channel II:} \quad \chi_{\Sigma v}(\tau,\phi) + \chi_{\Sigma vu}(\tau + T_2,\phi) \qquad (5.28)$$

In equations (5.27) and (5.28), the first terms represent the signal outputs from the matched filters and the second terms represent interference. The ambiguity functions and cross-ambiguity functions given in equation (5.27) and (5.28) are plotted in 3D drawings in Figures 5.9 and 5.10. It can be observed that the energy levels of the interference at each channel are much lower than that of the main lobe. In fact, it can be shown that the interference levels are approximately equal to the inverse of the time-bandwidth (BT) products of the waveforms.

For a single target, the effective ratio of signal and interference can be calculated by the following equation:

$$\left| \frac{\chi_{\Sigma u}(0,0)}{\chi_{\Sigma uv}(0,0)} \right|^2 = \sqrt{\frac{a^2 + \alpha^2}{a^2}} \qquad (5.29)$$

We are going to prove that the above expression is equal to the time bandwidth product of a pulse. Let the chirped pulse width be δ. The bandwidth then is approximately equal to $\alpha\delta$, and the time bandwidth product, BT, is equal to

$$BT = \delta\, \alpha\delta$$

The parameter a and the pulse width δ are related as follows

$$a \simeq \frac{1}{\delta^2}$$

If we substitute these equations into (5.29), the effective signal to interference ratio becomes

$$\sqrt{\frac{a^2 + \alpha^2}{a^2}} = \sqrt{1 + (BT)^2} \simeq BT$$

(5.30)

Equation (5.30) above shows that the effective SNR for a single target is determined by the time bandwidth product of the FM modulated signal. By choosing large time bandwidth products for the transmitted pulses, we can reduce the interference level to an arbitrarily small value.

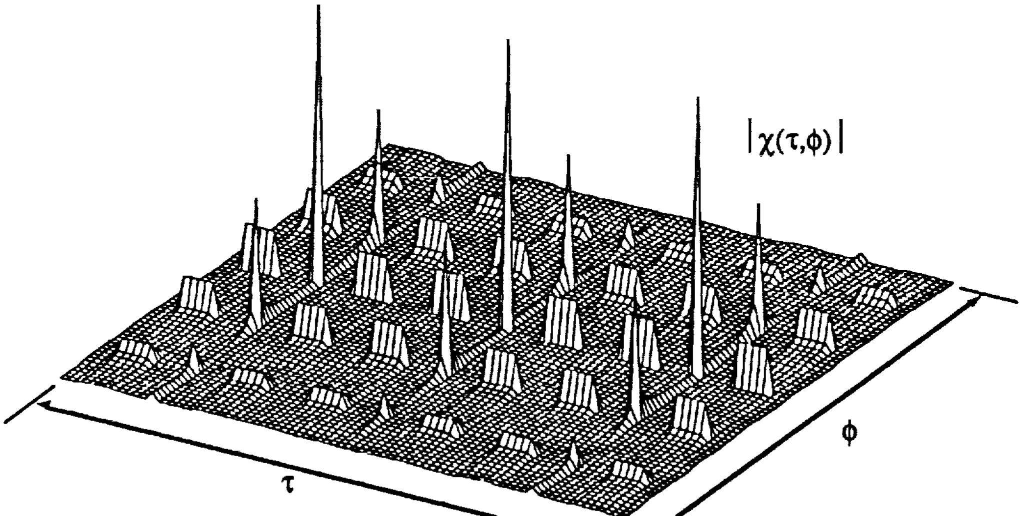

Figure 5.9. Ambiguity function of dual linear FM modulated pulse train. $T_2 = 0.3\,T_1$, time bandwidth product = 10.0

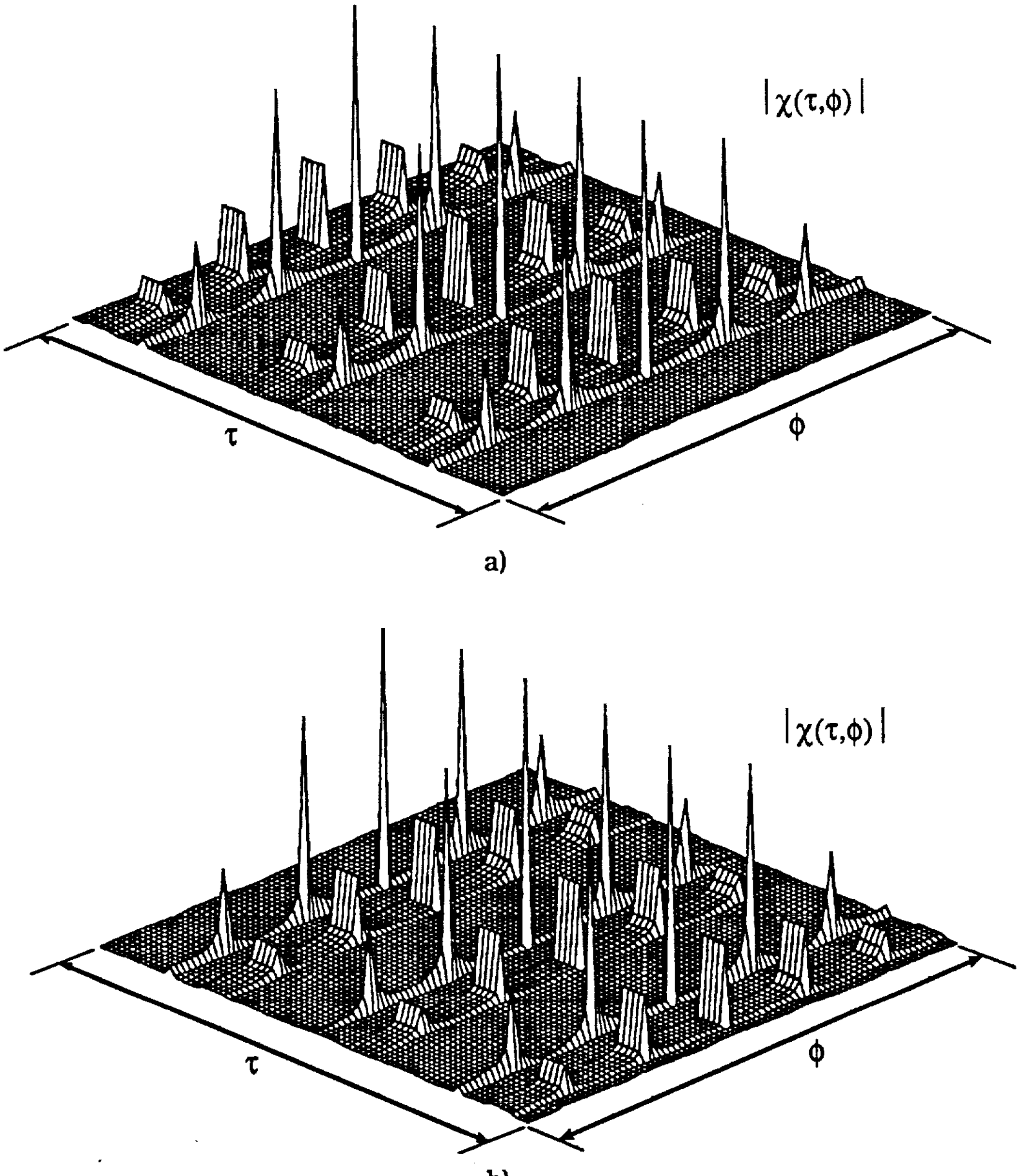

a)

b)

Figure 5.10. Cross ambiguity functions, a) as an output of channel I, b) as an output of channel II.

However, in weather radar the target is always spread. The above calculation of effective SNR cannot be used for a spread target. The interference can be calculated from equation (5.3). However, from observing the plot in Figure 5.10, the domain of integration can be simplified to the area represented by the product of the time duration $(T_2-\delta, T_2+\delta)$ and frequency interval $(-\infty, +\infty)$ Since echoes only from this area can contribute to the interference. Denote C as the voltage output of the total interference, it can be shown that (Appendix 5.A):

$$C = \int_{T_2-\delta}^{T_2+\delta} \int_{-\infty}^{+\infty} \chi_{uv}(\tau - T_2, \phi)\, d\tau d\phi$$

$$= \sqrt{\frac{2a}{a-j\alpha}} \tag{5.31}$$

Therefore, the effective signal to interference ratio is equal to

$$\frac{S}{C^2} = \frac{|\chi(0,0)|^2}{C^2} = \frac{\sqrt{a^2+\alpha^2}}{2a} \simeq \frac{BT}{2} \tag{5.32}$$

In calculating the spread target interference, we made the assumption that the refelectivity of the distributed target in the integral domain is constant.

5.4.2 AN APPLICATION

a) In the waveform discussed in the previous section, each pulse in a pulse-pair is transmitted with the same carrier frequency, same bandwidth, and same envelope but opposite slopes of linear FM. Because the two pulses are transmitted with the same carrier frequency, the coherency of the returned signals from the two pulses in a pulse-pair is guaranteed if these signals are returned from the same resolution volume. The covariance method can be used to estimate the mean frequency from each pulse-pair. As discussed in chapter 4, the covariance method does not depend upon the inter-spacing between two adjacent pulse pairs.

Since the maximum unambiguous frequency only depends upon the length of T_2 and the maximum unambiguous range only depends upon the length of $T_1 + T_2$, the lengths of T_1 and T_2 can be adjusted to achieve a desired unambiguous frequency and range. Although the plot of the ambiguity function shows that this scheme cannot remove the peaks of the frequency ambiguities, we can still use this scheme to get the correct mean frequency of the spectrum. As the two pulses in one pulse pair are in the same bandwidth and have the same carrier frequency, the echoes from the two pulses can be coherent if the transmitted pulses are coherent.

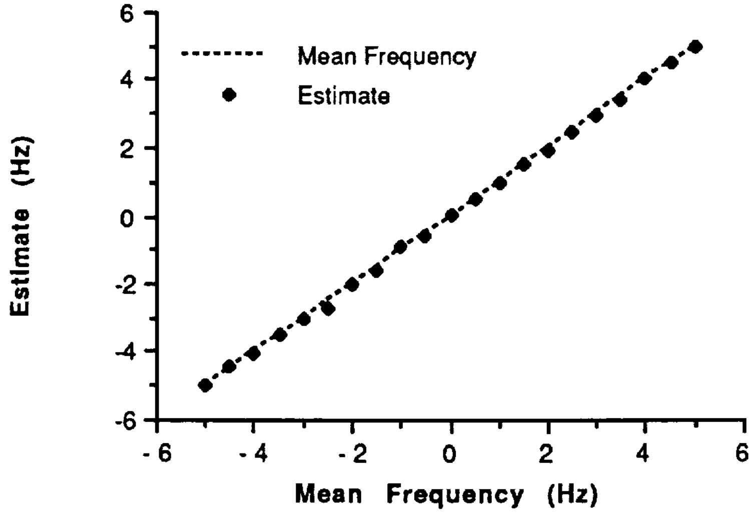

Figure 5.11. Simulation of waveform modulation method for estimating first moment with extended frequency range, with one run, σ=0.3, SNR=10 dB.

In summary, the waveform modulation allows us to achieve high signal to interference ratios and to obtain coherence between the pulses. The radar echoes from the two pulses in a pulse-pair are separated through two matched filters. The frequency ambiguity is reduced by the pulse pair method with two PRTs (T_1 and T_2). A computer simulation of this algorithm is presented in Figure 5.11 (with measurements as a function of mean frequency). This figure shows that the waveform modulation method produces smaller errors in estimation than the STAGGER-B method.

STAGGER-B method.

b) Furthermore, we can combine a) with the inter-pulse coding method. For example, we can code the pulse train with a random binary phase coding: each pulse pair is multiplied by a random binary phase either 0 or π. One such an example is given in Figure 5.12. By comparing Figure 5.12 and Figure 5.9, we can see that the peaks of the range ambiguities are further reduced by the random phase coding. More important is the fact that the spectrum of the interference is flattened. This can reduce bias in our estimate of the mean frequency. However, one needs to notice that the effective signal-to-interference ratio is not being reduced by the random phase coding, only the spectrum of the interference is flattened.

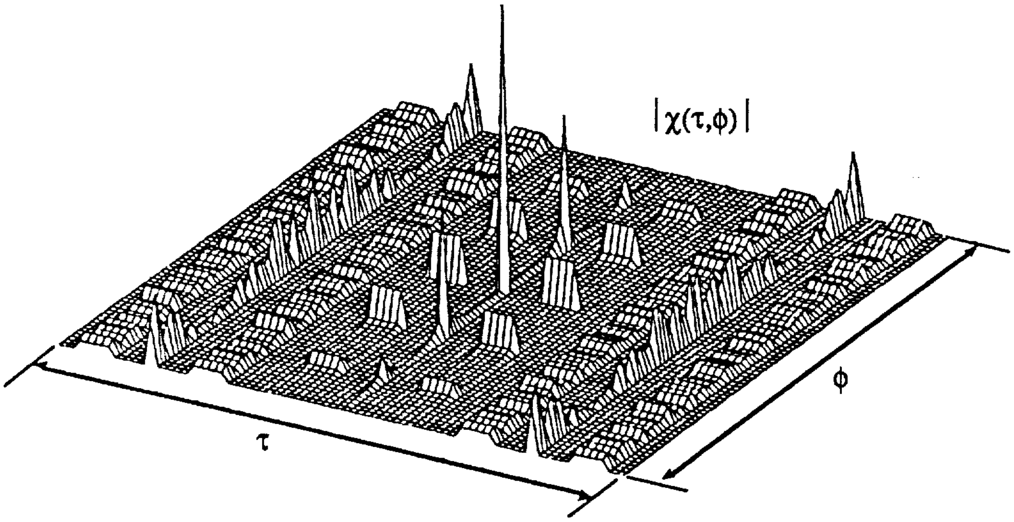

Figure 5.12. Ambiguity function for the same pulse train as in Figure 5.10, except random phase coding was applied.

5.5 RESULTS AND CONCLUSIONS

5.5.1 THE SIMULATOR

Two simulators were used in this chapter. One simulator written in C language was used to study the ambiguity functions for the different algorithms discussed This simulator allows the user to specify parameters such as the pulse length, pulse repetition time (PRT), type of inter-pulse coding, and number of pulses in the pulse train, etc. The resulting ambiguity functions are plotted with 3-D hidden-line drawings on the computer screen. The second simulator is similar to the one used in Chapter 4. This simulator is used for Monte Carlo simulations of the algorithms discussed in this chapter, with specified parameters such as SNR, number of runs, spectral width of the signals, etc.

5.5.2 MONTE CARLO SIMULATION

Monte Carlo simulations have been used to compare the performance of the three algorithms discussed in this chapter: STAGGERED PRF-A, STAGGERED PRF-B and waveform modulation methods. As in Chapter 4, the results are presented with RMS errors as functions of SNR, spectral widths of the signals, and mean frequencies of the signals.

The data used in the simulations were generated with Gaussian shaped spectral density functions with different SNRs and spectral widths. In the simulations of the staggered PRF-A method, two different PRF's were used with a ratio of F_1:F_2=7:8. In the simulations of staggered PRF-B method, two PRT's were chosen with the ratio of T_2:T_1=7:8. In the simulations of the waveform-modulation method, the ratio of inter-spacing of the two pulses in a pulse pair and the spacing between pulse-pairs is chosen to be 1:7. All the three estimators should have unambiguous frequency ranges as large as seven times the Nyquist interval.

All the computer simulations are based on the normalized Nyquist frequency interval defined as [-1,1]. The mean frequencies of the input data change from -5 to 5 with specified steps. This frequency range is 5 times the Nyquist frequency. Figures 5.14 to 5.16 illustrate the Monte Carlo simulations of the RMS errors as functions of the SNR and mean frequency. Figures 5.17 to 5.19 show the Monte Carlo simulations of the RMS errors as functions of spectral widths of the input data and SNRs. From these results, we can draw the conclusion that the STAGGERED PRF-A method produces the smallest RMS errors, followed by the waveform-modulation method. The STAGGERED PRF-B method produces RMS errors which are approximately an order of magnitude larger than those of the STAGGERED PRF-A method.

However, the STAGGERED PRF-A method is not without its disadvantages. When the spectral width of the signal is large compared with the Nyquist frequency ($\sigma/f_N > 0.3$), the STAGGERED PRF-A method produces a significant number of false correlations as shown in Figure 5.16a. The RMS errors produced by the waveform-modulation method do not change very much as the spectral width of the data changes.

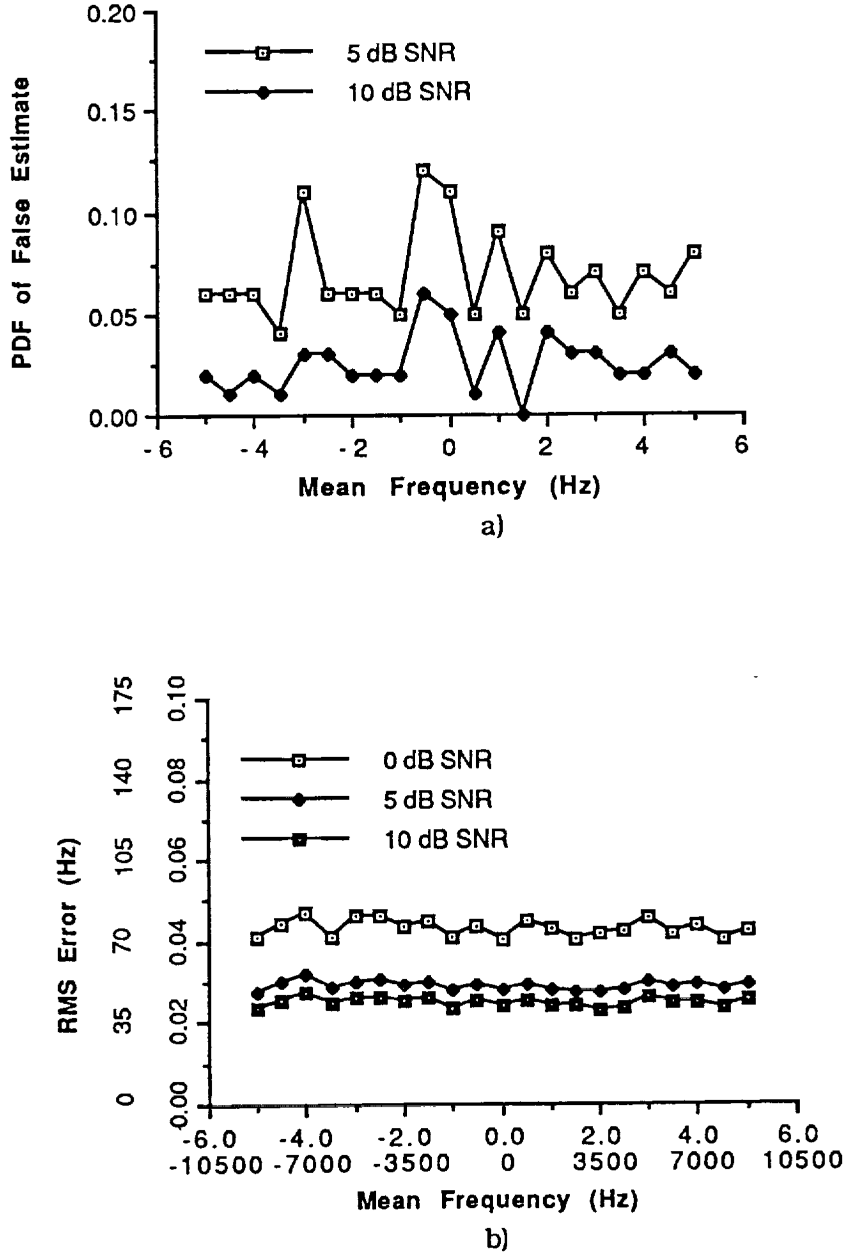

a)

b)

Figure 5.13. Monte Carlo simulation of STAGGERED PRF-A method with 100 runs, $\sigma=0.3$, number of pulse pairs = 128; a) probability of false estimate; b) RMS error as a function of frequency and SNR.

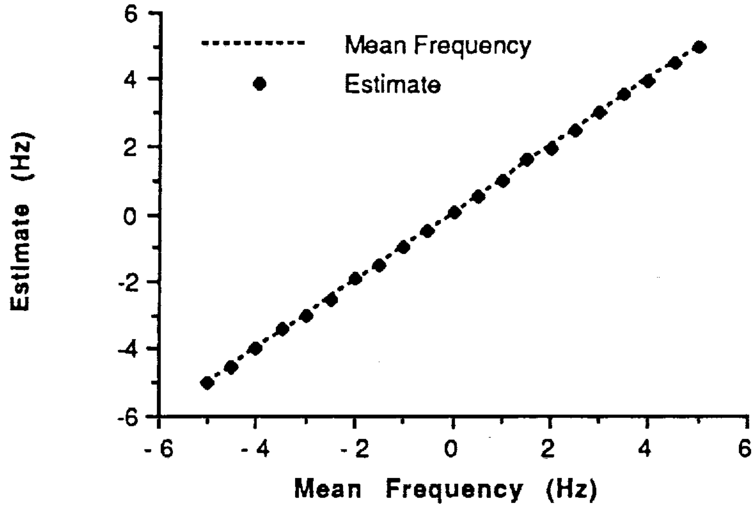

a)

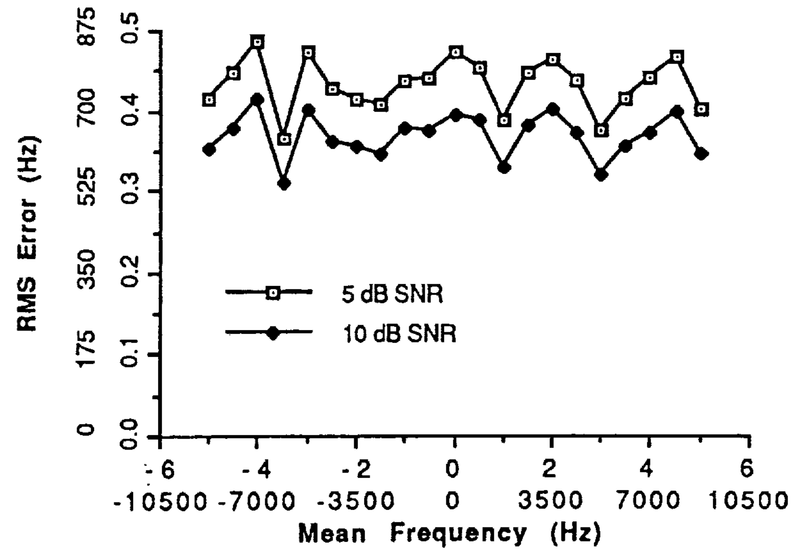

b)

Figure 5.14. Monte Carlo simulation of STAGGERED PRF-B method with 100 runs, $\sigma=0.3$, number of pulse pairs = 128; a) ensemble average of estimates; b) RMS error as a function of frequency and SNR.

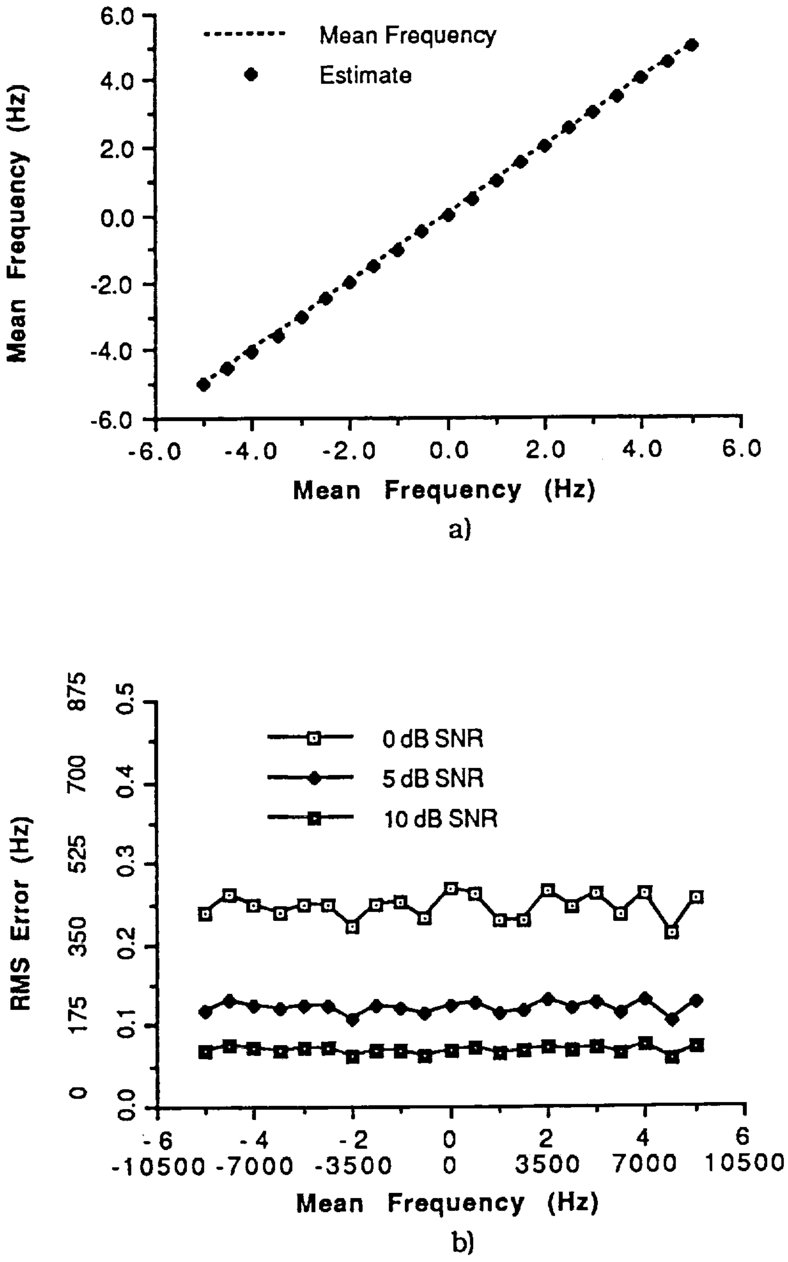

Figure 5.15. Monte Carlo simulation of WAVEFORM MODULATION method with 100 runs, $\sigma=0.3$, number of pulse pairs = 128; a) ensemble average of estimates; b) RMS error as a function of frequency and SNR.

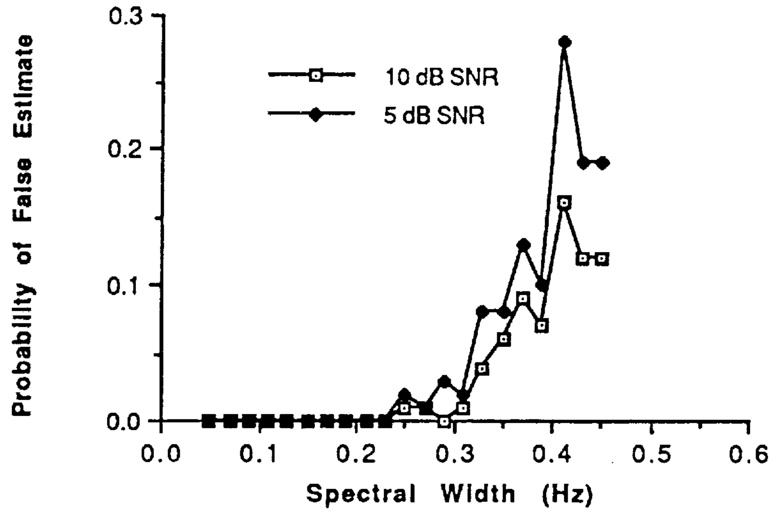

a)

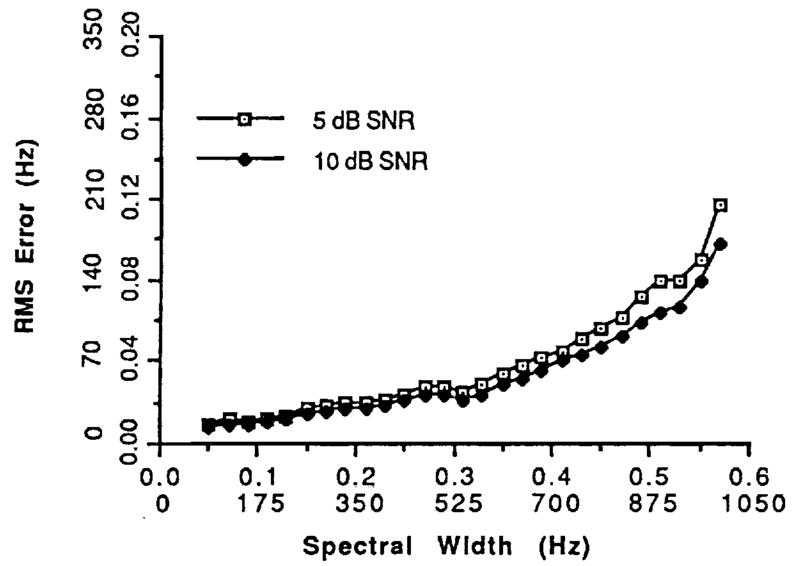

b)

Figure 5.16. Monte Carlo simulation of STAGGERED PRF-A method with RMS error and probability of false estimate as function of spectral width of the signal and SNR, 100 runs, number of pulse pairs = 128; a) plot of the probability of false estimate; b) plot of RMS errors.

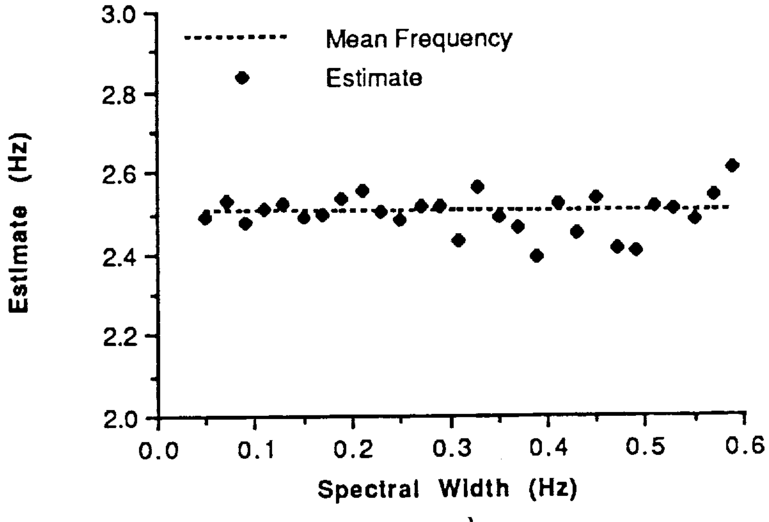

a)

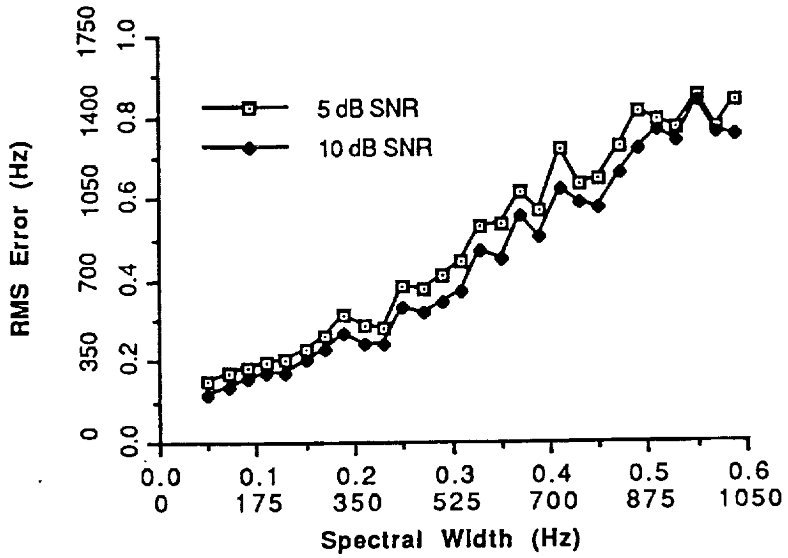

b)

Figure 5.17. Monte Carlo simulation of STAGGERED PRF-B method with 100 runs, number of pulse pairs = 128; a) plot of the ensemble average of estimates; b) plot of RMS errors as a function of spectral width of input signal.

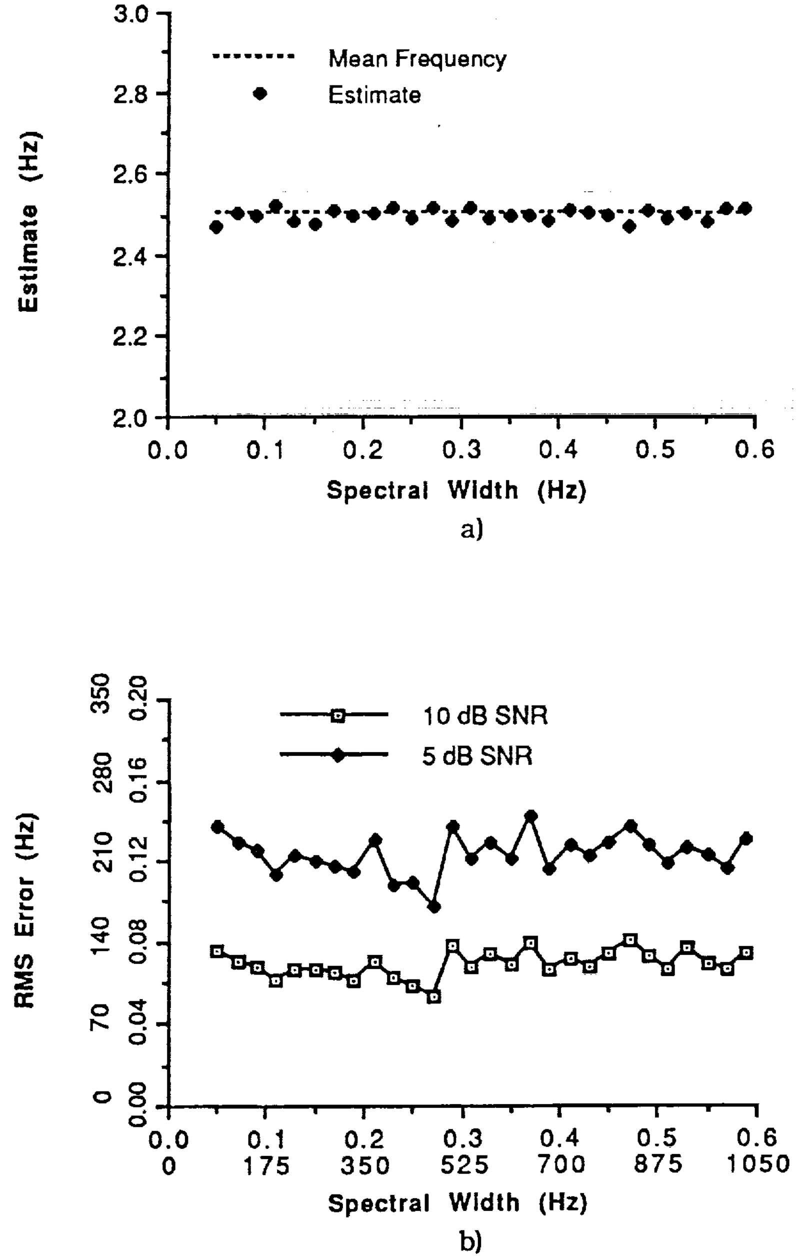

Figure 5.18. Monte Carlo simulation of WAVEFORM MODULATION method with 100 runs, number of pulse pairs = 128; a) plot of the ensemble average of estimates; b) plot of RMS errors as a function of spectral width of input signal.

5.5.3 CONCLUSION

Among the algorithms discussed in this chapter, the staggered PRF-A produces the smallest RMS errors of these three algorithms when the spectral width is less than 0.3. The staggered PRF-B method produces the largest RMS errors among these algorithms. For all these algorithms, the RMS errors increased as the SNRs decreased. For the staggered PRF-A and PRF-B methods, the RMS errors also increased as the spectral widths increased. In the computer simulation, for the waveform modulation method, the RMS errors did not change very much as the the spectral widths of the radar signals increased.

In the RAWS system, the spectral widths of the radar echoes are about half of the Nyquist interval. In such a case, the PRF-A method has very large probability of false measurements, about 20% at 10 dB SNR and 30% at 5 dB SNR. The RMS errors produced by the waveform modulation are about 7% of the Nyquist interval at 10 dB SNR, and about 12% at 5 dB SNR. The staggered PRF-B method generates too large RMS errors to be used in this system. Assume that the PRF is 3500 Hz. Then the Nyquist interval is 1750 Hz. Therefore, the waveform modulation method will generate about 122 Hz RMS errors in the estimates of mean frequencies at 10 dB SNR, and about 210 Hz at 5 dB SNR.

APPENDIX 5.A AMBIGUITY FUNCTION FOR WAVEFORM MODULATION

To derive the ambiguity function for the waveform modulation method, we first need to review some basic formulas often used in deriving ambiguity functions and the ambiguity functions for some simple waveforms and pulse trains.

BASIC FORMULAS

$$\int_{-\infty}^{+\infty} e^{-st^2}\, dt = \sqrt{\frac{\pi}{s}} \tag{5.33}$$

$$F(e^{-st^2}) = \sqrt{\frac{\pi}{s}}\, e^{-\omega^2/4s} \tag{5.34}$$

$$\int_{-\infty}^{+\infty} e^{-(\alpha t^2 + 2\beta t)}\, dt = \sqrt{\frac{\pi}{\alpha}}\, e^{\beta^2/\alpha} \tag{5.35}$$

$$\int_{-\infty}^{+\infty} e^{\pm j2\pi x a(x-b)}\, dx = \delta(a(x-b)) \tag{5.36}$$

AMBIGUITY FUNCTIONS FOR A SINGLE PULSE

RECTANGULAR PULSE

For a rectangular pulse,

$$u(t) = \frac{1}{\sqrt{\delta}} \text{rect}\left(\frac{t}{\delta}\right)$$

The ambiguity function for a rectangular pulse is given in the following form:

$$\chi_u(\tau,\phi) = \int_{-\infty}^{+\infty} u(t)\, u^*(t+\tau)\, e^{-j2\pi\phi t}\, dt$$

$$= \int_{-\delta/2}^{+\delta/2} u(t)\, u^*(t+\tau)\, e^{-j2\pi\phi t}\, dt$$

$$\chi_u(\tau,\phi) = \begin{cases} \text{rect}\left(\frac{\tau}{2\delta}\right) e^{j\pi\phi\tau} \left(\frac{(\delta-|\tau|)\sin(\pi\phi(\delta-|\tau|))}{\pi\phi\delta(\delta-|\tau|)}\right) & |\tau| \le \delta \\ 0 \quad \text{elsewhere} & \end{cases} \tag{5.37}$$

SINGLE FM RECTANGULAR PULSE

For an FM rectangular pulse,

$$u(t) = \frac{1}{\sqrt{\delta}} \text{rect}\left(\frac{t}{\delta}\right) e^{j\pi\alpha t^2}$$

The ambiguity function is

$$\chi_u(\tau,\phi) = \text{rect}\left(\frac{\tau}{2\delta}\right) e^{j\pi\phi\tau} \left(\frac{(\delta - |\tau|)\sin(\pi(\alpha\tau+\phi)(\delta - |\tau|))}{\pi\delta(\delta - |\tau|)\,(\alpha\tau+\phi)}\right) \qquad (5.38)$$

AMBIGUITY FUNCTION FOR SINGLE FM GAUSSIAN PULSE

For a Gaussian pulse

$$u(t) = (2a)^{1/4}\, e^{-\pi a t^2 + j\pi\alpha t^2} \qquad (5.39)$$

The ambiguity function is

$$\chi_u(\tau,\phi) = e^{j\pi\tau\phi}\, e^{-\pi/2\left(a\tau^2 + \frac{(\alpha\tau+\phi)^2}{a}\right)} \qquad (5.40)$$

AMBIGUITY FUNCTION FOR A PULSE TRAIN

Assume

$$y(t) = \sum_{n=0}^{N-1} u(t - nT_0) \qquad (5.41)$$

The ambiguity function for a pulse train is defined as

$$\chi_y(\tau,\phi) = \int_{-\infty}^{+\infty} \sum_{n=0}^{N-1} u(t - nT_0) \sum_{k=0}^{N-1} u^*(t - kT_0 + \tau)\, e^{-j2\pi\phi t}\, dt \qquad (5.42)$$

Assume $T_0 > 2\delta$, if $|\tau - mT_0| < \delta$

$$\chi_y(\tau,\phi) = \int_{-\infty}^{+\infty} \sum_{n=0}^{N-1} u(t - nT_0)\, u^*(t - (n + m)T_0 + \tau)\, e^{-j2\pi\phi t}\, dt$$

$$= \sum_{n=0}^{N-1} \int_{-\infty}^{+\infty} u(t - nT_0)\, u^*(t - (n + m)\, T_0 + \tau)\, e^{-j2\pi\phi t}\, dt$$

$$= \chi_u(\tau - mT_0, \phi) \quad \sum_{n=0}^{N-1} e^{-j2n\pi\phi T_0}$$

$$= \chi_u(\tau - mT_0, \phi)\; e^{j(N-1-m)T_0\phi}\, \frac{\sin((N-m)T_0\pi\phi)}{\sin(\pi T_0\phi)} \tag{5.43}$$

If $\left| \tau + mT_0 \right| < \delta$

$$\chi_y(\tau,\phi) = \int_{-\infty}^{+\infty} \sum_{n=0}^{N-1} u(t - nT_0)\, u^*(t - (n - m)T_0 + \tau)\, e^{-j2\pi\phi t}\, dt$$

$$= \sum_{-\infty}^{+\infty} \int_{n=0}^{N-1} u(t - nT_0)\, u^*(t - (n - m)\, T_0 + \tau)\, e^{-j2\pi\phi t}\, dt$$

$$= \chi_u(\tau + mT_0, \phi) \sum_{n=0}^{N-1} e^{-j2n\pi\phi T_o}$$

$$= \chi_u(\tau + mT_0, \phi)\; e^{j(N-1+m)T_0\phi}\, \frac{\sin((N-m)T_0\pi\phi)}{\sin(\pi T_0\phi)} \qquad (5.44)$$

So, the ambiguity function for a pulse train is

$$\chi_y(\tau,\phi) = \begin{cases} \displaystyle\sum_{m=-(N-1)}^{N-1} e^{-j\pi(N-1-m)\phi T_0} \chi_u(\tau - mT_0, \phi)\, \frac{\sin((N-m)T_0\pi\phi)}{\sin(\pi T_0\phi)} \\ 0 \quad |\tau - mT_0| \geq \delta \end{cases} \qquad (5.45)$$

<u>AMBIGUITY FUNCTION FOR DUAL WAVEFORM MODULATED PULSE TRAIN</u>

Assume that y(t) is the sum of two different waveforms u(t) and v(t) where v(t) lags u(t) by T. The ambiguity function of y(t) can be written as:

$$\chi_y(\tau,\phi) = \int_{-\infty}^{+\infty} (u(t) + v(t-T))\, (u^*(t+\tau) + v^*(t - T + \tau))\, e^{-j2\pi\phi t}\, dt$$

$$= \chi_u(\tau,\phi) + \chi_{uv}(\tau-T,\phi) + \chi_{vu}(\tau + T,\phi)\, e^{-j2\pi\phi T} + \chi_{vv}(\tau,\phi)\, e^{-j2\pi\phi T} \qquad (5.46)$$

Similarly, we can derive the ambiguity function of a pulse pair train. Assume that the pulse train can be represented as:

$$y(t) = \sum_{n=0}^{N-1} u(t - nT_1) + v(t - nT_1 - T_2) \qquad (5.47)$$

where $T_2 < T_1$ and twice the pulse duration $2\delta < T_2$. Thus, the ambiguity function is defined as

$$\chi_u(\tau,\phi) = \int_{-\infty}^{+\infty} y(t)y^*(t + \tau)\, dt$$

$$= \sum_{n=0}^{N-1} \sum_{k=0}^{N-1} \int_{-\infty}^{+\infty} u(t-nT_1)u^*(t-kT_1+\tau)\, e^{-j2\pi\phi t}\, dt$$

$$+ \sum_{n=0}^{N-1} \sum_{k=0}^{N-1} \int_{-\infty}^{+\infty} u(t-nT_1)v^*(t-kT_1-T_2+ \tau)\, e^{-j2\pi\phi t}\, dt$$

$$+ \sum_{n=0}^{N-1} \sum_{k=0}^{N-1} \int_{-\infty}^{+\infty} v(t-nT_1-T_2)u^*(t-kT_1+ \tau)\, e^{-j2\pi\phi t}\, dt$$

$$+\sum_{n=0}^{N-1}\sum_{k=0}^{N-1}\int_{-\infty}^{+\infty} v(t-nT_1)v^*(t-kT_1-T_2+\tau)\, e^{-j2\pi\phi t}\, dt$$

$$= \chi_{\Sigma u}(\tau,\phi) + \chi_{\Sigma v}(\tau,\phi)\, e^{-j2\pi\phi T_2} + \chi_{\Sigma uv}(\tau - T_2,\phi)$$

$$+ \chi_{\Sigma vu}(\tau + T_2,\phi)\, e^{-j2\pi\phi T_2} \qquad (5.48)$$

In special cases, the pulses in a pair are linear FM modulated with an opposite frequency modulation as shown below.

$$u(t) = (2a)^{1/4}\, e^{-\pi a t^2 + j\pi\alpha t^2}$$

$$v(t) = (2a)^{1/4}\, e^{-\pi a t^2 - j\pi\alpha t^2} \qquad (5.49)$$

Since $v(t) = u^*(t)$ and from the properties of the ambiguity function, we know that [83]

$$\chi_u(\tau,\phi) = \chi_v^*(\tau, -\phi) \qquad (5.50)$$

so from (5.40), we can derive $\chi_v(\tau,\phi)$,

$$\chi_v(\tau,\phi) = e^{j\pi\tau\phi}\, e^{-\pi/2\left(a\tau^2 + \frac{(\alpha\tau-\phi)^2}{a}\right)} \qquad (5.51)$$

The cross ambiguity $\chi_{uv}(\tau,\phi)$ can be derived from the following integral:

$$\chi_{uv}(\tau,\phi) = \int_{-\infty}^{+\infty} u(t)\, v^*(t + \tau)e^{-j2\pi\phi\tau}\, dt$$

$$= \int_{-\infty}^{+\infty} (2a)^{\frac{1}{2}} e^{-\pi(a - j\alpha)t^2}\, e^{-\pi(a - j\alpha)(t + \tau)^2} e^{-2\pi\phi t}\, dt$$

$$= (2a)^{\frac{1}{2}} \int_{-\infty}^{+\infty} e\left\{-2\pi(a-j\alpha)(t^2+t\tau+\frac{\tau^2}{2})\right\} e^{-j2\pi\phi t}\, dt$$

$$= (2a)^{\frac{1}{2}}\, e^{-\pi(a - \alpha)\tau^2} \int_{-\infty}^{+\infty} e^{-2\pi(a - j\alpha)(t^2+(\tau + \frac{j\phi}{a-j\alpha})t)}\, dt$$

If we let $\alpha = 2\pi(a\text{-}j\alpha)$ and $\beta = \pi(a\text{-}j\alpha)(\tau + \frac{j\phi}{a-j\alpha})$, by equation (5.35), the above integral is equal to

$$\chi_{uv}(\tau,\phi) = \sqrt{\frac{a}{a-j\alpha}}\, \exp\left((\frac{\pi}{2}(a-j\alpha)(-\tau^2 - \frac{2\phi\tau(\alpha-ja)}{a^2 + \alpha^2} + \frac{-\phi^2}{(a-j\alpha)^2}) \right)$$

$$= \sqrt{\frac{a}{a-j\alpha}}\, \exp\left[\frac{\pi}{2}(a-j\alpha)\left\{ -\tau^2 - \frac{2\tau\alpha\phi^2}{a^2 + \alpha^2} - \frac{(a^2 - \alpha^2)\phi^2}{(a^2 + \alpha^2)^2} \right.\right.$$

$$+\frac{j2\phi a\tau}{a^2+\alpha^2} - \frac{j2a\alpha\phi^2}{(a^2+\alpha^2)^2}\Big\}\Big]$$

$$= \sqrt{\frac{a}{a - j\alpha}}\, e^{-\frac{\pi}{2}\left(a\tau^2 + \frac{a\phi^2}{a^2 + \alpha^2}\right)}\, e^{-j\frac{\pi}{2}\left(-\alpha t^2 - 2\phi\tau + \frac{\alpha\phi^2}{a^2 + \alpha^2}\right)} \tag{5.52}$$

As $u(t) = v^*(t)$, it can be shown that $\chi_{uv}(\tau,\phi) = \chi^*_{vu}(\tau,\phi)$. It follows that

$$\chi_{vu}(\tau,\phi) = \sqrt{\frac{a}{a + j\alpha}}\, e^{-\frac{\pi}{2}\left(a\tau^2 + \frac{a\phi^2}{a^2 + \alpha^2}\right)}$$

$$e^{j\frac{\pi}{2}\left(-\alpha t^2 + 2\phi\tau + \frac{\alpha\phi^2}{a^2 + \alpha^2}\right)} \tag{5.53}$$

EFFECTIVE SIGNAL-TO-INTERFERENCE RATIO

The total interference at the output of a matched filter can be approximately calculated as:

$$C = \int_{-\delta}^{+\delta}\int_{-\infty}^{+\infty} \chi_{uv}(\tau,\phi)\, d\tau d\phi$$

$$= \sqrt{\frac{a}{a-j\alpha}} \int_{-\delta}^{+\delta}\int_{-\infty}^{+\infty} e^{-\frac{\pi}{2}\left[(a-j\alpha)\tau^2 - j2\phi\tau + \frac{a+j\alpha}{\alpha^2+a^2}\phi^2\right]} d\tau d\phi$$

$$= \sqrt{\frac{a}{a-j\alpha}} \int_{-\delta}^{+\delta} e^{-\frac{\pi}{2}(a-j\alpha)\tau^2} \int_{-\infty}^{+\infty} e^{-\frac{\pi}{2}\left[-j2\phi\tau + \frac{a+j\alpha}{\alpha^2+a^2}\phi^2\right]} d\phi d\tau$$

$$= \sqrt{\frac{a}{a-j\alpha}} \int_{-\delta}^{+\delta} e^{-\frac{\pi}{2}(a-j\alpha)\tau^2} \sqrt{\frac{2(a^2+\alpha^2)}{a+j\alpha}}\, e^{-\frac{\pi}{2}\frac{a^2+\alpha^2}{a+j\alpha}\tau^2}\, d\tau$$

$$= \sqrt{2a} \int_{-\delta}^{+\delta} e^{-\pi(a-j\alpha)\tau^2}\, d\tau$$

$$\simeq \sqrt{\frac{2a}{a-j\alpha}} \qquad (5.54)$$

Chapter 6

Conclusions and Recommendations for Future Work

The major focus of this research was a system study of a Doppler radar used for global wind measurements. In addition to studying cloud modeling and the system configuration, such as antenna scan pattern, we discussed algorithms for estimating the first moment of power spectra of radar signals, and algorithms for reducing frequency and range ambiguities of Doppler radar systems. The results can be summarized as follows:

(1) In Chapter 2 we reviewed volume backscattering of radar echoes from clouds. For three different types of cloud, we simulated the SNRs of the radar echoes. The results demonstrated that, from the SNR point of view, frequencies of 35 GHz or higher are needed to obtain high enough SNRs of radar echoes from these types of clouds, presuming the radar system has enough power and enough gain of the antenna. Although the results were based only on water-cloud models, ice clouds tend to have larger reflectivity than water clouds. The SNRs from ice clouds will be larger than those from the water clouds with the same system parameters. However, in the computer simulations, the cloud models were based on an analytical drop-size distribution formula, and these drop-size distributions may be quite different from the drop-size distributions found in practice. Therefore, more realistic cloud models may need to be developed in future study.

(2) In Chapter 3, we discussed the system configuration of the radar wind sounder. Three different antenna scan methods were discussed,and the result revealed that a combination of uniform and discrete antenna scanning would result in acceptable pointing errors and cost. We also discussed a tracking method to estimate the Doppler frequency shift caused by satellite motion. The tracking is through a combination of satellite inertial navigation system and a second-order phase-lock-loop. The result of a computer simulation with a step input function

showed that for given antenna pointing errors, and parameters of the phase-lock-loop, this method can achieve very small RMS errors (several Hertz) in a steady state. However, the simulation was crude since the clutter echoes used as the input signal of the tracking system may be much different from the input signal used in the simulation. More thorough analysis of the tracking system and more accurate models of the tracking system and input signal need to be developed in future study of RAWS. In addition, different tracking methods, such as a Kalman filter, may also need to be considered in the future study.

(3) We also conducted an error analysis in Chapter 3, and the result showed that error caused by satellite pointing angle is an important factor to the system performance. To achieve the required accuracy (1m s^{-1}), a large number of independent measurements needs to be averaged. The error analysis was based upon the error in measurement of the mean Doppler frequency and estimate of the Doppler shift caused by satellite motion. However, these estimate errors and measurement errors are usually functions of the SNR of the received signal. An error analysis concerning SNRs of the system may need to be performed in the future study.

We also pointed out in Chapter 3 that clutter rejection is an important issue in the design of RAWS. However, in this dissertation we did not discuss this problem. This topic should be left as a topic of future study.

(4) In Chapter 4, we discussed several algorithms for estimating the mean Doppler frequency: the FFT estimator, the covariance estimator, and the estimators based on autoregressive models. The covariance estimator produced slightly smaller RMS errors than the FFT estimator and the autoregressive-model-based estimators in the computer simulations. However, these results were derived under the condition that the power spectrum of the radar echo is symmetric and has only one peak. In practice, interference caused by leakage from the transmitter, or clutter, may cause the returned signals to have non-symmetric spectrum or spectrum with more than one peak.

The performance of the FFT estimator and the AR-based estimators are affected by the noise and alias of the frequency of the radar echoes. A noise-suppression method was discussed in this chapter. It can effectively remove the bias caused by white noise. We also discussed a method for removing the bias caused by frequency alias; this method can also reduce the bias caused by noise.

The FFT, the covariance estimator, and the AR estimator are comparable in terms of estimate errors. Although, the RMS errors in the estimates depend on both the spectral widths and SNRs of the input signals. The RMS error is mainly a function of the spectral width of the signal when the SNR is above 5 dB. As discussed, the spectral widths of the signals in RAWS are about half of the Nyquist interval. In such case, the RMS errors produced by these estimators discussed in Chapter 4 were as large as 10% of the Nyquist frequency. That is, for a 3500-Hz PRF, the RMS errors are around 175 Hz. This error is higher than the error limit (23 Hz) for the mean frequency estimates needed to produce the 1m s^{-1} accuracy in wind estimates. About 64 independent measurements may need to be averaged to achieve the required accuracy.

(6) In Chapter 5, we reviewed several algorithms for reducing the radar ambiguities, such as a phase-coding method and staggered prf methods. However, these methods do not perform well when the spectral widths of the radar echoes are large (> 50% of the Nyquist interval). Therefore, a new method based on using different waveform modulations on successive transmitted pulses was developed to reduce the radar ambiguities. Monte-Carlo simulations were used to compare the performance of this method with two staggered-prf methods. The results showed that when the spectral width of the signal increases, the RMS errors increase rapidly with the staggered-prf methods. However, the RMS error for the waveform modulation method does not change very much as the the spectral width of the radar signal increases.

In the RAWS system, the spectral widths of the radar echoes are about half of the Nyquist interval. In such a case, the staggered PRF-A method has very large probability of false measurements; about 20% at 10 dB SNR and 30% at 5 dB SNR.

The RMS errors produced by the waveform modulation are about 7% of the Nyquist interval at 10 dB SNR, and about 12% at 5 dB SNR. The staggered PRF-B method generates very large RMS errors, over 50% of the Nyquist interval, when the spectral width is equal to or greater than half of the Nyquist interval. In all these computer simulations, the extended maximum unambiguous frequency is 7 times as large as the Nyquist interval. For a 3500-Hz prf, the maximum unambiguous frequency is 12250 Hz. In summary, the waveform modulation method is the most promising algorithm among the algorithms discussed in this chapter to be used in the RAWS for estimating the Doppler mean frequency.

REFERENCES

[1] G. E. Stout and E. A. Mueller, "Survey of relationships between rainfall rate and radar reflectivity in the measurement of precipitation," *J. Appl. Meteorol.*, vol. 7, pp. 465-474, 1968.

[2] D. Atlas, C. W. Ulbrich, and R. Mneghini, "The multi-parameter remote mesurement of rainfall," *Radio Science*, vol. 19, pp. 3-22, 1984.

[3] K. R. Hardy, and I. Katz, "Probing the clear atmosphere with high power, high resolution radars," *Proceedings of the IEEE*, vol. 57, pp. 468-480, 1969.

[4] K. S. Gage, J. L. Green, and T. E. VanZandt, "Use of Doppler radar for the measurement of atmospheric turbulence parameters from the intensity of clear-air echoes," *Radio Science*, vol. 15, no. 2, pp. 407-416, 1980.

[5] R. J. Doviak, R. M. Rabin, and A. J. Koscielny, "Doppler weather radar for profiling and mapping winds in the prestorm environment," *IEEE Trans. Geosci. Remote Sensing*, vol. 21, pp. 25-33, 1983.

[6] W. H. Heiss and D. L. McGrew, "Nexrad: Next Generation Weather Radar (WSR-88D)," *Microwave Journal*, pp. 79-98, January 1990.

[7] Tropical Rain Measurement Mission Science Steering Group Workshop, Calverton, MD., Nov. 13-14, 1986. (Sponsored by Atmospheric Dynamics and Radiation Branch, NASA Headquarters, Washington, DC.)

[8] R. M. Lhermitte, "Coud and Precipitation Remote Sensing at 94 GH," *IEEE Trans. Geosci. Remote Sensing*, vol. 26, no. 3, pp. 207-216, May 1988.

[9] R. J. Curran, ed., *Earth Observing System Instrument Panel Report: LAWS Laser Atmospheric Wind Sounder*, vol. IIg, NASA, Washington DC, 1987.

[10] G. J. Haltiner, and R. T. Williams, *Numerical Prediction and Dynamic Meteorology* , John Wiley & Sons, New York, 1980.

[11] D. Atlas and C. L. Korb, "Weather and Climate Needs for Lidar Observations from Space and Concepts for Their realization," *Bull. Amer. Meteor. Soc.*, vol. 62, p.1270, 1981.

[12] N. A. Phillips, "An Accuracy Goal for a Comprehensive Satellite Wind Measuring System" *Monthly Weather Review*, pp. 237-239, Jan. 1983.

[13] J. G. Navarra, *Atmosphere, Weather and Climate: An Introduction to Meteorology*, W. B. Saunders Company, Philadelphia, 1979.

[14] E. Kalnay, J. C. Jusem, and J. Pfaendtner, "The relative importance of mass and wind data in the present observing system," *Proceedings of the NASA Symposium on Global Wind Measurements*, A. Deepak Publishing, Hampton, VA, 1985.

[15] W. E. Baker, and R. J. Curran, eds., *Report of the NASA Workshop on Global Wind Measurements*, STC2081, A. Deepak Publishing, Hampton, VA, 1985.

[16] R. Atlas, E. Kalnay, W. E. Baker, J. Susskind, D. Reuter and M. Halem, "Simulation studies of the impact of future observing systems on weather prediction," *Proceedings of the Seventh Conference on Numerical Weather Prediction*, Montreal, pp.145-151, June 1985.

[17] R. M. Huffaker, ed., "Feasibility study of satellite borne lidar global wind monitoring system," *NOAA Tech. Memo. ERK WPL-37*, Wave Propagation Laboratory, Boulder, Colo., 297 pp., 1978.

[18] V. J. Abreu, "Wind measurements from and orbital platform using a lidar system with incoherent detection: an analysis," *Applied Optics*, vol. 18, No. 17, pp. 2992-2997, Sept. 1979.

[19] R. M. Huffaker, T. R. Lawrence, Madison J. Post, J. T. Priestley, F. F. Hall, Jr., R. A. Richter and R. J. Keeler "Feasibility studies for a global wind measuring satellite system(Windsat): analysis of simulated performance," *Applied optics*, vol. 23, No. 15, pp. 2523-2536, August 1984.

[20] C. Dey, C. P. Arnold, and W. Bostelman, "Design of a Windsat observing system simulation experiment," *Proceedings of the NASA Symposium on Global Wind Measurements*, A. Deepak Publishing, Hampton, Virginia, 1985.

[21] J. Bilbro, G. Fichtl, D. Fitzjarrald, M. Krause, and R. Lee, "Airborne Doppler Lidar Wind Field Measurements," *Bull. Amer. Meteo. Soc.*, vol. 65, No. 4, pp.348-359, April 1984.

[22] J. C. Sadler, and B. J. Kilonsky, "Deriving Surface Winds from Satellite Observations of Low-Level Cloud Montions," *J. of Climate and Appl. Meteorol.*, vol. 24, pp. 758-769, 1985.

[23] G. D. Emmitt, "Doppler Lidar Sampling Strategies and Accuracies -- Regional Scale," *Symposium and Workshop on global Wind Measurements*, Columbia, MD, July 29-August 1, 1985.

[24] R. K., Moore, et al., *Radar Wind Sensor (RAWS)*, Instrument Investigation, vol. 1, Investigation and Technical Plan, Data Plan, Management Plan, July, 1988, Proposal from KU CRINC to NASA.

[25] F. T. Ulaby, R. K. Moore, A. K. Fung, *Microwave Remote Sensing*, vol, I, Chapter 5, Addison-Wesley Publishing Company, Reading, Massachusetts, 1981.

[26] G. Mie, "Beitrage zur Optik truber medien," speziell Koloidaler metalasungen, *Ann. Physik*, vol. 25, 377 p., 1908.

[27] J. A. Stratton, *Electromagnetic Theory*, McGraw-Hill Book Co., New York , 1941.

[28] L. J. Battan, *Radar Observation of the Atmosphere*, University of Chicago Press, Chicago, 1973.

[29] Fraser, K. S., N. E. Gaut, E. C. Reifenstein, II, and H. Sievering, "Interaction Mechanisms - Within the Atmosphere," in *Manual of Remote Sensing*, I, R. G. Reeves, ed., American Society of Photogrammetry, Falls Church, Virginia, Chapter 5, pp. 207-210, 1975.

[30] G. Maral and M. Bousquet, *Satellite Communications Systems*, John Wiley & Sons, New York, 1986

[31] J. R. Probert-Jones,"The radar equation in meteorology," *Quart. J. R. Met. Soc.*, vol. 88, pp. 485-495, 1962.

[32] R. R. Rogers, *A short course in cloud physics*, Pergamon Press, Oxford and New York, 1979.

[33] Mason, B. J., *The physics of Clouds*, Oxford Univ. Press(Clarendon), Oxford, 1957.

[34] H. R. Pruppacher, *Microphysics of Clouds and Precipitation*, D. Reidel Publishing Company, Dordrecht, Holland, 1980.

[35] P. V. Hobbs, ed., *Clouds, their formation, optical properties, and effects*, pp. 93-183. Academic Press, New York, 1981.

[36] A. J. Heymsfield, and Knollenberg R. G., "Properties of cirrus generating cells," *J. Atmospheric Sci.*, 29, pp. 1358-1366, 1972.

[37] L. J. Battan, and R. R. Braham, "A Study of Convective Precipitation Based On Cloud and Radar Observations," *J. Meteor.* , vol. 13, pp. 587, 1956.

[38] T. R. Morris, "Shorter Contribution - Precipitation in Arizona Cumulus As A Function Of Cloud Size And Temperature," *J. Meteor.* , vol. 14, pp. 281, 1957.

[39] E. B. Dobson "Doppler radar measurements of mean wind variations in the clear atmosphere," *Preprints, 14th Conference on Radar Meteorology (Tucson)*, Am. Meteoro. Soc., Boston, pp. 69-78, 1970.

[40] K. A. Browning, J. R. Starr, and A. J. Whyman, "Measurements of air motion in regions of clear air turbulence using high-power Doppler radar," *Nature*, 239, pp. 267-269, 1972.

[41] R. F. Woodman, and A. Guillen, "Radar observations of winds and turbulence in the stratosphere and mesosphere," *J. Atmos. Sci..*, 31, pp. 493-505, 1974.

[42] P. Czechowsky, J. Klostermeyer, J. Rottger, R. Ruster, G schmidt, and R. F. Woodman, "The SOUSY VHF radar for tropospheric stratospheric and mesospheric sounding," *Preprints, 17th Conference on Radar Meteorology (Seattle)*, Am. Meteoro. Soc., Boston, pp. 349-353, 1976.

[43] C. A. Balanis, *Antenna Theory- Analysis and Design*, pp.604 -636, Harper & Row, Publishers, New York, 1982.

[44] R. J. Doviak and D. S. Zrnic, *Doppler Radar and Weather Observations*, Academic Press, New York, 1984.

[45] Toshiaki Kozu, "Consideration of Vertical Resolution for Near Nadir-looking Space Borne Radar," *IEEE Trans. Geosci. and Remote Sensing*, vol. 27, No. 4, July 1989.

[46] M. L. Skolnik, *Introduction To Radar Systems*, 2nd ed., Chapter 13, McGraw-Hill, New York, 1980.

[47] F. T. Ulaby, R. K. Moore, A. K. Fung, *Microwave Remote Sensing*, Chapter 11, Addison-Wesley Publishing Company, vol. II, Reading, Massachusetts, 1981.

[48] F. M. Gardner *Phaselock Techniques*, 2 ed. John Wiley&Sons, New York, 1979.

[49] J. K. Holmes, *Coherent Spread Spectrum Systems*, John Wiley & Sons, New York, 1982.

[50] W. C. Lindsey and C. M. Chie, *Phase-Locked Loops*, IEEE Press, New York, 1986.

[51] V. Manassewitsch, *Frequency Synthesizers - Theory and Design*, 3ed. John Wiley & Sons, New York, 1987.

[52] J. M. Richardson, *Simulation of Non-Linear System*, PhD Dissertation, Oklahoma State University, 1980.

[53] P. E. Kopp, *Martingales and Stochastic Integrals*, Cambridge Press, Cambridge and New York, 1984.

[54] V. Krishnan, *Nonlinear Filtering and Smoothing - An Introduction to Martingales, Stochastic integrals and Estimation*, John Wiley & Sons, New York, 1984.

[55] W. Rudin, *Real and Complex Analysis*, McGraw-Hill, New York, 1981.

[56] S. M. Pizer, and V. L. Wallace, *To Compute Numerically -- Concepts and Strategies*, Little, Brown&Company Limited, Boston, 1983.

[57] S. M. Key and S. L. Marple, Jr., "Spectrum Analysis-A Modern Perspective," *Proceedings of the IEEE*, November 1981.

[58] A. V. Oppenheim and R. W. Schafer, *Digital Signal Processing*, Prentice-Hall, Englewood Cliffs, N.J., 1975.

[59] R. J. Doviak and D. Sirmans, "Considerations for Pulse-Doppler Radar Observations of Severe Thunderstorms," *J. of Applied Meteorol.*, vol 17, pp. 189 - 205, February 1978.

[60] H. P. William, P. F. Brian, A. T. Saul, and T. V. William, *Numerical Recipes in C - The art of Scientific Computing*, Cambridge University Press, Cambridge and New York, 1988.

[61] R. V. Hogg, and A. T. Craig, *Introduction To Mathematical Statistics*, Macmillan Publishing Co., New York, Collier Macmillan Publishers, London, 1978.

[62] B. Liu, and D. C. Munson, Jr., "Generation of a Random Sequence Having a Jointly Specified Marginal Distribution and Autocovariance," *IEEE Trans. on Acoustics, Speech, and Signal Processing*, vol. ASSP-30, No6, pp. 973-983, December, 1982.

[63] D. S. Zrnic, "Simulation of weatherlike Doppler spectra and signals," *J. of Applied Meteorol.*, vol. 14, pp. 619-620, 1975.

[64] D. Sirmans and B. Bumgarner, " Numerical comparison of five mean frequency estimators," *J. of Applied Meteorol.*, vol. 14, pp. 991-1003, Sept. 1975.

[65] D. S. Zrnic, "Estimation of spectral moments for weather echoes," *IEEE Trans. Geosci. Electron.*, vol. GE-17, pp. 113-128, Oct. 1979.

[66] W. D. Rummler, "Introduction of a new estimator for velocity spectral parameters," *Tech. Memo. MM-68-4121-5*, Bell Telephone Labs., Whippany, NJ, 1968.

[67] W. D. Rummler, "Two pulse spectral measurements," *Tech. Memo. MM-68-4121-15*, Bell Telephone Labs., Whipany, NJ, 1968.

[68] F. C. Benham, H. L. Groginsky, A. S. Soltes and G. Works, "Pulse-pair estimation of Doppler spectrum parameters," *Final Report, Contract F-19628-71-C-0126*, Raytheon Co., Wayland, MA, 1972.

[69] K. S. Miller, and M. M. Rochwarger, "A covariance approach to spectral moment estimation," *IEEE Trans. Inform. Theory*, IT-18, 588-596, 1972.

[70] D. Sirmans, and B. Bumgarner, "Estimation of spectral density mean and variance by covariance argument techniques," *Preprints 16 th Radar Meteorology Conf.*, Houston, Am. Metoro. Soc., pp. 6-13, 1975.

[71] D. S. Zrnic, "Spectral moment estimates from correlated pulse pairs," *IEEE Trans. on Aerospace and Electronic Systems*, vol. 13, no. 4, pp.344-354, 1977.

[72] Stanislav B. Kesler, ed., *Modern Spectrum Analysis, II,* IEEE press, New York, 1986.

[73] M. J. Gwilym, and G. W. Donald, *Spectral Analysis and its Applications*, Holden-Day, SanFrancisco, 1968.

[74] M. B. Priestley, *Spectral Analysis and Time Series*, vol. I, Academic Press, London and New York, 1981.

[75] H. S. Shapiro, and R. A. Siverman, "Alias-free sampling of random noise," *J. Soc. Ind. Appl. Math.*, 8, pp. 225-248, 1960.

[76] R. H. Jones, "Aliasing with Unequally Space Observations," *J. of Applied Meteorol.*, vol. 11, No. 2, pp. 245-254, March, 1972.

[77] W. B. Sweezy, "Comparison of maximum entropy method estimation of Doppler velocity moments with conventional techniques," *18th Conf. on Radar Meteorology*, Am. Meteoro. Soc., pp. 28-31, Atlanta, GA, 1978.

[78] Peter S. Ray and Conrad Ziegler, "De-Aliasing First-Moment Doppler Estimates," *J. of Applied Meteorol.*, vol. 16, pp. 563-564, May, 1977.

[79] E. A. Mueller, and E. J. Silha, "Unique features of the CHILL radar system," *Preprints 18th Conf. on Radar Meteorology*, Am. Meteoro. Soc., pp.381-382, Atlanta, GA, 1978.

[80] R. G. Strauch, R. A. Kropfli, W. B. Sweezy, W. R. Moninger and R. W. Lee, "Improved Doppler velocity estimates by the poly-pulse pair method," *Preprints 18 th Conf. on Radar Meteorology*, Am. Meteoro. Soc., pp.376-380, Atlanta, GA, 1978.

[81] R. J. Doviak, and D. Sirmans "Doppler radar with polarization diversity," *J. Atmos.* Sci., vol. 30, pp. 737-738, 1973.

[82] Jiro Aoyagi, "Wind Measurements by a Doppler Radar," Preprints, *21st American Meteorology Society Conference on Radar Meteorology*, (Edmonton, Alberta), pp. 536-541, 1983.

[83] G. W. Deley "Waveform Design," in *Radar Handbook* (M. I. Skolnik, ed.), pp. 3-1 - 3-47. McGraw-Hill, New York, 1970.

[84] B. Nutten et al., "The RONSARD radars: A versatile C-band Doppler facility," *IEEE Trans. Geosci. Electron.*, vol. GE-17, no. 4, pp. 281-288, 1979.